Universität Stuttgart

Three Dimensional Analytical Study of Thin Film Battery Electrodes

Von der Fakultät Chemie der Universität Stuttgart zur Erlangung der Würde
eines Doktors der Naturwissenschaften (Dr. rer. nat.) genehmigte
Abhandlung

Vorgelegt von
Ahmed Mohamed Abdelkarim
aus Ägypten

Hauptberichter:	Prof. Dr. Dr. h. c. Guido Schmitz
Mitberichter:	Prof. Dr. -Ing. Kai Peter Birke
Mitprüfer:	Prof. Dr. Thomas Schleid
Tag der mündlichen Prüfung:	27. Oktober 2021

Institut für Materialwissenschaft der Universität Stuttgart
Lehrstuhl für Materialphysik

2021

Gedruckt und veröffentlicht mit der Unterstützung des Deutschen Akademischen Austauschdienstes (DAAD).

Printed and published with the support of the German Academic Exchange Service (DAAD).

@2021 All rights reserved

Liability Agreement

I hereby certify that the dissertation entitled: "Three Dimensional Analytical Study of Thin Film Battery Electrodes" is entirely my own work except where otherwise indicated. Passages and ideas from other sources have been clearly indicated.

Ich versichere, dass ich die vorliegende Arbeit mit dem Titel: "Three Dimensional Analytical Study of Thin Film Battery Electrodes" selbständig verfasst und keine anderen als die angegebenen Quellen und Hilfsmittel benutzt habe; aus fremden Quellen entnommene Passagen und Gedanken sind als solche kenntlich gemacht.

....

Ort, Datum Abdelkarim, Ahmed

Acknowledgments

First and foremost, with a deep sense of gratitude, I want to thank the God for allowing me to perform this thesis and peace be upon Prophet Muhammad. This thesis is the result of the work whereby I have been accompanied and supported by many people. It is a pleasant opportunity to express my gratitude for all of them.

I'm highly indebted to the German Academic Exchange Service (DAAD) and the Egyptian Missions authority for their personal fund. I sincerely express my deepest gratitude to the DAAD employees in Bonn, Germany and Cairo, Egypt for their help and support.

I would gratefully like to express my deep appreciation to Prof. Dr. Dr. h. c. Guido Schmitz for giving me the opportunity to do my PhD at the Chair of Materials Physics at the University of Stuttgart, who inspired me to deepen my knowledge in materials physics. Moreover, I would like to thank him for providing help and support whenever needed. His great guidance had a huge impact in my studies.

I'm pleased to express my profound gratitude and deep thanks to Dr. Patrick Stender for his professional and technical guidance, helpful suggestion, support and valuable advices. I sincerely express my deepest gratitude to Dr. Efi Hadjixenophontos for her outstanding willingness to help, Dr. Yug Joshi for his thoughtful discussions and overall enormous support, Dr. Robert Lawitzki for his kind support and Rüya Duran for her kind help and her invested time. Also, I would like to thank Jianshu Zheng for his fruitful discussions. I am highly grateful to my colleagues: Helena Solodenko, Samuel Griffiths, and Evgeniia Volobueva for their corrections and assistance.

Dimitrios Paroglon, Peter Engelhardt, Jacqueline M. Dunn, and Frank Hack for the best working atmosphere. My heartfelt thanks to all my friends and colleagues in University of Stuttgart and Max Planck Institute for intelligence systems for them untiring and continued support during my thesis work.

Lastly, this thesis could not have been completed without the endless love and blessings from my family. I wish to thank my parents, who taught me the value of hard work and rendered me enormous support during the whole tenure of my research work. I would like to thank them, for their patience to go through this endeavor hand-in-hand with me. Without their dearly accompaniment, both physically and spiritually, there would be no such an achievement.

Abdelkarim, Ahmed

Contents

Nomenclature **xi**

Abstract **xiii**

Kurzfassung **xvii**

1 Introduction **1**

2 Theoretical Concepts **7**

2.1 Crystal structure of LFP 7

2.2 Phase Transformations 8

2.3 Electro-chemical behavior of LFP 9

2.3.1 Miscibility gap 14

2.3.2 Interfacial zone 16

2.4 Configuration and principle of Li-ion batteries 17

2.5 X-Ray Diffraction (XRD) 18

2.6 Transmission Electron Microscope (TEM) 19

2.7 Field Ionization 21

2.8 Field Evaporation 22

2.9 Field Ion Microscopy (FIM) 24

2.9.1 FIM technique 25

2.10 Atom Probe Tomography (APT) 27

2.10.1 APT technique 29

2.11 Volume Reconstruction 32

2.12 Data Analysis 34

2.12.1 Concentration Analyses 34
2.12.2 Isoconcentration and Isodensity 34
2.13 Voxelisation 35

3 Experimental 37

3.1 Electropolishing 37
3.2 Reactive Ion Beam Sputtering 38
3.3 Electrochemistry 39
3.3.1 Open Circuit Voltage (OCV) 40
3.3.2 Cyclic Voltammetry (CV) 40
3.3.3 Chronoamperometry (CA) 41
3.4 Dual Beam Microscopy (SEM/FIB) 41
3.4.1 Lift-out procedure 43
3.4.2 2 μm tungsten post 45
3.4.3 TEM Lamella 45

4 Electrochemistry of LFP 49

4.1 Structural and morphological characterization 49
4.1.1 Structural characterization by XRD 49
4.1.2 Compositional characterization by ICP-OES 50
4.1.3 Morphological characterization by TEM 51
4.2 Electrochemical characterization 52
4.2.1 Rate capability 52
4.2.2 Cycle stability 54
4.2.3 Li kinetics 56

5 3D Analyses of Amorphous and Crystalline LFP 67
5.1 Evaporation field of Lithium Iron Phosphate (LFP) 67
5.1.1 LFP/W bi-layers 68
5.1.2 LFP/Fe multilayers 74
5.2 Amorphous LFP 77
5.3 Crystalline LFP 83
5.4 LFP at different laser powers 86
5.5 Local Li Enrichment 96

6 3D Analysis of Dis-/charged LFP 107
6.1 LFP at different de-/lithiation states 107
6.2 Frequency distribution analyses 114

7 Summary 125

Bibliography 127

A Appendix 141

List of Tables 153

List of Figures 169

Nomenclature

APT	Atom Probe Tomography
CA	Chronoamperometry
CV	Cyclic Voltammetry
EC:DMC	Ethylene Carbonate and Dimethyl Carbonate
FEG	Field Emission Gun
FIB	Focused Ion Beam
FIM	Field Ion Microscope
FP	Iron Phosphate
GIS	Gas Injection System
HOMO	Highest Occupied Molecular Orbital
ICF	Image Compression Factor
ICP-OES	Inductively Coupled Plasma - Optical Emission Spectrometry
LEAP	Local Electrode Atom Probe
LFP	Lithium Iron Phosphate
LIB	Lithium Ion Batteries
LMIS	Liquid Metal Ion Source
LUMO	Lowest Unoccupied Molecular Orbital
MCP	Microchannel Plates
OCV	Open Circuit Voltage

RF	Radio Frequency
SEI	Solid Electrolyte Interphase
SEM	Scanning Electron Microscope
SEM/FIB	Dual Beam Microscope
TEM	Transmission Electron Microscope
ToF	Time of Flight
XRD	X-ray Diffraction

Abstract

Li ions play a major role in batteries for energy storage. On the other hand, Li is notoriously challenging to be reliably detected with most microscpic techniques. Owing to its weak scattering form factor, low X-ray emission or peak overlaps in EELS spectroscopy, precise microscopic analysis of Li in battery materials is delicate. The aim of this study was to investigate a very sensitive analysis of the ionic transport on a microscopic, even on an atomic level scale. Well controlled amorphous lithium iron phosphate (LFP) thin films were prepared by ion-beam sputter deposition. In a subsequent annealing step, amorphous films were then crystallized. The electrochemical performance of both LFP phases is checked in cyclo-voltammetry, while structure and microstructure are confirmed by XRD and TEM, respectively. Cycling reversibility over 7000 cycles with a retention > 92 % is accomplished for the crystalline LFP, whereas the amorphous phase is electrochemically nonfunctional. Intercalation of LFP thin films was studied as a function of film thickness (25 - 250 nm). The intercalation kinetics is systematically quantified over a wide range of scanning rates (0.004 to 400 $\mathrm{mV\,s^{-1}}$) in cyclic voltammetry experiments. Two different diffusion regimes for the material undergoing two-phase reaction were explained with the help of the modified Randles-Sevcik equation. Slow Li diffusion in the thickest films was recorded. Dependence of the peak current on the layer thickness is explained in terms of increasing the grain boundary (GB) area. Opposite to the peak fluxes, the overpotential was interestingly found to be independent of the layer thickness. Less electrical driving force is required to force the same current in thick films. The grain boundaries represent an electroactive interface at which the overpotential appears. And hence, the grain boundaries work as fast conduction paths for faster Li ions diffusion. Thus, the total current is controlled by the total grain boundary area rather than the thin film surface.

$LiFePO_4$ (LFP) is then 3-dimensionally studied by laser-assisted Atom Probe Tomography (APT). The effects of laser power on the quantitative analysis of the amorphous phase by atom probe tomography were considered. The systematic investigation of amorphous samples presented herein demonstrates

quantification of constituent elements, particularly lithium. Stoichiometric ratios relative to all elements (Li+Fe+P+O) and to the stable element (Fe) were calculated; P and O reveal reverse behavior against laser power. Li, on the other hand, after considering its migration, increases with rising laser power.

Even though APT measurements at cryogenic temperatures (60 K) were performed, migration of Li ions in some LFP states was observed. In response to the applied measurement fields, Li ions are undoubtedly redistributed. In the amorphous LFP material, we observe a strong Li gradient towards the tip front, which hinders reliable analysis. Obviously, during measurement, Li is drawn towards the tip front and this effect increases with increasing laser power. The remaining host elements, Fe, P, and O, remain homogeneously distributed. New unique insights into the mechanisms of Li movements are provided. Li is pulled and Li enrichment/depletion regions are observed. A new term "Li shooting" is addressed to describe these Li movements. It is demonstrated that the ions indeed experience a field-dependent drift. By mathematically modelling the resulting composition profiles, the Li diffusivity is quantitatively evaluated. In a direct comparison between the amorphous and the crystalline LFP films of identical chemical composition, it is shown that the diffusivity of the amorphous structure is orders of magnitude faster than that of the crystalline state at a temperature of 60 K.

Most notably, this is the first study to investigate the capabilities of APT in LFP at different de-/lithiation states. Li compositions show a wave-like distribution as a result of existence the Li rich/poor phases. 3D iso-surfaces and 2D orthoslices were provided to differentiate between the two phases. Li, in the fully lithiated phase, reaches its ideal stoichiometric ratio, while it is overestimated in the fully delithiated phase. Obviously, the thin films include inactive LFP regions. They were highlighted in this thesis for the first time by atom probe analysis. To quantify the two-phase nature of LFP, statistical analyses of the dis/charged LFP at different lithiation states were performed. Observed frequency distributions of the concentrations of small clusters were compared to the binomial distributions and discussed in detail. Deviations between observed and binomial distributions were represented in the Pearson coefficient to demonstrate the phase separation in the atom probe analysis. Our results provide an evidence to statistically understand the local microstructure evolution in battery materials, which is a pivotal characteristic of battery performance. On the other hand, APT has shown some constraints to microscopy differentiate between the two phases. Although APT measurements were performed at cryo-temperature, Li showed a displacement during measurements. Contrastingly, most of materials are fractured early at ultra low temperatures.

Kurzfassung

Die Speicherung von elektrischer Energie ist eine große technische und wissenschaftliche Herausforderung der Gegenwart. Die zurzeit höchste Energiedichte (Energiemenge pro Volumen Wh kg^{-1}) wird in Lithium-Ionen-Akkus erreicht. Diese Batterien haben den Einzug in nahezu alle akkubetriebenen Geräte unseres Alltags erhalten. Für die Elektromobilität werden jedoch noch höhere Energiedichten benötigt. Die Verbesserung der Technologie erfordert jedoch ein fundamentales Wissen über die atomaren Vorgänge in den beteiligten Materialien. Da das leichte Element Lithium eine herausragende Rolle spielt, ist eine Identifikation desselbigen erwünscht bzw. notwendig. Allerdings ist die qualitative und quantitative Untersuchung von Lithium für herkömmliche metrologische Untersuchungsmethoden eine große Herausforderung, Bedingt durch sein geringes Atomgewicht und die geringe Zahl an Elektronen besitzt Lithium nur einen geringen Streufaktor für elektromagnetische Wellen und ist damit nicht durch Röntgenstrahlung in der Umgebung schwererer Element detektierbar. Dies gilt nicht für Neutronenbeugungsverfahren, die aber ungleich aufwendiger sind. Auch durch andere Standardverfahren der Materialanalytik wie die Energiedispersive Röntgenspektroskopie (EDS) und die Elektronenenergieverlustspektroskopie (EELS) können nicht zur Quantifizierung benutzt werden. Deswegen war es Ziel dieser Arbeit, den Ionentransport innerhalb des Kathodenmaterials Lithium-Eisenphosphat ($LiFePO_4$) mit Hilfe der Atomsondentomographie atomar zu untersuchen und zu quantifizieren. Dazu wurden dünne amorphe LFP-Schichten durch Ionenstrahl Sputterdeposition unter kontrollierten Bedingungen hergestellt und durch einen anschließenden Auslagerungsprozess in einem Vakuumofen in den kristallinen Zustand überführt. Die elektrochemischen Eigenschaften des amorphen und des kristallinen Zustands wurden durch zyklische Voltammetrie charakterisiert. Für die Atomsondentomographie schwer zugängliche Struktureigenschaften wurden durch begleitende Röntgenbeugungsuntersuchungen (XRD) und Transmissionselektronenmikroskopaufnahmen (TEM) gewonnen. Die kristallinen LFP-Proben zeichneten sich durch eine hohe Zyklenfestigkeit von über 7000 Zyklen mit einer Retention > 92 % aus, während die amorphe Phase keine

elektrochemische Reaktion aufwies. Der Vorgang der Interkalation von Lithium in den dünnen LFP-Schichten wurde als Funktion der Filmdicke (25 - 250 nm) untersucht. Die Interkalationskinetik wurde in Cyclovoltammetrie-Experimenten mit Abtastraten von 0,004 bis 400 $\mathrm{mV\,s^{-1}}$ quantifiziert.

Die beobachtete Kinetik kann durch eine modifizierte Version der Randles-Sevcik-Gleichung beschrieben und durch zwei verschiedene Diffusionsregime erklärt werden, was den Rückschluss auf eine Zweiphasenreaktion erlaubt. Für die dicksten gesputterten Schichten wurde eine signifikant langsamere Li-Diffusion beobachtet. Die gemessene Abhängigkeit des Spitzenstroms von der Schichtdicke wird durch die Vergrößerung der Korngrenzfläche (GB) erklärt. Im Gegensatz dazu, konnte keine Abhängigkeit der Überspannung von der Schichtdicke festgestellt werden. Es ist weniger Spannung erforderlich, um einen Strom gleicher Stromstärke in dicken Filmen zu erzeugen. Die Korngrenzen stellen eine elektroaktive Grenzfläche dar, die für die Überspannung verantwortlich ist. Deshalb wirken die Korngrenzen als schnelle Leitungswege und sorgen für eine schnellere Li-Ionen-Diffusion entlang der internen Grenzflächen. Somit wird der Gesamtionenstrom durch die akkumulierte Korngrenzfläche und nicht durch die Querschnittsfläche (Dünnfilmoberfläche) der Schicht gesteuert.

Die erzeugten $\mathrm{LiFePO_4}$ (LFP) Proben wurden mit der laserunterstützte Atomsonden-Tomographie (APT) untersucht. Die Abhängigkeit der quantitativen Ergebnisse von der Laserleistung wurde in einer systematischen Parameterstudie mit Hilfe der amorphen Proben charakterisiert. Die resultierenden stöchiometrische Verhältnisse in Abhängigkeit der Laserleistung wurden relativ zu allen Elementen (Li+Fe+P+O) und relativ zum Eisen (Fe) berechnet. Der Anteil an gemessenen Phosphor und Sauerstoff zeigt ein inverses Verhalten relativ zur genutzten Laserleistung auf. Die gemessene Menge an Lithium nimmt hingegen, nach Berücksichtigung einer anfänglichen überproportionalen Verdampfungsrate, mit steigender Laserleistung zu.

Obwohl die APT-Messungen bei sehr tiefen/kryogenen Temperaturen (60 K) durchgeführt wurden, wurde in einigen LFP-Zuständen eine Migration von Li-Ionen an die Oberfläche der Probe beobachtet. Bedingt durch die sehr hohen Spannungen und resultierenden Feldstärken während des Experiments kommt es offensichtlich zu einer Umverteilung der Li-Ionen. Dies äußert sich im amorphen LFP-Material durch einen erheblichen Konzentrationsgradien-

ten der Li-Ionen relativ zur Spitzenoberfläche. Dieses durch die Messmethode artifiziell erzeugte Signal beeinträchtigt eine zuverlässige Analyse. Die Mobilität der Lithiumionen nimmt relativ mit der eingesetzten Laserleistung zu und führt zu einer verstärkten Diffusion der Li-Ionen an die Oberfläche. Die verbleibenden Matrixelemente Fe, P und O bleiben hingegen homogen verteilt.

Durch die durchgeführten Untersuchungen werden neue Erkenntnisse über das Diffusionsverhalten von Li in dünnen Schichten gewonnen. In der Volumenanalyse der APT Daten können Li-Anreicherungs- und Verarmungszonen beobachtet werden, die Rückschlusse auf den Transport erlauben. Durch mathematische Modellierung der resultierenden Kompositionsprofile wird die Li-Diffusions quantitativ bewertet und eine feldabhängige Triebkraft identifiziert. Im direkten Vergleich der amorphen und der kristallinen LFP-Proben wird ersichtlich, dass das Diffusionsvermögen der Lithiumionen in der amorphen Struktur um Größenordnungen schneller ist als das im kristallinen Zustands bei einer Temperatur von 60 K.

Dies ist vor allem die erste Studie, die die Fähigkeiten von APT in LFP bei verschiedenen De-/Lithiierungszuständen untersucht. Die gemessenen Volumenzusammensetzungen zeigen aufgrund der Existenz der Lirich/Poor-Phasen eine wellenförmige Verteilung. Zur Unterscheidung der beiden Phasen wurden 3D-Iso-Konzentrationsflächen und zweidimensionale Konzentrationsschnitte (Orthoslices) erstellt. Die Lithiumkonzentration erreicht in der vollständig lithiierten Phase das erwartete stöchiometrische Verhältnis, während es in der vollständig delithiierten Phase immer noch eine signifikante Konzentration, entgegen der Erwartung, aufweist. Im delithiierten Zustand zeigen sich inaktive LFP-Regionen. Diese Regionen werden im Rahmen dieser Studie anhand der volumetrischen Daten analysiert. Dazu wurden Proben mit variierenden Beladungszuständen geschaffen und vermessen. Die Größenverteilung dieser speziellen Regionen wurde mit der Clusteranalyse bestimmt und die bestimmte Verteilung mit einer Binomialverteilungen verglichen. Die sich ergebenden Abweichungen zwischen beobachteter Verteilung und der Binomialverteilungen werden durch den Pearson- Koeffizienten quantifiziert, um die Phasentrennung mathematisch zu untermauern.

1 Introduction

Human life is highly dependent on a limited supply of fossil fuel. Some have considered fossil fuels as the cornerstone of the industrial revolution that has changed all life aspects [1]. On the other hand, the global consumption of such fuels leads to a devastating influence on human health and climate [2]. The hidden costs of fossil fuels cannot be clearly represented in their markets; even so their negative impacts. That's why there's a strong motivation, to find a replacement for these fossil fuels [3]. 'We have to find a way to liberate society from that dependence' says John Goodenough, the father of Lithium Ion Batteries (LIB) [3]. Therefore, many efforts have been made to find environment-friendly energy sources [4].

A reliable energy storage system, Lithium Ion Batteries (LIB), has been coming close to this trend. LIB have not only driven changes in our life, portable electronics, and emission-free electric vehicles, but also drained attention for space exploration missions [3, 5, 6]. Today, LIB's world market is remarkable. Therefore, much research is devoted to developing battery cells and modules that result in significantly lower battery cost, longer life, and better performance.

A battery is a device that converts chemical energy into electrical energy [7]. Batteries are sorted into two main categories, non-rechargeable and rechargeable batteries. Non-rechargeable primary batteries have an irreversible chemical reaction; contrary to rechargeable secondary batteries. The chemistry of rechargable LIB depends on a reversible redox reaction between two electrodes in an electrolyte. Thanks to their potential of providing a high-energy density compared to the traditional batteries such as lead acidic batteries, LIB have attracted much attention [8]. Electrode materials are considered the cornerstone in establishing the overall properties of batteries. The prerequisite condition to accept battery materials depends basically on their capacity for efficient reversible extractions/insertions of lithium ions in some suitable lattice sites, i.e., reduction-oxidation (redox) reaction [4, 9, 10].

Lithium Cobalt Oxide (LCO) and Lithium Iron Phosphate (LFP) are the most common battery materials. Although LCO has high energy density [11, 12], LFP attracts much interest due to its cyclic stability [13–16]. LFP has played the key role in the battery science since introducing it as a low-cost cathode in 1997 by Padhi et al [15, 17]. On account of its high specific capacity, excellent cyclic stability, environmental benignity, and inexpensiveness, LFP has attracted exceptional attention [13, 15–17]. Furthermore, its thermostability at high temperature makes it desirable for high-temperature applications such as long distance electric vehicles.

LFP displays an olivine-type structure with a theoretical capacity around 170 $\mathrm{mAhg^{-1}}$ [16]. LFP charging and discharging can be electrochemically described by

$$\mathrm{LiFePO_4} \rightleftarrows \mathrm{Li^+} + \mathrm{e^-} + \mathrm{FePO_4} \tag{1.1}$$

during redox reactions; Li ions are intercalated in the host lattice, while the electro-neutrality of the host is preserved by adding electrons from the external circuit [9]. In the negative electrode, the active material, most simply lithium, is responsible for the accommodation and release of Li ions. Li ions migrate through an electrically insulated electrolyte.

$$\mathrm{Li} \rightleftarrows \mathrm{Li^+} + \mathrm{e^-} \tag{1.2}$$

Lithium intercalation is considered to be the pivotal of the energy storage systems, therefore understanding of the Li movements is the essence of the battery development [18]. However, even for well-studied lithium insertion compounds such as LFP, little attention has been given to reveal its properties in a three-dimensional sub-nanometer spatial resolution. It is profoundly unclear how the nucleation and diffusion mechanisms during delithiation/lithiation occur. This shift towards the study of the local microstructural evolution is driving the current development of batteries [10]. Understanding of the nanoscale distributions of all battery's compounds -especially Li positions and transport paths has a crucial role on the local ion transport processes that differ during transformation in individual grains [19]. This is of great significance. In this thesis, the interfacial reactions and ionic transport on a microscopic, even on atomic level, were studied.

Regardless of the continued advances in electron microscopes, which have a great opportunity to deliver compositional and bonding maps in a two dimensional system, it gives poor information of the 3D nanoscale, for instance grain boundaries in the atomic resolution [20]. Because of the TEM electrons being passed through the samples, transmitted signals can be overlapped and convoluted, making it difficult to accurately interrogate specific features -in particular light elements like lithium [21].

In chemical analysis, it is a dream to identify and locate every single atom. This dream has been becoming true at least for suitable materials by Atom probe tomography (APT). The evolution of the APT started by Erwin Müller in 1952 with his invention "Field Ion Microscopy (FIM)" [22, 23]. APT is the only technique which has the ability to detect chemical elements in a 3D single atomic level [22, 24–26]. Since it can provide detailed microstructural information, APT has received remarkable progresses until it reached the modern Local Electrode Atom Probe (LEAP) with its wide viewing angle [22]. Laser-assisted evaporation mode has opened a broad range of potential materials e.g. oxide ceramics [25]. Field evaporating of ions by laser pulses was introduced by Kellogg and Tsong. At the beginning, the idea faced rejection from the scientific society in view of the unreliable nature of pulsed lasers. By contrast, modern reliable laser-assisted APT has found a wide acceptance.

Tomography in the Greek language means a technique to reconstruct an object [27]. As opposed to surfaces, tomography points out the inner volume. In its narrow meaning, tomography refers to techniques which have the ability to collect views of an object from different directions and construct a 3D representation. Tomography in its general meaning includes all techniques that use sectional views (not only projections) by which the three dimensional reconstruction is reassembled [27]. The reconstruction is a conclusion process to the missing z-information of an object in a three dimensional space. Usually, three dimensional reconstruction is a mathematical method to recover the missing z-dimension. This can be done by retrieving the z values of the voxels. A voxel (volume element) is defined as the individual picture element of an image, which has dimensions in the x and y plane, and includes the thickness as the third dimension (z axis).

The stronghold of APT is the ability to chemically identify the atoms that are field-evaporated from the specimen by time of flight spectrometry and to localize their positions by a position sensitive detector. The key features of APT have been elucidated by A. Cerezo et al. in his review [26]. The review discussed GaInN quantum wells identification by the transmission electron microscopy and the atom probe tomography. TEM has blindly seen the quantum wells; contrary, APT has been able to reveal the indium clustering and the chemical information of each atom [26].

The systematic studies presented herein explore the possibilities of applying APT to the atomic-scale structure of LFP and its battery function. Furthermore, issues associated with APT for LFP and more broadly complex oxides, provide further insights into the material behavior during laser assisted field evaporation. With this in mind, the first evidence for achieving unambiguous 3D subnanometre scale spatially resolved mapping of Li, Fe, P, and O is provided. Moreover, Li de-/intercalation into thin films of LFP were studied. APT results from as-fabricated, crystalline, powdered or multilayers LFP/Fe system, lithiated and delithiated LFP are compared to obtain insights towards Li distributions. This is of a great significance because Li distributions are vital in formulating relationships between microstructure and properties. High quality thin films/tips were produced by ion beam sputtering, a technique which provides well defined thin films of low surface roughnesses [14]. X-ray diffraction (XRD) and Transmission Electron Microscope (TEM) were used to observe the thin films structural, while electrochemical characterization and three dimensional microscopy were obtained by means of Cyclic Voltammetry (CV) and Atom Probe Tomography (APT).

Following a brief introduction of the LFP material in chapter 2, phase transformations and the electrochemical behavior of LFP are presented. The theoretical principles of APT in addition to FIM are then illustrated. At the end of the chapter, concepts of the reconstruction technique and data analyses are explained. In the next part, experimental details are clarified in chapter 3.

The primary goal of this work is to check the possibility of measuring the phase decomposition in LFP, nucleation and diffusion mechanisms during delithiation/lithiation processes using APT. Prior to APT, the electrochemical activity of LFP thin films was checked and outlined in chapter 4. In a first step, rate capability, cycle stability, capacity retention were tested, and Li transport relative to the grain boundaries was discussed thereafter.

Evaporation field of LFP using bi-layers and multilayers was determined by APT. Three-dimensional chemical maps of lithium are explored at the atomic spatial resolution and correlated to the distributions of the transition metal cation (Fe), phosphorous, and oxygen in chapters 5 and 6. Stoichiometric ratios in amorphous phase were quantified in chapter 5. Comparison of amorphous and crystalline LFP phases relative to the applied laser power is then given. Local Li enrichment against the applied laser power in both phases are discussed and mathematically modelled in chapter 5. Dis-/charged LFP at different de-/lithiation states are discussed in chapter 6. At the end, statistical analyses of elemental distributions in LFP at different de-/lithiation state are discussed.

2 Theoretical Concepts

2.1 Crystal structure of LFP

The phospho-olivine-type structure of $LiFePO_4$ with an orthorhombic unit cell is shown in Figure 2.1. The figure shows four units cells of $LiFePO_4$. Oxygen ions form a hexagonal close-packed configuration. The Fe ions form zigzag chains of octahedrons bridged by the tetrahedral phosphate groups (PO_4). Lithium atoms are settled on octahedral sites in between oxygen. Lithium ions, on the other hand, move in one dimensional tunnels along the [010] direction in the orthorhombic P_{mnb} lattice. Thus, tunnels aligned parallel to the planes of corner-sharing FeO_6 octahedra. Two neighbouring Li atoms are 0.516 nm far along the a-axis [29]. The whole crystal structure acquires its great stability from the strong covalent bond between the oxygen and P^{5+} ions forming $(PO_4)^{3-}$ units [15]. The antibonding Fe^{3+}/Fe^{2+} state is also stabilized as a result of this strong covalency. Consequently, oxy-

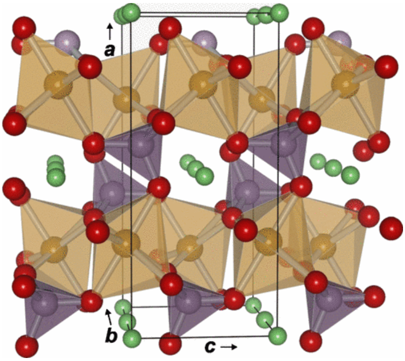

Figure 2.1: Elementary cell of the olivine-type structure of $LiFePO_4$, illustrating locations of Li atoms (green), Fe (yellow), P (violet), and O atoms (red) in the unit cell, tetrahedral of PO_4 and octahedra of FeO_6. After [28].

gen atoms are hard to extract [30]. The Fe/P/O linkage creates a suitable Fe^{3+}/Fe^{2+} redox energy of flat voltage 3.40 V versus Li/Li^+ [31].

2.2 Phase Transformations

Crystal structure and stability of unit cells are of great importance for development of battery materials. Ions inside crystal lattices are influenced by the surroundings, which is why the whole electrochemical processes and potential rely on the crystal structures [32]. Presence and stability of channels for fast transport are an important design element in cathode materials [18]. During the charging/discharging processes of the electrode materials, Li concentrations are varied and accompanied by phase transformations, order-disorder transitions, crystallographic changes and other phase reactions [10, 33]. Thus, battery performance depends on the phase transitions of the electrode materials. Phase transitions, in this respect, are decisive in limiting the high rate capabilities and cycle life of batteries. Microscopic information like phase nucleation and growth is frequently fundamental to the understanding of battery electrodes [10]. Poor rate/cycle performances due to large volume changes and/or large amount of interfaces that are associated with the phase transitions are quite known problems [10]. Any differences in lattice parameters between the two phases participating in the phase transformation introduce coherency strains, which affect the thermodynamic potentials such as the Li chemical potential and the overall free energy. This, in turn, can modify the boundary composition of any two-phase coexistence regions and, in consequence, the voltage profile in which two-phase coexistence becomes obvious by voltage plateaus [34]. Olivine $LiFePO_4$ is well known for its two phase reaction and characterized by a flat voltage plateau [35]. The two phase reaction leads to heterogeneous coexistence of two phases in which the passage through coherent or semicoherent interface may limit the diffusion of Li atoms [34]. Electrochemical kinetics are directly dependent on the phase transition mechanism and/or miscibility gaps between the two phases of crystallites [33].

The flat voltage plateau can be justified from the Gibbs free energy [36, 37]. The open-cell voltage $\boldsymbol{V_{oc}}$, according to the Nernst equation, is the difference of the Li chemical potentials between the anode ($\boldsymbol{\mu_{Li}^{anode}}$) and the cathode ($\boldsymbol{\mu_{Li}^{cathode}}$)

$$V_{oc} = \frac{\mu_{Li}^{cathode} - \mu_{Li}^{anode}}{e} \tag{2.1}$$

where $\boldsymbol{e}$ is the elementary charge, and $\boldsymbol{\mu_{Li}}$ is the Li chemical potential.

2.3 Electro-chemical behavior of LFP

LFP ($LiFePO_4$) is a triphylite like compound with 170 mAh/g theoretical capacity. In spite of its poor electronic conductivity, LFP is a very attractive cathode material of low costs. LFP shows a stable crystalline structure in almost all commonly used electrolytes. Robust crystal structures together with sufficient storing sites are the main factors to get a high specific capacity with a long cycle life [38, 39]. LFP is capable of reversibly insert/deinsert one lithium ion per iron atom at a moderate operating flat voltage 3.50 V versus Li^+/Li, which is convenient with the common organic electrolytes [40]. Actually, throughout the electrochemical de-/intercalation, Fe^{+2} ions of $LiFePO_4$ are oxidized to Fe^{+3} leaving the olivine $FePO_4$ crystal system intact. Yamada et al. has described the two phase nature of Li_xFePO_4 as a mixture of the Fe^{+3}/Fe^{+2} valent [41]. Extraction of lithium from the triphylite $LiFePO_4$ is accompanied by an approximately (-7%) shrinkage forming a heterogeneous delithiated phase $FePO_4$. The two-phase reaction could be demonstrated by transmission electron microscopy as a disordered region between the crystalline domains accompanied by lattice parameters mismatch [15, 42, 43].

During the delithiation, Li is being removed from the surface creating concentration gradients within the material. These concentration gradients, according to Fick's law Eq. 2.2, drive a diffusion as shown in the schematic diagrams Figure 2.2. In this example, Li is essentially removed from the center to the surface of the particle. The outer depleted zones of the crystal (α) grow inward consuming the (β) phase. So, the rate at which Li ions extracted from inside the particle is determined by the diffusion coefficient D_{Li} within the α-phase or by the interfacial transport through the interface between α and β. Li flux can be identified in terms of the diffusion coefficient as

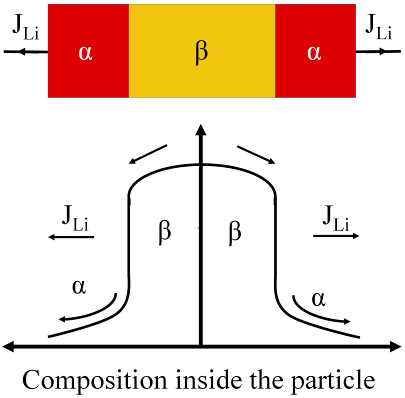

Figure 2.2: Schematic shows the Li composition distribution inside a particle during the delithiation process.

$$J_{Li} = -D_{Li}.\nabla C \tag{2.2}$$

where is $\boldsymbol{J_{Li}}$ the Li flux, $\boldsymbol{D}$ is the diffusivity, and $\nabla \boldsymbol{C}$ is the concentration gradient.

Because of the coexistence of the two phases, the delithiated phase (α) and the lithiated phase (β), an abrupt jump in composition exists as shown in Figure 2.2. The two phases have not only different compositions, but also different lattice parameters. The fully lithiated (β) phase has a larger lattice parameter.

Li ions in Li_xFePO_4 can in principle migrate only along one-dimensional channels parallel to the [010] direction [46, 47]. So, the b-axis in the P_{nma} symmetry group notation is the expected preferable diffusion direction, while similar continuous chains of LiO_6 octahedra are missing in the direction of the a-axis and c-axis [48]. Nishimura et al. has experimentally observed the directed Li-ion transport path along the [010] axis [44]. Figure 2.3 represents the delocalization path along the [010] direction as blue contours. Elementary analysis for the interface separating the Li rich/poor phases would therefore suggest that the interface has to be preferably perpendicular to the b-

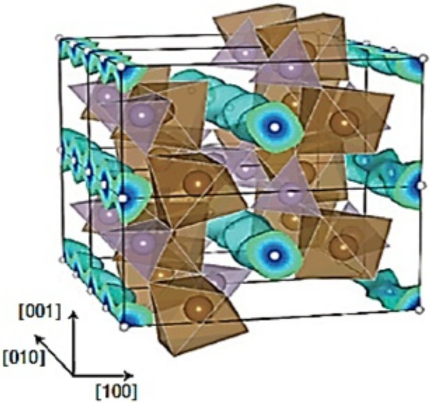

Figure 2.3: Schematic shows the Li distribution by blue contours, whereas the brown octahedra represents FeO_6 and the purple tetrahedral represents PO_4 units. After [44].

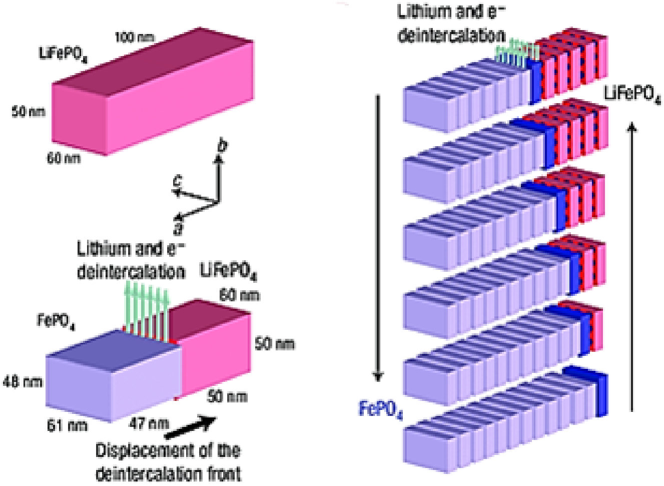
LiFePO₄
100 nm
50 nm
60 nm
b
c
a
Lithium and e⁻ deintercalation
LiFePO₄
60 nm
FePO₄
50 nm
48 nm
50 nm
61 nm
47 nm
Displacement of the deintercalation front
Lithium and e⁻ deintercalation
LiFePO₄
FePO₄

Figure 2.4: Schematic of the 'domino-cascade' model shows the de/intercalation processes in the LFP. After [45].

direction. In other words, the b-direction allows a uniform extraction/insertion of Li ions from surfaces perpendicular to the diffusion direction [34, 49] (see Figure 2.4). Inevitably, interfaces may limit the Li diffusion, which indicates that the electrochemical kinetics is controlled by the phase transformation [33]. De/intercalation in $LiFePO_4$ nanocrystallite was proposed as a domino cascade mechanism by Delmas et al. [45]. Figure 2.4 shows the conceived movement of the interfacial zone in the a-direction, while the Li removal appears in the orthogonal b-direction.

For bigger particles, a core-shell two-phase configuration can be expected. The shrinking core model -adopted by Srinivasan et al. [50]- was introduced to explain the asymmetric behavior during the de-/lithiation processes (see Figure 2.5). The concept of the model is that one of the two phases, fully lithiated or fully delithiated, is initially formed from the surface, while the phase boundary progressively moves towards the core [33]. When $LiFePO_4$ is delithiated, the Li deficient shell wraps around the Li- rich core resulting in shrinking the core and expanding the shell. This process is continued until the core is entirely consumed. The material at the final stage returns as a single phase system. The reaction ends by emptying up all the available sites. The process is reiterated in the opposite direction with a shell of a Li-rich phase covering a Li-deficient core during lithiation. The core shell model and a newer model called the radial model have predicted the deceleration of Li diffusivity when the electrode reactions approach the end [35, 51]. Moreover, the radial model proposed existence of dead $LiFePO_4/FePO_4$ cores at the end stages of the charging and discharging processes [35, 51] (see Figure 2.6). When the limited mobility of Li ions through the interface can't sustain the current density, the electrochemical reaction stops without fully consuming the active materials. The reaction leaves an inactive $LiFePO_4$ inside the two phase reaction during charging and a remnant $FePO_4$ through the discharging [35, 51]. What is more, the core shell model assumes isotropic diffusions for Li ions and phase boundary movement, while in the actual case both Li ions and phase boundary are confined anisotropically in the diffusion direction and the phase boundary movement [52].

In a real battery, electrodes consist of a large amount of particles and the overall phase transitions in all particles define the electrochemical performance of the electrodes. Dreyer et al. [53] assumed that particles are com-

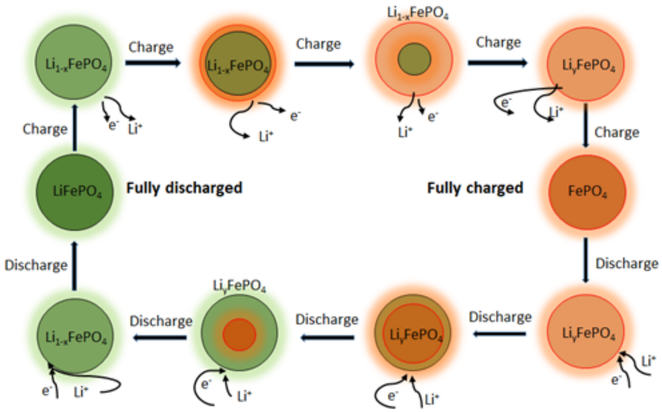
Li1-xFePO4
Charge
Li1-xFePO4
Charge
Li1-xFePO4
Charge
LiyFePO4
e-
Li+
Charge
LiFePO4
Fully discharged
Fully charged
FePO4
Discharge
Discharge
LiyFePO4
Li1-xFePO4
Discharge
Discharge
LiyFePO4
Discharge
LiyFePO4

Figure 2.5: Schematic represents the shrinking-core model in the LFP electrode. After [50].

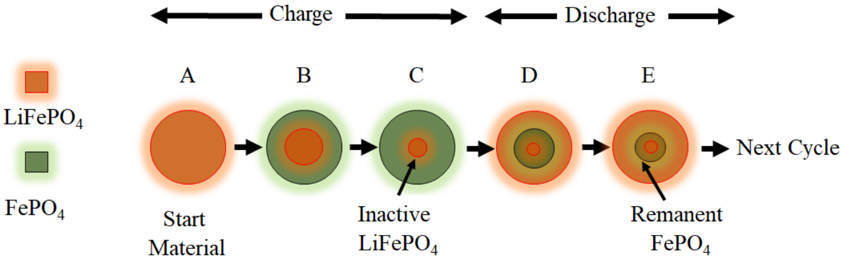
Charge
Discharge
A
B
C
D
E
LiFePO4
FePO4
Next Cycle
Start Material
Inactive LiFePO4
Remanent FePO4

Figure 2.6: Schematic illustrates the ’radial mode’ and its inactive/remnant cores. After [35].

pletely charged individually rather than partial filling of all particles at the same time.

2.3.1 Miscibility gap

In batteries, temperature and pressure are practically constant. Only compositions and electrical potentials vary. By contrast, Li chemical potentials $\mu_{Li}^{cathode}$ and μ_{Li}^{anode} are the axes of the changes. Li chemical potential ***(μ)*** can be identified as the first derivative of the Gibbs free energy ***(G)*** with respect to the number of Li atoms ***(n_e)*** in each electrode, Eq. 2.3 and 2.4. Chemical potentials in both electrodes are related to the electrical potential ***(φ)*** as in Eq. 2.7 and 2.8.

$$\mu_{Li}^{cathode} \approx \frac{\Delta G^{cathode}}{\Delta n_{Li}^{cathode}} \tag{2.3}$$

$$\mu_{Li}^{anode} \approx \frac{\Delta G^{anode}}{\Delta n_{Li}^{anode}} \tag{2.4}$$

$$\Delta G^{cathode} = -n_e F \varphi^{cathode} \tag{2.5}$$

$$\Delta G^{anode} = -n_e F \varphi^{anode} \tag{2.6}$$

Since the number of the transported Li ions (n_{Li}) during the electrochemical reactions is equal to n_e the number of transported electrons in the outer circuit, the Li chemical potentials can be rewritten as in Eq. 2.7 and 2.8.

$$\mu_{Li}^{cathode} = F \varphi^{cathode} \tag{2.7}$$

$$\mu_{Li}^{anode} = F \varphi^{anode} \tag{2.8}$$

Furthermore, the measured voltage is equal to the potential difference between the two electrodes, as written in Eq. 2.9.

$$\varphi = \varphi^{cathode} - \varphi^{anode} = -\frac{\mu_{Li}^{cathode} - \mu_{Li}^{anode}}{eN_A} \tag{2.9}$$

where $\boldsymbol{N_A}$ is the Avogadro's number, and $\boldsymbol{e}$ is the charge of the electron.

Li metal may be used as an anode, which means that μ_{Li}^{anode} sees no change during charging and discharging [35]. For positive electrode (cathode) materials such as $LiFePO_4$, Li insertion induces a first-order phase transition from

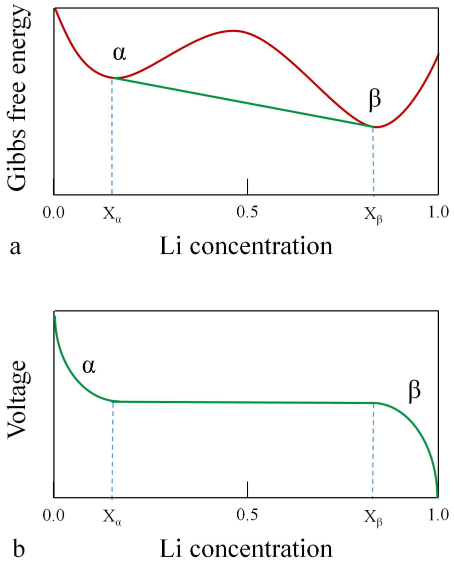

Figure 2.7: (a) Gibbs free energy and (b) the voltage profile as a function of Li concentration for a two phase transition battery material upon de-/ithiation.

a Li poor phase (α) into a Li rich phase (β). The appropriate free energy function is graphically displayed in Figure 2.7 (a). The free energy function for any two phase reaction exhibits two local minima at Li contents x_α and x_β. The free energy of the two phase mixture is then defined upon the common tangent of the free energies of the two phases. This implies that the Li chemical potential μ_{Li} of the material isn't changed between the two free energy wells from x_α to x_β. Therefore, the voltage becomes flat between x_α and x_β [35]. The unchanged plateau voltage indicates a miscibility gap, Figure 2.7 (b).

The width of the miscibility gap is influenced by the substitution in the lattice, and possibly of the crystallite [54]. Omenya et al. [55, 56] reported a reduction of the miscibility gap in view of vanadium substitution that creates a direct distortion of the lattice and disordering of the lithium ions [54].

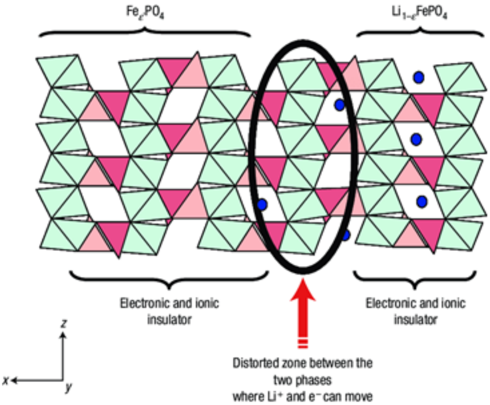
$Fe_{\varepsilon}PO_4$
$Li_{1-\varepsilon}FePO_4$
Electronic and ionic insulator
Electronic and ionic insulator
z
x
y
Distorted zone between the two phases where Li^+ and e^- can move

Figure 2.8: Schematic representing a finite region between the lithiated and the delithiated phases. After [45].

In two-phase reaction materials, once the disordering time of lithium ions is longer than the diffusion time, the system remains a single phase [35].

2.3.2 Interfacial zone

Even though the widespread acceptance of the domino-cascade model [45, 57], it would, however, overlook the interfacial zone between the two phases [52]. The Domino cascade model was introduced by Delmas et al. [45] to describe the phase boundary movements with either lithiated or delithiated phases at the miscibility gap [52]. Thus, the domino-cascade model, has neglected the diffusional transit interfacial zone [35]. The interfacial zone is a finite region composed of neither lithiated nor delithiated phases [58] (see Figure 2.8).

Chen et al. [42] has announced the importance of the boundary and experimentally shown it via a high-resolution TEM as a visible zone on the ac-plane [52]. The zone was observed with varying lithium concentrations [52, 57, 59]. In addition, the size of the interfacial zone (4.20 nm) was found to be independent of the particle size [52]. Furthermore, the phase boundary is not

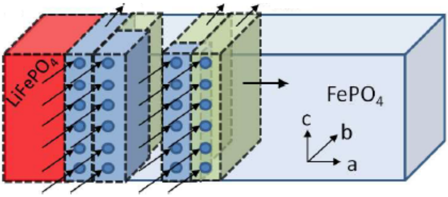

Figure 2.9: Schematic representation of the phase boundary. LiFePO$_4$ phase moves along the a-direction, while Li ions pull in and out the b-direction during dis/charging processes. After [52].

perfectly parallel to the bc plane as a result of the coherency strains [52]. The interfacial zone moves along the a-direction, whereas the paralleled channels are progressively filled by diffusion along the b-direction [52] (see Figure 2.9). It is worth mentioning that Li$^+$ diffusion takes place with different diffusivities in all channels at the same time, Figure 2.9. In addition, channels closer to the LiFePO$_4$ phase represent faster diffusivities than the others away from the LiFePO$_4$ phase until it reaches the zero value around the FePO$_4$ phase [52]. Once the closest channel to the LiFePO$_4$ phase is fully filled, the interfacial zone starts to move one channel distance in the a-direction perpendicular to the Li diffusion direction [52]. With further charging, the interfacial zone moves until a fully FePO$_4$ phase is reached. The process goes into the opposite direction by charging. The high concentration of Li$^+$/vacancies and Fe^{+2}/Fe^{+3} polarons in the interfacial zone are the driving forces of the phase boundary movement that allow the redox reaction to proceed [35].

2.4 Configuration and principle of Li-ion batteries

Two electrodes, anode and cathode, separated by an electrolyte are the main components of Li batteries that determine the performance of the battery. The electrodes are immersed in an electronic isolator (ionic conductor) electrolyte and separated by a polymer membrane. In typical Li-ion batteries, the redox reactions are always accompanied by mass transport and/or volume expansion or contraction [4]. Although the concentration of lithium ions varies in the two electrodes with the degree of charge and discharge state, it remains constant in the electrolyte regardless of the degree of the state [4]. There are three basic principles to store lithium ions in the electrodes: (1) alloying such as silicon [60–62]; (2) conversion such as with CuO [63]; intercalation such as in $LiFePO_4$ [14]. Among all reactions alloying offers the highest specific capacity, but it results in massive volume change [60, 64]. Mechanical stresses and fractures are notoriously recognized for large volume expansions which lead to materials degradation. On account of the bad reversibility of the conversion reactions, their materials are rarely used in lithium ion batteries [65]; conversely, intercalation materials. In intercalation reaction, the host electrode accommodates Li ions between its layers, whereas the electroneutrality is maintained by existence of multivalent ions [4].

2.5 X-Ray Diffraction (XRD)

High angle X-ray diffractometry is a well-known technique to analyze the crystal structure of materials by reflecting the incident x-rays off the atomic layers. Diffracted rays appear only when certain geometrical conditions are fulfilled. Accelerated electrons from a heated tungsten filament (cathode) are collided with an anode normally made from copper, where they produce a continuous X-ray spectrum overlaid with characteristic radiation. A filter made from nickel is used to transmit only one wavelength $\lambda(\text{Cu-K}_\alpha)$ = 1.54059 Å. The X-ray source and the detector orbit the sample along the same circle but move in opposite directions. 2θ is the angle between the detector and the source. An X-ray beam was generated at 40 kV and 30 mA in a sealed copper tube. Scans were conducted with an angular resolution (step size) of 0.01° with a scan time of 1 step s^{-1}. Constructive interference of scattered beams can be predicted using the Bragg's law [66, 67]:

$$n\lambda = 2dsin\theta \tag{2.10}$$

where, $\boldsymbol{n}$ is an integer, $\boldsymbol{\lambda}$ is the characteristic wavelength of the X-ray beam, $\boldsymbol{\theta}$ is the angle of the X-ray beam with respect to the planes, and $\boldsymbol{d}$ is the spacing between the planes.

Analysis of the scattering angles of the diffracted beams reveals the size, shape, and orientation of the crystallographic unit cell. For the orthorhombic structure of LFP, ***d*** spacing can be calculated using the following equation:

$$\frac{1}{d^2} = \frac{h^2}{a^2} + \frac{k^2}{b^2} + \frac{l^2}{c^2} \tag{2.11}$$

where ***(h,k,l)*** are the Miller indices and ***a, b, c*** are the lattice constants.

Scherrer [68] showed that the mean dimension ***D*** of the crystallites is related to the angular reflection broadening ***(β)*** by

$$D = \frac{0.89 \cdot \lambda}{\beta cos(\theta)} \tag{2.12}$$

2.6 Transmission Electron Microscope (TEM)

Because of its ultrashort wavelength, electrons are used to obtain microscopic images in high resolution. Electrons wavelength ***(λ)*** can be stated when taking the relativistic effect into account as [70]:

$$\lambda = \frac{h}{\sqrt{2meU_{AC}(1 + \frac{eU_{AC}}{2mc^2})}} \tag{2.13}$$

where ***h*** is the Planck's constant, $\boldsymbol{U_{AC}}$ is the acceleration voltage, ***e, m*** are the charge and the rest mass of the electron, respectively, and ***c*** is the speed of light.

An acceleration voltage of 200 kV produces a wavelength 2.51 x 10^{-12} m. This means that subatomic features are, in principle, measurable. Resolution of wave optics is calculated from

$$\delta = \frac{0.61 \cdot \lambda}{n \cdot sin(\alpha)} \tag{2.14}$$

where ***δ*** stands for the resolution and ***n·sin(α)*** represents the numeric aperture of the optics.

An electron source, in this study a field emission gun, emits a beam of electrons, which is accelerated by a high voltage. A thin sample is exposed to

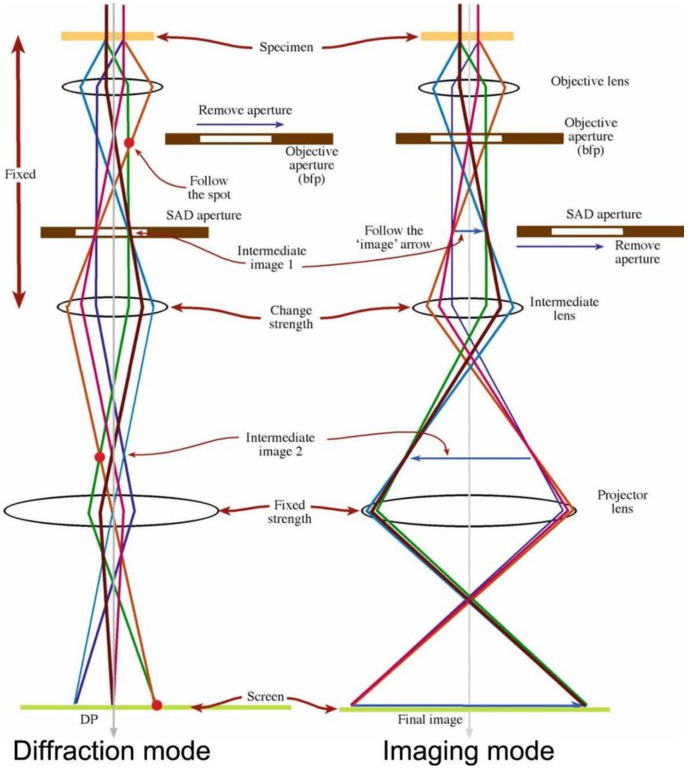
Specimen
Objective lens
Remove aperture
Objective aperture (bfp)
Objective aperture (bfp)
Fixed
Follow the spot
SAD aperture
SAD aperture
Follow the 'image' arrow
Intermediate image 1
Remove aperture
Change strength
Intermediate lens
Intermediate image 2
Fixed strength
Projector lens
Screen
DP
Final image
Diffraction mode
Imaging mode

Figure 2.10: Schematic diagram of a TEM setup. Left: diffraction mode, Right: imaging mode. After [69].

a beam of accelerated electrons, uniformly over the illuminated area. The transmitted beam is magnified and focused by a system of magnetic lenses and apertures. As the electrons travel through the sample, they are either scattered or transmitted. This results in a heterogeneous distribution of electrons, which contains the microstructural information of the sample. In the bright field imaging, the diffracted electrons deflected away from the axis of the microscope are blocked using selected apertures. Thus, the transmitted electron beam generates a contrast on the fluorescent screen depending on

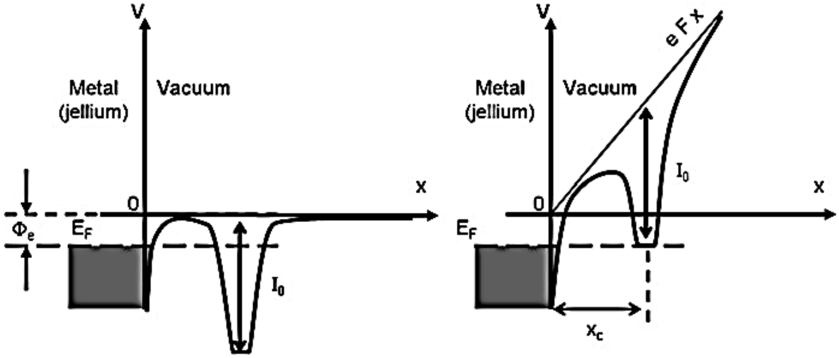

Figure 2.11: Electron's potential energy diagrams, (left) in absence of the applied electric field, and (right) in presence of the applied electric field. x is the distance to the surface of an electron from a gas atom in the vicinity of a tip, I_0 is the energy of the first ionisation, x_c is the critical distance of ionisation, E_F is the Fermi energy and Q_c is the work function of the surface. After [71].

local lattice orientation and mass density. The intensity of the diffraction depends on the orientation of the planes in the crystal relative to the electron beam. Angular distribution of the electrons due to diffraction can be viewed in the form of diffraction patterns, and the spatial distribution of electrons can be observed as a contrast in images of the sample. A simplified representation is depicted in Figure 2.10. A CM200FEG (Philips) TEM was used to check out the samples in this work.

2.7 Field Ionization

Field ionization is the process of removing an electron from its atom in strong electric fields. Figure 2.11 schematically illustrates the idea of the ionization in the form of energy diagrams. The potential energies of a gas atom in absence and presence of a high electric field in the vicinity of metal surface are shown.

To remove a confined electron from a symmetrical potential well, ionization energy (I) has to be paid. In presence of an inhomogeneous electric field, a deformed asymmetrical potential well is established, whereas the potential barrier is reduced. Consequently, a finite potential barrier close to the metal surface is formed, which can be penetrated with a given tunneling probability by an outer shell electron. The energy of such electron has to be above the Fermi level of the metal. Therefore, the process can only take place at a critical distance X_c between the gas atom and the metal surface. Below the critical distance X_c, all the electronic levels in the metal are occupied, which forbids any tunneling. This critical distance can be quantified as:

$$X_c = \frac{I - Q_c}{eE} \tag{2.15}$$

where $\boldsymbol{I}$ is the first ionization energy, $\boldsymbol{Q_c}$ is the work function of the metal, $\boldsymbol{e}$ is the charge electron and $\boldsymbol{E}$ is the electric field.

Upon further increase of the applied voltage, surface irregularities are being blotted out.

2.8 Field Evaporation

Atom plucking out from its own lattice is known as field evaporation. A very intense electric field leads to a combination of ionization and desorption of an atom from its surface. Upon exposure of a high electric force, surface atoms are being ionized and escape over an energy barrier that is reduced by the electric field. Afterwards, the ionization of those atoms, evaporation events are pursued immediately. In APT, ionization is induced by a standing electrostatic field (DC) combined with either a high voltage or laser pulse applied at the specimen apex.

After being polarized by a sufficient electric field, surface atoms are pulled away from the surface, while their outer shell electrons are drained into the surface. Figure 2.12 shows the transition from an atomic to an ionic state as a function of the distance from the surface. Two main phenomenological theories have been offered to describe the critical evaporation field. In Müller's proposal, atoms become fully ionized at a critical distance before escaping

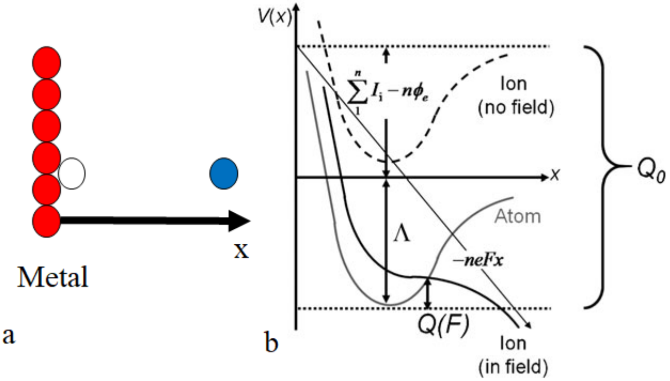

Figure 2.12: Schematic depicts the removal of a surface atom and the transition from the neutral atomic state (red) to the ionic state (blue). Atomic and ionic potential energy V(x) with and without electric field as function of the distance from the surface. Λ is the sublimation energy, n is the degree of ionisation, I_i is the ith ionisation energy, ϕ_e is the work function of the surface ion, Q_0 is the energy barrier without the electric field and Q(F) is the energy barrier with electric field. After [72].

from the surface. Such model is renowned as the image hump model [73]. In Gomer's proposal, the charge is progressively drained out during surface escaping [74]. Although both ideas contradict each other for the moment of ionization of the escaping atom, they have recognized the way of evaporation. Field evaporation occurs when the surface atoms get sufficient energy to overcome the energy barrier that constrain it to the surface. This kind of energy was identified as the thermal agitation energy. Figure 2.12 (a) represents the removal of a surface neutral atom (red) to an ion (blue). The evaporated ions are subsequently accelerated by the electric field. As a function of the distance from the specimen's atom, three different potential energy curves are shown in Figure 2.12 (b). One curve illustrates the potential energy of the neutral atom, while the others represent the ion's energy in case of absence and existence of an electric field. The minimum energy of the ion has a higher energy than the neutral atom. Therefore, the transition from the atomic state to the ionic state is energetically not possible in the field free case:

$$Q_{0(n)} = \Lambda + \sum_{1}^{n} I_i - n\phi_e \tag{2.16}$$

where **Λ** is the sublimation energy, ***n*** is the degree of ionisation, $\boldsymbol{I_i}$ is the ith ionisation energy, $\boldsymbol{\phi_e}$ is the work function of the surface ion, and $\boldsymbol{Q_0}$ is the energy barrier without the electric field. When an electric field is applied, ion's potential energy decreases with increasing the distance (x) from the surface. At a certain distance from the surface, an intersection between the potential energies of the atom and the ion under electric field occurs as shown in Figure 2.12 (b). At this intersection, the activation barrier Q(F) is defined, which can be overcome by thermal agitation. Thus, the atom can be extracted from the surface.

2.9 Field Ion Microscopy (FIM)

Field ion microscopy (FIM) was the first technique that provided an atomic resolution imaging of solid state surfaces. FIM relies on the ionization of an inert gas in the presence of a high electric field. A rare noble gas is introduced to a sharp cryogenically cooled needle specimen [71, 75]. By applying a high electric positive voltage to the sharp needle, an intense electric field, typically of the order of 10^{10} V nm^{-1}, is generated at its surface. The field is adjusted enough to induce ionization of the imaging gas. The electric field E at the surface of the tip apex can be estimated as:

$$E = \frac{V}{\beta R} \tag{2.17}$$

where ***E, V,*** and ***R*** represent the evaporation field strength, the applied voltage, and the curvature radius of the needle's apex, respectively. $\boldsymbol{\beta}$ is a compression factor that is related to the tip geometry. It typically ranges from 5 to 10.

The high electric field and its gradient actuate the gas atoms to be polarized and approached to the tip. After ionization the gas ions are repelled and sub-

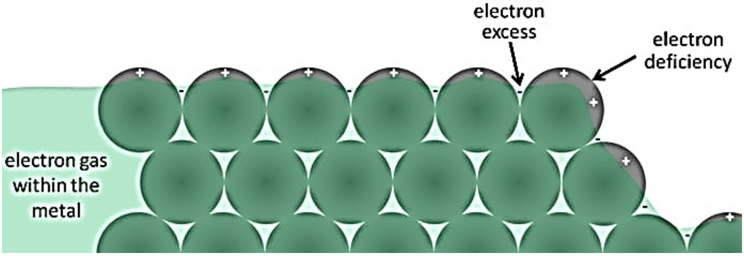

Figure 2.13: Schematic diagram shows a positively charged surface. After [71].

sequently accelerated toward an in-front phosphorous screen. The resultant pattern reflects the distribution of the local field at the tip surface. Indeed, the free electrons are displaced inwards by the high voltages, leaving partly charged atoms at the surface. Yet, the creation of a higher charge density around the protruding atoms is real (see Figure 2.13).

2.9.1 FIM technique

The typical FIM detector consists of a double microchannel plate (MCP) in front of a phosphor screen (see Figure 2.14). The front grounded side of the MCPs acts as ions receiver, whereas the positively charged back side (+ 2000 V) attracts electrons. A further accelerating voltage (+1000 V) is applied on the secondary electrons between the back side of the MCP and the phosphor screen [76]. The accelerated ions are projected normally to the tip surface, following approximately the electric field lines and brightening the phosphor screen, whenever they strike. Eventually, a clear highlighted pattern representing the dynamic constant current of the ionized gas atoms above the tip surface can be seen. This output pattern corresponds to the characteristic crystallographic projection of the prospective material. The lateral resolution is increased by reducing the lateral motion of the atoms by cryogenic temperatures.

In considering the phosphor screen at a distance $\boldsymbol{L}$ from the tip, the magnification $\boldsymbol{M}$ of the image can be generalized as

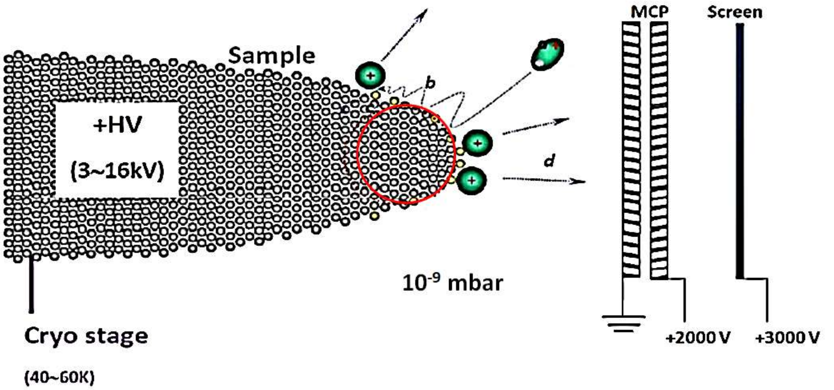

Figure 2.14: Schematic diagram illustrates the field ion imaging.

$$M = \frac{L}{\xi R} \tag{2.18}$$

where $\boldsymbol{R}$ is the radius of curvature of the tip and $\boldsymbol{\xi}$ is the image compression factor (ICF).

Imaging gas atoms accelerate and fly nearly but not exactly along the electric field lines. ICF takes into account the actual surface deviations from a sphere shape. So the ICF can be defined as the ratio between the observed $\boldsymbol{\theta_{obs}}$ and the theoretical $\boldsymbol{\theta_{crys}}$ angles of two crystallographic orientations. These angles are represented in Figure 2.15.

$$\xi = \frac{\theta_{obs}}{\theta_{crys}} \tag{2.19}$$

In this work, the FIM is mainly used to develop a smoothed rounded surface, and further essential geometrical operators -tip radius and shaft angle- can be measured or estimated. As it is shown in Figure 2.16 (a), by counting the number of rings ***(n)*** between two poles $\boldsymbol{(h_x k_x l_x)}$ making an angle $\boldsymbol{(\theta)}$, the tip radius ***(r)*** is calculated with the relation.

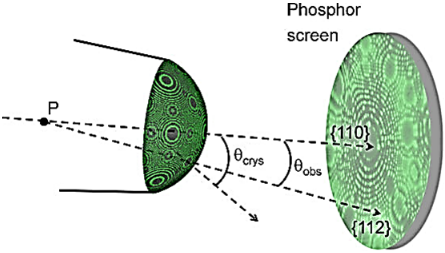

Figure 2.15: Schematic represents the point-projection of surface atoms in a specimen [71].

$$r_t = \frac{n.d_{h_1k_1l_1}}{1-cos\theta} \tag{2.20}$$

In case of tungsten, the interplaner distance $\boldsymbol{d_{hkl}}$ is commonly determined by

$$d_{hkl} = \frac{a}{\sqrt{h^2+k^2+l^2}} \tag{2.21}$$

$$cos(\theta) = \frac{h_1h_2+k_1k_2+l_1l_2}{\sqrt{h_1^2+k_1^2+l_1^2}\cdot\sqrt{h_2^2+k_2^2+l_2^2}} \tag{2.22}$$

During the field evaporation process, the radius of curvature, known as the curvature evolution, increases in size. As seen in Figure 2.16 (b), by simple geometry, the shaft angle $\boldsymbol{\alpha}$ can be determined as

$$sin(\alpha) = \frac{R_2-R_1}{\sqrt{R_2-R_1+nd_{hkl}}} \tag{2.23}$$

2.10 Atom Probe Tomography (APT)

By combining the Field Ion Microscope (FIM) and time of flight mass spectroscopy, Müller et al. [77] has developed what today's APT would look like.

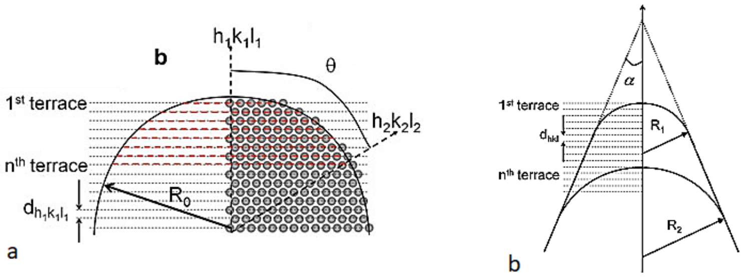

Figure 2.16: Schematic views of (a) lattice planes. (b) the radius curvature evolution. After [71].

Needle shaped specimens are subjected to high positive voltages, high electric fields are created on the specimen's apices then atoms are evaporated [72]. In traditional electrical atom probe tomography (HV-APT), investigated materials are conducting, which has a limitation for ceramic and oxide materials. Implementation of photon-assisted field evaporation by using ultrafast lasers has been a remarkable breakthrough for wide spread applications of APT to nonconducting materials. On account of triggering field evaporation of sample atoms, focused laser pulses are applied to the tip apex beside a base voltage V_{DC}. Among all of the various mechanisms that have been proposed to describe the physics of the laser assistance, activation by thermal pulsing is now widely accepted [22, 72]. After being absorbed, laser pulses locally heat the apex to trigger the field evaporation. In dependence of the thermal conductivity of materials, temperatures are shortly rising and cooling between the laser pulses. The heat flux can be mathematically expressed as a function of the thermal conductivity and the temperature gradient.

$$\vec{J} = -K \cdot \vec{\nabla} T \tag{2.24}$$

where $\boldsymbol{\vec{J}}$ is the heat flux flowing per second per unit area. $\boldsymbol{K}$ is the thermal conductivity, and $\boldsymbol{T}$ is the temperature gradient.

Cooling down of surface atoms has the opportunity to decrease their lateral velocity during the evaporation process. Diffusion of atoms at the sample surface through a thermally activated process cannot completely be avoided

[71]. Cryogenic temperatures increase the confidence of constraining the atoms in their original positions. Furthermore, it restricts the possible redistributions of atoms by the electric field [78–80]. Exactly like FIM, the specimen is subjected to cryogenic temperatures to reduce the thermal agitation of the surface atoms. Atoms afterwards get ionized and in a controlled manner removed after applying electrical or laser pulses.

2.10.1 APT technique

Sharpened needles are transferred into an ultrahigh vacuum chamber (< 7.00 x 10^{-10} mbar), exposing them to a laser beam. In APT, an ultra-violet laser strikes the apex of the needle, while a base voltage from 0 to 12 KV is simultaneously applied. Atoms get ionized and evaporated in a controlled manner. Opposed to the apex, a position-sensitive delay line detector is used to register the positions of striking ions and measure the time of flight (ToF) of each ion. The stronghold of the APT is its ability to chemically identify those ions by time of flight spectrometry and to localize their positions by a position sensitive detector [15]. Time of flight is the time that each ion takes from the original location in its lattice to the impingement onto the detector. As the experiment is going on, a list of times-of flight and positions is populated with the data from each ion successively detected. The positions data parallel to the times set are thereafter used to build the tomographic reconstruction of the analyzed tip[18].

Similar to the FIM, APT's needle-shaped samples are mounted on a cryo stage, but -unlike FIM- there are neither imaging gas nor phosphorous screen. A base voltage V_{dc} -not sufficient to induce field evaporation of the atoms- is applied to the specimen. A key trigger of evaporation in the form of short additional voltage or ultrafast laser pulses is superimposed on the base voltage (see Figure 2.17). With the new micro-counter electrodes implementation, the specimen apex electric field increases and the measured volume can be extended to hundreds of nanometers [81]. Throughout the experiment, the radius of curvature increases and the electric field drops, which induces a drop in detection rate. The base voltage is automatically increased to counter-balance this drop and to maintain a constant detection rate.

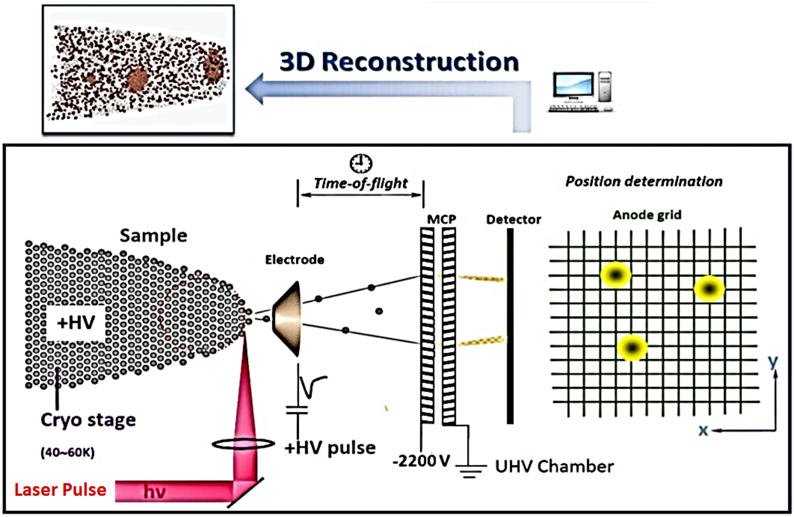
3D Reconstruction
Time-of-flight
Position determination
Sample
Electrode
MCP
Detector
Anode grid
+HV
Cryo stage
(40~60K)
+HV pulse
-2200 V
UHV Chamber
Laser Pulse
hv
y
x

Figure 2.17: Scheme of the atom probe tomography (APT). After [82].

A synchronized timer is adjusted between the detector and the applied pulse either electric or laser. The timer starts with the electrical or laser pulse and stops with arrival of an atom at the detector. This gives information about the time of flight (ToF) of each ion. By using the distance between the apex and the detector together with the flight length, elements can be identified. The basic concept of APT's time synchronization and time of flight (ToF) measurement is illustrated in Figure 2.18. The kinetic energy of the atoms is gained from the electrical potential $\boldsymbol{V}$. The equation of kinetic and potential energies yields:

$$E = \frac{1}{2} m v^2 = neV \tag{2.25}$$

where $\boldsymbol{E}$ is the kinetic energy, $\boldsymbol{m}$ is the mass of the object, $\boldsymbol{e}$ and $\boldsymbol{n}$ are the elementary charge and the charge state respectively, while $\boldsymbol{v}$ and $\boldsymbol{V}$ are the end velocity of the object and the applied electric potential, respectively.

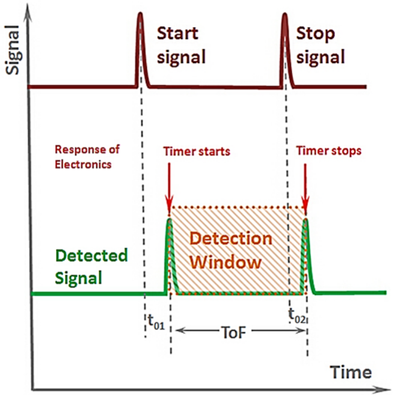
Signal
Start signal
Stop signal
Response of Electronics
Timer starts
Timer stops
Detected Signal
Detection Window
t_{01}
ToF
t_{02}
Time

Figure 2.18: Process diagram of the time of flight (ToF), electronics response as compared to the applied laser signal. After [82].

Mass per charge can be rewritten under the assumption of constant velocity along the trajectory as function of the flight length ***(L)*** -between tip and detector- and flight time ***(t)***,

$$\frac{m}{n} = 2eV \cdot (\frac{t}{L})^2 \tag{2.26}$$

As a result of the electronics response, a constant time deviation $\boldsymbol{t_0}$ -time of flight offset- is subtracted from the detected flight time ***t***. Moreover, the real flight length is modified according to the hitting position ***(x, y)*** on the detector.

$$\frac{m}{n} = 2eV \cdot \frac{t - t_0}{L^2 + X^2 + y^2} \tag{2.27}$$

After identification, also from the registered impact position, a 3D spatial reconstruction is built. Lastly, the three dimensional reconstruction is a mathematical method to recover the missing z-dimensional. This can be done by retrieving the z values along the tip axis from the temporal sequence of the events.

2.11 Volume Reconstruction

One of the outstanding features of the APT is the ability to obtain a 3-dimensional insight of the material on an atomic scale. The (x_D, y_D) coordinates of every ion hitting the detector are recorded during the measurement. Using this dataset in combination with the measured mass to charge ratios, a three dimensional view of the evaporated tip can be reconstructed. The reconstruction algorithm based on a point projection model used in this work, was initially proposed by Bas et al. [83]. A hemispherical cap along with straight ion trajectories are the essential assumptions [72]. Figure 2.19 represents the schematic geometry of the reconstruction.

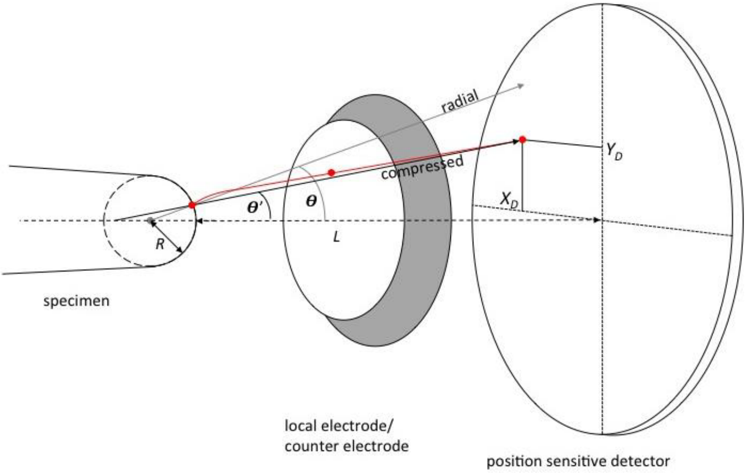

Figure 2.19: Schematic illustration of the reconstruction algorithm. L is the distance between the surface of the sample and the detector, R is the radius of the apex, (x_D, y_D) are the cartesian coordinates of the evaporated ion on the detector. θ and θ' are the angles of the detected ion in the radial and compressed modes respectively. After [84].

The x and y positions within the sample are reconstructed from the cartesian coordinates (x_D, y_D) of each detected ion. While the sequence of evaporated atoms represents the depth. Using straightforward geometry, the detection angle $\boldsymbol{\theta}'$, Figure 2.19, can be calculated from the relation:

$$\theta' = arctan\frac{\sqrt{x_D^2 + y_D^2}}{L} \tag{2.28}$$

where **L** is the distance between the detector and the evaporated tip.

Depending on the the assumption of the point projection, the incident angle θ' and the real crystallographic angle θ are correlated by the image compression factor k. Since the observed ion trajectory is deviating from the expected (radial) trajectory in a compressed manner, the angle θ has to be corrected.

$$\theta = \frac{1}{k} arctan\frac{\sqrt{x_D^2 + y_D^2}}{L} \tag{2.29}$$

So the originating coordinates x_i and y_i of an atom at the reconstructed tip surface can be represented by:

$$x_i = \frac{x_D}{\sqrt{x_D^2 + y_D^2}} R_i \cdot sin(\frac{\theta'}{k}) \tag{2.30}$$

$$y_i = \frac{y_D}{\sqrt{x_D^2 + y_D^2}} R_i \cdot sin(\frac{\theta'}{k}) \tag{2.31}$$

with the assumption of a hemispherical shape, the z-coordinate of the given atom is calculated by

$$z_i = R_i(1 - cos(\frac{\theta'}{k})) \tag{2.32}$$

The evaporated atoms are distributed along a spherical shell. In principle, this shell is filled up until all lattice sites are occupied and then moved down by one atomic distance. For every detected atom, the shell is consequently moved by a small infinitesimal distance dz_0 ($dN = 1$)

$$dz_0 = \frac{\Omega M^2}{pA_{detector}} dN \tag{2.33}$$

where $\boldsymbol{\Omega}$ is the atomic volume, $\boldsymbol{M}$ is the magnification, $\boldsymbol{p}$ is the detector efficiency, $\boldsymbol{A_{detector}}$ is the detector area, and $\boldsymbol{N}$ is the number of detected ions. Since the microchannel plates (MCP) in front of the detector have a limited open area, only a fraction typically 50 % of the evaporated atoms can be detected. Finally, z-coordinate for a single atom is the sum of Eq. 2.32 and Eq. 2.33.

$$z_{Total} = Z + Z_0 \tag{2.34}$$

2.12 Data Analysis

2.12.1 Concentration Analyses

Concentration of a given element, A, in atomic percent is estimated from the number of atoms of element A with respect to the total content in the sampled volume.

$$C_A = \frac{n_A}{n_T} \tag{2.35}$$

where $\boldsymbol{C_A}$ is the atomic fraction of element A, $\boldsymbol{n_A}$, and $\boldsymbol{n_T}$ are the number of atoms of element A and total number of atoms, respectively.

The standard error $\boldsymbol{\sigma}$ of different measurements can be calculated as [22]

$$\sigma = \sqrt{\frac{C_A(1 - C_A)}{n_T}} \tag{2.36}$$

2.12.2 Isoconcentration and Isodensity

Isoconcentration surface and isodensity surface are the most effective way to interpret atom probe data. A threshold concentration/density level of one or more elements are used to isolate blocks containing a specific range of composition or density for one or more selected elements. Interpretation through these blocks is used to create a 3D visualisation of iso-surfaces through the reconstruction. Adjacent blocks within the threshold level combine with each other to create an isosurface and appear as highlighted regions in the reconstruction. Different phases, grain boundaries and/or precipitates can be localized by defining appropriate of local atom fraction or density.

2.13 Voxelisation

In order to check the homogeneity of the sample and possible phase separation, a frequency distribution analysis is often applied. A binomial frequency distribution analysis has the ability to identify clustering or segregation processes [85, 86]. A region of interest from the reconstructed volume is partitioned into small sub-volumes (voxels). Voxel is a grid-based technique in either a cubic or a rectangular shape. The size of the voxel may be defined in one of two ways. The first is creating voxels with a constant volume, in which the number of atoms per voxel is varied. The second is creating voxels with a constant number of atoms, whereas the length along the three dimensions is varied. In both cases, a frequency distribution of voxels containing different numbers of atoms is obtained. Both ways are illustrated in Figure 2.20.

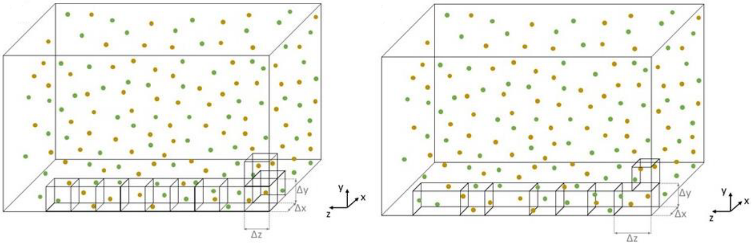

Figure 2.20: Left: Voxelisation with a constant volume. Right: Voxelisation with a constant number of atom per voxel. After [87].

The resulting histogram is compared to the binomial frequency distribution:

$$f_b(n) = N * \frac{n_b!}{n!(n_b - n)!} * {C_A}^n (1 - C_A)^{n_b - n} \tag{2.37}$$

where $\boldsymbol{f_b(n)}$ is the expected number of blocks containing $\boldsymbol{n}$ atoms of element $\boldsymbol{A}$. $\boldsymbol{N}$ is the total number of voxels, $\boldsymbol{n}$ is the number of the interested atom per voxel, $\boldsymbol{n_b}$ is the total number of all atoms per voxel and $\boldsymbol{C_A}$ is the average concentration of the selected atom [88, 89].

The measured frequency distributions are compared to the binomial distribution using the χ^2 analysis [90]. $\boldsymbol{\chi^2}$ statistics measures the departure from randomness.

$$\chi^2 = \sum_{n=0}^{n_b} \frac{(e(n) - f_b(n))^2}{f_b(n)} \tag{2.38}$$

where $\boldsymbol{e(n)}$ is the measured number of voxels containing n of the interesting atoms, and $\boldsymbol{f_b(n)}$ is the binomial distribution of voxels containing n of the interested atoms.

The value of χ^2 increases with the sample size [91]. Furthermore, the significance test is corrupted and increasingly likely to reject the randomly distributed atoms of element A throughout the material [86, 92, 93]. Large disparities are further exacerbated with a very large amount of data. In this case, analyses of χ^2 values cannot indeed compare the levels of clustering or segregation between specimens with different sample sizes. To normalise χ^2 on the sample size, the Pearson coefficient μ is implemented [91, 94]. Pearson coefficient test can be used to evaluate the statistical relevance of the observed deviation from the randomness [86, 92, 95]. μ values range between 0 and 1, where 0 indicates a random distribution and 1 indicates a complete compositional segregation [92, 96, 97]. $\boldsymbol{N}$ again is the total number of voxels.

$$\mu = \sqrt{\frac{\chi^2}{N + \chi^2}} \tag{2.39}$$

3 Experimental

3.1 Electropolishing

Electrochemical polishing is an efficient method for preparing the needle-shaped specimens required for atom probe tomography. By electropolishing, a tungsten (W) wire (diameter 0.075 mm) can be sharpened. The final product can be controlled to acquire the form of needle (apex ≤ 100 nm) or post (2 μm). When appropriate conditions are applied, the protruding parts of the surfaces are preferentially dissolved, which leads to a progressive smoothing. The W wire (anode) and a counter electrode are immersed in an aqueous base medium (sodium hydroxide, 2 mol L^{-1}) then connected to an AC source (see Figure 3.1). By applying a suitable voltage (3-10 V) to the anode, the etching process occurs at the interface between tungsten/electrolyte (the base medium).

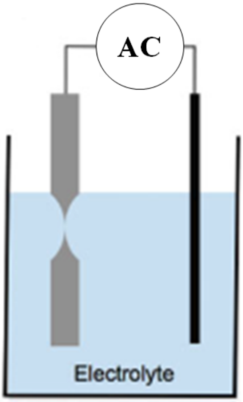

Figure 3.1: Schematic of the electropolishing setup.

At the anode, oxidation takes place and tungsten is converted into a tungsten anion [98]. The reaction mechanism was first analyzed by Kelsey [99]. Many researches were contributed afterwards to improve the etching equipment and the optimization of etching parameters [100–103].

3.2 Reactive Ion Beam Sputtering

Ion beam sputtering is a well known deposition technique in the physical vapor deposition family. Materials are evaporated by bombardment of an inert gas. The evaporated atoms are then condensed on substrates [104]. Figure 3.2 schematically illustrates the working principle of the method applied in this work. A target revolver with a maximum of four targets for in-situ switching of the target material is available. A fast sample exchange without breaking the vacuum is enabled by an airlock. With a base pressure (P_{base}) of down to 1.00 x 10^{-7} mbar and a working pressure 5.00 x 10^{-4} mbar, our sputtering chamber provides reasonable purity. In the gun, an electromagnetic field oscillates at 13.56 MHz in a 4.00 cm radio frequency (RF) copper coil of the ion source by Roth & Rau AG to ignite the argon plasma. Argon ions are accelerated towards the target using an electric field. High energy is transferred from the Ar ions to the atoms of the target material, and the atoms are thereby ejected from the target. These atoms are condensed on a substrate standing at a short distance from the target surface and almost parallel to it. The target is kept electrically neutral during the sputtering by switching between ion and electron beams. The thickness of the deposited film was monitored by a calibrated quartz crystal, located close to the substrates holder.

Targets were cleaned for 30 min by an ongoing bombardment of Ar ions, before starting the actual deposition. The Ar gun was operated with a power of 140 W and an acceleration voltage of 0.70 kV generating a beam current of 27.00 mA. The target was prepared from an uncoated LFP powder, (Novarials, Capacity: 150 mAh g^{-1} at 0.20 C, 2.70 - 3.20 V) cold pressed and sinter-annealed under ultrahigh vacuum (<10^{-7} mbar) at 500 °C for 24 h, resulting in a mechanically stable disk. Three different substrates in this thesis were used: W-needles of 100 nm diameter, W-posts of 2 μm cross section diameter

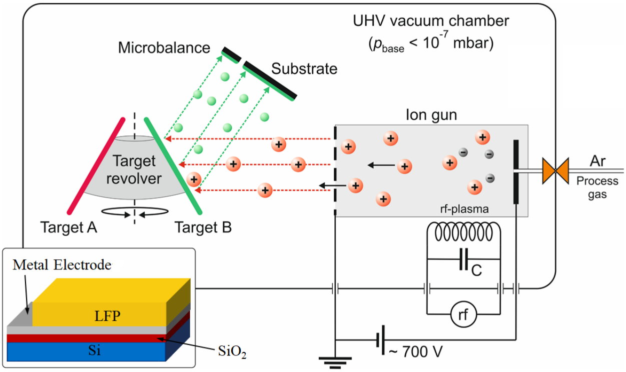
UHV vacuum chamber
(p_{base} < 10^{-7} mbar)
Microbalance
Substrate
Ion gun
Target
revolver
Target A
Target B
Ar
Process
gas
rf-plasma
C
rf
~ 700 V
Metal Electrode
LFP
Si
SiO_2

Figure 3.2: Scheme of the sputtering chamber and the flat thin film electrodes stack. After [105].

and flat SiO_2/Si substrates covered by a layer of Pt. As-sputtered amorphous $LiFePO_4$ thin films were crystallized through an additional annealing in an ultrahigh vacuum (<10^{-6} mbar) at 500 °C for 5 h [14].

3.3 Electrochemistry

The electrochemical properties of the produced thin films were checked using a three-electrode cell. In a three electrodes configuration, the sample works as the working electrode, and Li metal plates are counter and reference electrode [14]. The electrodes are dipped into a liquid electrolyte of ethylene carbonate and dimethyl carbonate (EC:DMC (1:1) containing 1 mol L^{-1} $LiClO_4$). In airtight sealed cells, electrodes were assembled in an argon-filled glove box. The electrochemical measurements were performed by a VSP-300 multi potentiostat (Bio-Logic SAS). The working (cathode) and counter (anode) electrodes exchange the Li ions between each other during the charging and discharging processes, while the reference electrode's compositions remain unchanged. So, the reference electrode provides a constant reference potential to monitor the varying working electrode potential.

3.3.1 Open Circuit Voltage (OCV)

Open circuit voltage (OCV) is an electrochemical measurement to determine the equilibrium potential between the working and the reference electrodes. OCV is the potential difference between the two electrodes when disconnected from any circuit. The measurement of its potential lasts at least 20 minutes until it reaches a plateau.

3.3.2 Cyclic Voltammetry (CV)

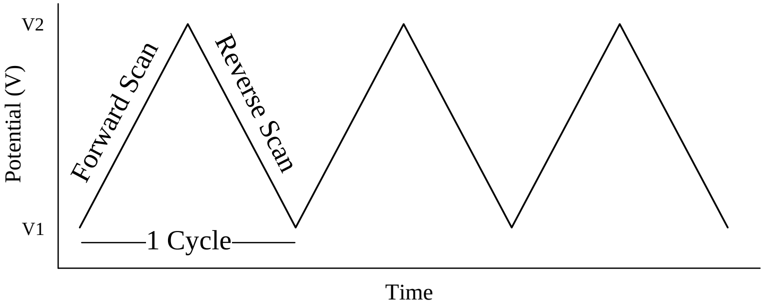

Figure 3.3: Potential waveform applied to the working electrode in the cyclic voltammetry experiment.

In cyclic voltammetry (CV), a set potential window is swept with a constant rate (v) and the corresponding current is recorded. Figure 3.3 illustrates the triangular wave form of the potential. The resultant cyclic voltammogram is the current response plotted versus the applied momentary potential.

The CV technique keeps in scanning the potential of a working electrode using a triangular potential waveform. The scan rate can be expressed as the change of the potential with respect to the time

$$v = \frac{dE}{dt} \tag{3.1}$$

where $\boldsymbol{v}$ is the scan rate. $\boldsymbol{E}$ is the potential and $\boldsymbol{t}$ is the time.

The redox potential and current of the working electrode can be acquired and the capacity can be calculated. The absolute capacity is calculated from the CV measurement using the following equation:

$$C_{abs} = \int I(t)dt \tag{3.2}$$

where $\boldsymbol{C_{abs}}$ is the absolute capacity. ***I(t)*** is the recorded current at a time $\boldsymbol{t}$.

Therefore, the specific capacity ***(C)*** can be extracted as:

$$C = \frac{C_{abs}}{A \cdot d \cdot \rho} \tag{3.3}$$

where $\boldsymbol{A}$ is the dipped area of the electrode into the electrolyte, $\boldsymbol{d}$ is its thickness, and $\boldsymbol{\rho}$ is the density of the electrode material.

3.3.3 Chronoamperometry (CA)

Chronoamperometry is a time-dependent technique, in which a constant potential is applied to the working electrode for a duration of time and the corresponding current is recorded (see Figure 3.4). In most cases, CA is applied to measure kinetic coefficients and/or to ensure a homogeneous distribution of Li throughout the whole layer.

3.4 Dual Beam Microscopy (SEM/FIB)

A Focused Ion Beam (FIB) is currently one of the most common and versatile nano tools used in materials science. A FIB dual beam microscope consists of a Ga ions column and an additional Scanning Electron Microscope (SEM), redefining the instrument to a flexible (dual-beam) platform. In principle, the instrument offers the opportunity of highly resolved scanning electron microscopy and nanomanipulation in one single instrument. Dual beam microscopes are mostly used for TEM lift-out lamella preparations, and it can also control the tips radii either in the way of flattening or sharping the tips.

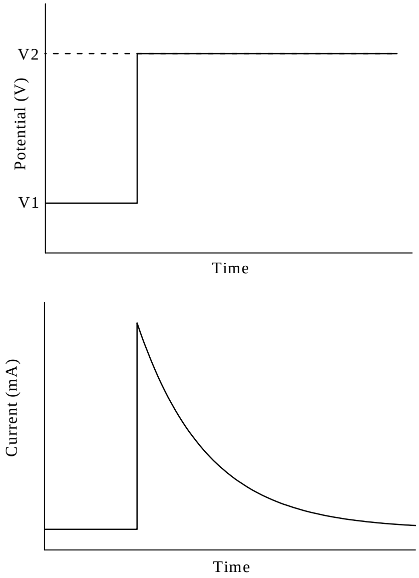

Figure 3.4: Potential (top) and corresponding current (bottom) waveforms in the chronoamperometry technique.

In this work, a FEI Scios Dual Beam Microscope equipped with an Easy Lift micromanipulator, and Pt Gas Injection System (GIS) was used. Therefore, it is adapted to image, remove, and deposit. Figure 3.5 schematically shows the geometric relationship of the stage, electrons and ions columns [106]. The two columns make an angle of 52° between each other, while the eucentric heights of both SEM and ion column are 7.00 mm and 19.00 mm, respectively.

A Ga needle is used as a liquid metal ion source (LMIS). Because of its low melting temperature, low vapor pressure, Ga ions are utilized to operate [76]. In presence of a strong electrical field on a sharp W needle, Ga ions are accelerated towards the sample. Using electromagnetic lenses, the Ga^+ beam is focused onto the sample. The ion beam has the ability to image by generating secondary electrons. Furthermore, Ga ions can erode material when using higher currents. Ion-activated deposition processes of metal films are

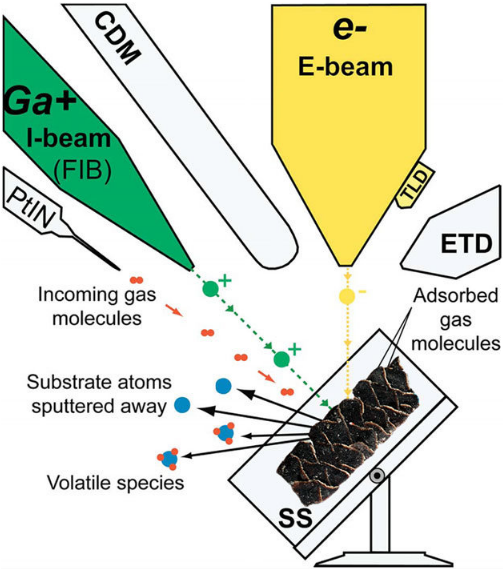
CDM
e-
E-beam
Ga+
I-beam
(FIB)
TLD
PtIN
ETD
Incoming gas molecules
Adsorbed gas molecules
Substrate atoms sputtered away
Volatile species
SS

Figure 3.5: Schematic diagram of the FIB-SEM device; PtIN, platinum injection needle; CDM, continuous dynode electron multiplier detector; ETD, Everhart-Thornley detector; SS, sample stage. After [106].

also enabled by a suitable organic-based platinum gas. A field emission gun (FEG) is used as an electron source. A high electric field is generated on the sharp needle shaped of W that causes the emission of electrons. Samples are precisely handled by a grounded stage, translation in three dimensions and rotation degrees of freedom around two axes.

3.4.1 Lift-out procedure

Figure 3.6 shows the lift-out procedures in FIB. At the beginning, a 700-800 nm thick Pt strip with dimensions 15 μm x 2 μm is deposited on top of the region of interest using the electron beam (see Figure 3.6 (1)). This step is to ensure the least damage from the ions impact. Subsequently, an additional

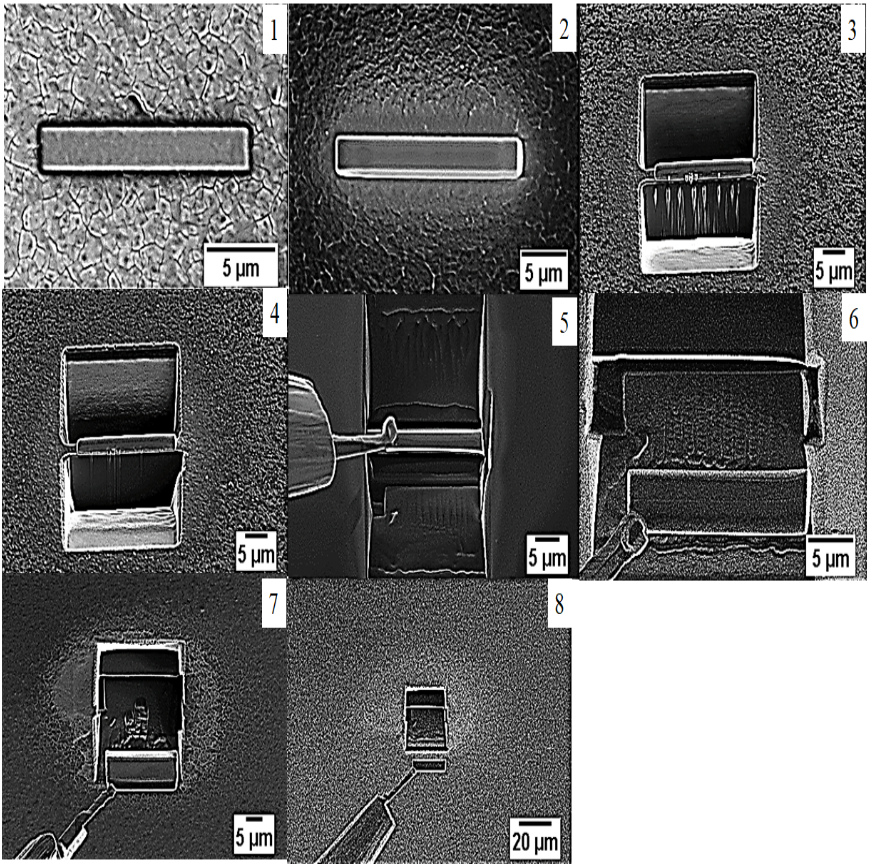

Figure 3.6: (1) E-beam deposited Pt layers using 5 kV. (2) Ion beam deposited Pt layer. (3, 4) Trenches milled into the specimen. 5) Micromanipulator attached to the lamella. (6, 7, 8) Lifting out the lamella.

thicker Pt layer with the same dimensions is deposited by using the ion beam (Figure 3.6 (2)). Trenches on both sides of the strip are cut off using a regular cross-section pattern. The trenches milling depth increases towards the Pt strip (see Figure 3.6 (3)). A lamella with a thickness of 15 μm between the two trenches is provided. A cleaning step is carried out using a cleaning cross section pattern (Figure 3.6 (4)). Before liberating the lamella from the substrate, an L-shaped undercut at stage tilt 7° is performed. At this point, the lamella is still attached to its substrate from one side. A micromanipulator is inserted, and gently placed on the cut-free side of the lamella. The micromanipulator is attached to the lamella by depositing a 1 μm thick Pt layer (Figure 3.6 (5)). The remaining connection of the lamella to the substrate is milled away. The lamella is now free from the substrate and subsequently attached to the micromanipulator (Figure 3.6 (6-8)). The lamella is finally attached either to a 2 μm W post for APT or to a Cu grid for TEM.

3.4.2 2 μm tungsten post

Figure 3.7 shows the sharpening steps of a tip in FIB. The lamella is mounted onto the 2 μm W post by Pt deposition (Figure 3.7 (1)). Annular milling is used to produce a sharp tip required for Atom Probe Tomography. The milling voltages/currents are sequentially reduced by reducing the tip diameter (Figure 3.7 (2-5)), until the final tip apex diameter around 100 nm is achieved (Figure 3.7 (6)). Sharpening of tips is done either for the lift-out lamella on W posts or for amorphous LFP directly deposited on W posts.

3.4.3 TEM Lamella

Figure 3.7 shows the thinning steps of a lamella in FIB. The lamella is mounted and glued onto a Cu grid by sputtering a 1 μm Pt layer (Figure 3.8 (1)). Then the lamella is thinned Figure 3.8 (2, 3). The Ga ions beam voltages/currents are operated in a descending manner with progress in thinning. Table 3.1 lists the applied voltages/currents of Ga ions at different lamella thicknesses.

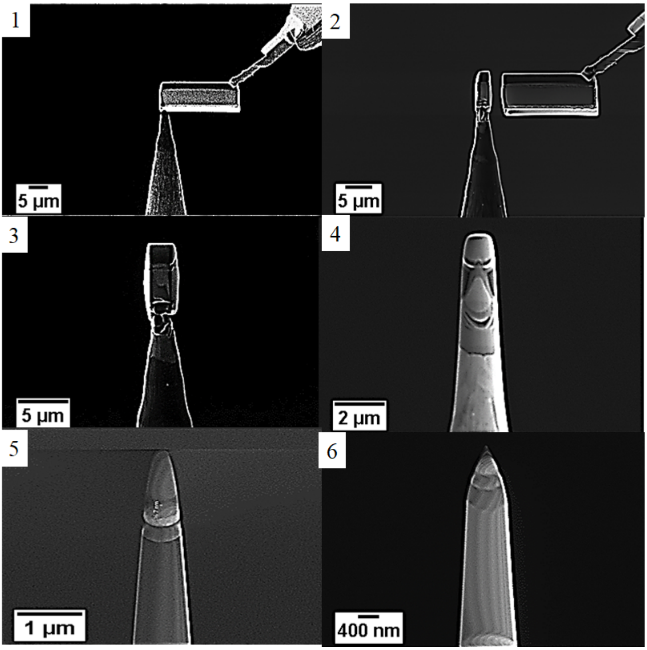
1
2
3
4
5
6
5 µm
5 µm
5 µm
2 µm
1 µm
400 nm

Figure 3.7: (1) Placing and gluing the lamella on the 2 μm W post. (2) Cutting the lamella. (3, 4, 5, and 6) Sharpening of the tip in a descending manner.

Table 3.1: TEM lamella thinning voltages/currents as compared to the thickness.

Ion beam current	Tilt angle/Milling side	Thickness after milling
30 KV, 1.00 nA	1.50/front -1.50/back	800 nm
30 KV, 0.50 nA	1.50/front -1.50/back	400 nm
30 KV, 0.10 nA	1.50/front -1.50/back	150 nm
30 KV, 50 PA	1.50/front -1.50/back	100 nm
Polishing at ± 3° or ± 5° tilting using cleaning cross at 2 KV, 27 pA and Z distance 10 nm		

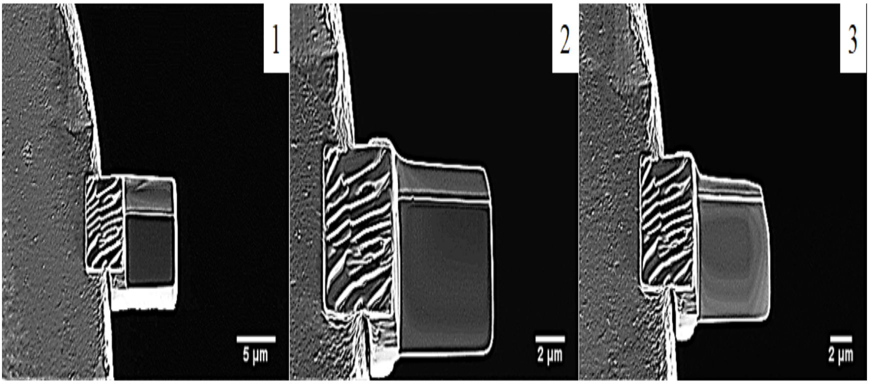

Figure 3.8: (1, 2, and 3) lamella thinning procedures.

4 Electrochemistry of LFP

4.1 Structural and morphological characterization

4.1.1 Structural characterization by XRD

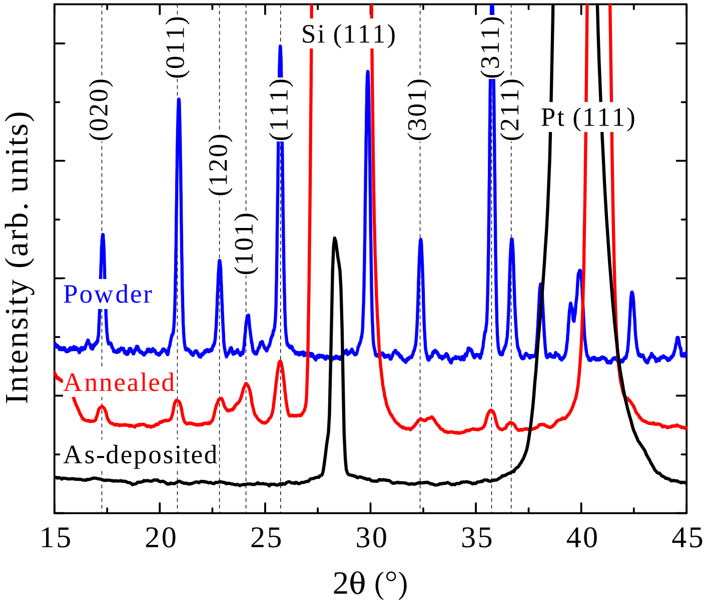

Figure 4.1: XRD spectra of the annealed LFP thin film as compared to the non-annealed LFP thin film and the LFP powder. All peaks are well clarified besides two main pronounced reflections of Pt and Si.

X-ray diffraction (XRD) was used to characterize the LFP thin films. It was carried out at room temperature on a Siemens BW/360/90/Rö diffractometer with a Cu-Kα radiation source. Figure 4.1 shows the x-ray diffractograms of the produced films in comparison to the LFP powder of the target (blue line). Amorphous (as deposited, black line) and annealed LFP thin films (red line) are shown. Crystalline thin film shows small reflections beside the strong reflections of the silicon substrate and the platinum current collector. Such low intensity peaks of LFP films have been frequently reported previously, however, with iron impurities [17, 107, 108]. By contrast the thin films produced here appear free of any iron peaks.

All diffraction peaks -excluding Si and Pt diffraction peaks- can be assigned to the LFP-related orthorhombic crystal system with a space group P_{nma} [109]. Unlike the reported impurities -$LiFeP_2O_7$, $Fe_4(P_2O_7)_3$, $Li_3Fe_2(PO_4)_3$, Fe_2O_3 [110–112], our own LFP thin films have a high phase purity with dissolved free iron. Bragg peaks can be indexed as (020), (011), (120), (101), (111), (301), (311) and (211) in (hkl) for the designated olivine type structure. The observed measured lattice parameters for the $LiFePO_4$ were (a = 10.27 Å, b = 6.03 Å, and c = 4.66 Å), which nicely fit to the standard lattice parameters values (a = 10.33 Å, b = 6.01 Å, and c = 4.69 Å). Additionally, the exact chemical composition of the LFP thin films was analyzed using the Inductively Coupled Plasma - Optical Emission Spectrometry (ICP-OES).

4.1.2 Compositional characterization by ICP-OES

The exact cation ratios in the LFP powder and the produced thin film were checked by ICP-OES using a Spectro Ciros CCD system from Spectro Analytical Instruments. By assuming the ideal stoichiometric content of oxygen, since it cannot be measured in both powder and thin film, the obtained values are presented in table 4.1. Analytical measurements show almost no deficiency, but a slight excess of lithium in the powder and the thin film.

Table 4.1: Chemical compositions of LFP powder and thin film by Inductively Coupled Plasma - Optical Emission Spectrometry (ICP-OES) after assuming the ideal content of O.

Intended Composition	Measured Composition
$\mathrm{Li}_{1.00}Fe_{1.00}P_{1.00}O_{4.00}$	Powder: $\mathrm{Li}_{1.22\pm0.09}Fe_{1.00\pm0.01}P_{1.03\pm0.02}O_{4.00\pm0.00}$
	Thin film: $\mathrm{Li}_{1.12\pm0.06}Fe_{1.00\pm0.01}P_{0.93\pm0.03}O_{4.00\pm0.00}$

4.1.3 Morphological characterization by TEM

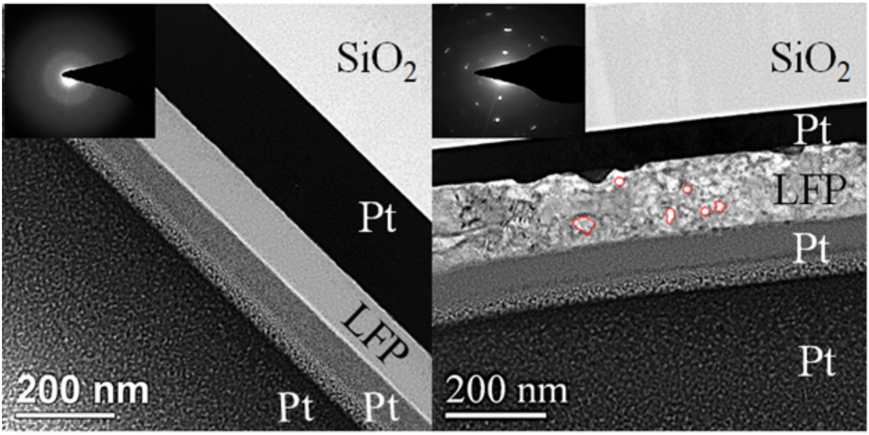

Figure 4.2: Bright field TEM images of the produced layers stack with the respective diffraction pattern from the LFP. LFP/Pt layers are stacked between two Pt protective coatings from the FIB and the SiO_2 substrate. Left: LFP_{100nm}/Pt_{150nm} in as-deposited state and its respective diffraction pattern confirm the amorphous structure. Right: LFP_{150nm}/Pt_{100nm} layers after an additional annealing in an ultrahigh vacuum ($<10^{-6}$ mbar) for 5 h at 500 °C. Crystalline LFP layer with some highlighted grains in red colour is shown.

To get more structural and morphological information about the films, cross section Transmission Electron Microscopy (TEM) micrographs were captured to distinguish between amorphous and crystalline features, as shown in Figure 4.2. The cross sections lamellae were prepared by the ion beam milling using the Focused Ion Beam (FIB), see section 3.4. The interface quality between layers, in addition to their thicknesses, can be clearly observed. LFP films present dense layers, well adherent to the substrate, exhibiting almost a uniform thickness and smooth surfaces. The as-deposited sample shows a clear amorphous structure, whereas the annealed sample displays a crystalline structure. The bright spherical regions represent crystalline grains, a few of them emphasized by red circles in Figure 4.2 (right). It is obviously clear from the x-ray diffraction, the compositional characterization by ICP-OES, and TEM that the desired structure and morphology for active LFP are well formed.

4.2 Electrochemical characterization

4.2.1 Rate capability

Microstructural analyses using XRD and TEM demonstrate that the annealed layers represent the intended lattice structure, but the functionality of layers as battery electrodes is yet to be probed. To characterize their electrochemical behavior, LFP thin films were charged/discharged using a VSP-300 potentiostat (Bio-Logic Science Instruments SAS). In a custom-built gas tight cells filled with argon, cyclic voltammetry (CV) was executed. As shown in Appendix Figure A.1, the amorphous sample -as a result of its poor crystallinity- exhibits no-electrochemical activity. Similar observations have also been reported previously [17]. The rate capability of lithium batteries critically depends on the reversible insertion and extraction of Li ions in the crystal structure of the electrode materials [49], therefore a wide range of scan rates from 400 to 0.004 mV s^{-1} was examined. Figures 4.3 (a-c) show the plots of the measured dis-/charging currents versus the applied voltage at different scan rates for a 200 nm thick film. The layers were cycled in a potential window between 3.20 V and 3.80 V. All films are first cycled at 1.00 mV s^{-1} for 10 cycles to avoid any possible influence of irreversible reactions [113]. Subsequently, the scanning series started from the lowest rate 0.004 mV s^{-1}, followed by several order of magnitudes faster scanning rates. Each scan rate was performed for three cycles. This standard protocol gives the chance to determine the real capacity and to indicate the cyclic stability. For reason of clarity in the figure, the series of CV measurements is split into three regimes.

Two defined current peaks are observed, averaged at around 3.45 V -see Figure 4.3, clearly indicate the Li intercalation and deintercalation reactions [114]. These two peaks, reduction and oxidation peaks, contribute to the gain and loss of electrons during the insertion and extraction of lithium from the

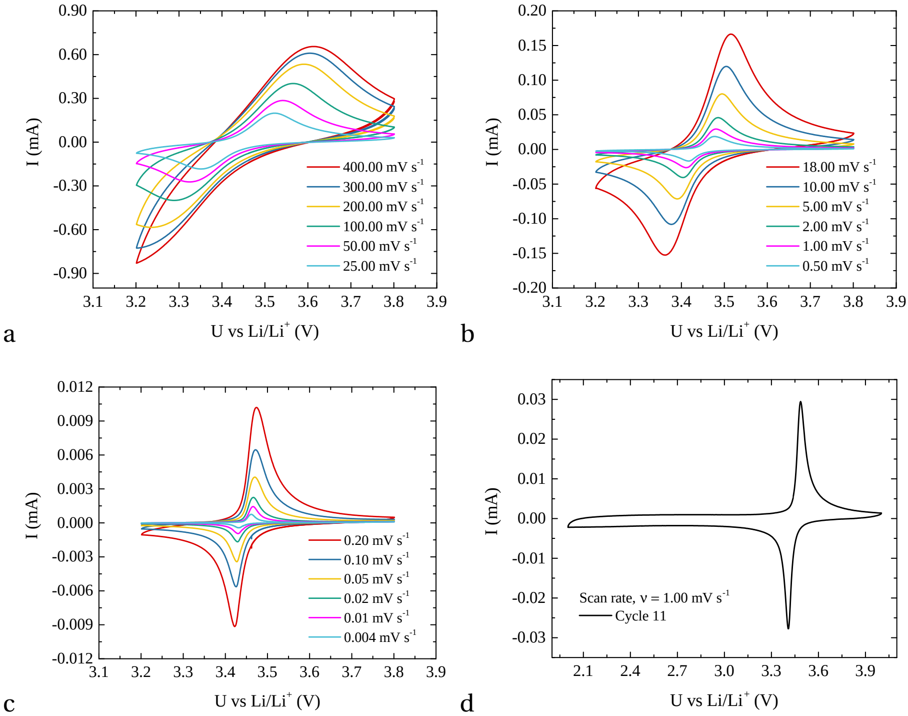

Figure 4.3: CV data of a 200 nm thin LFP film at different scanning rates. For the sake of clarity, presentation was split into three regimes of decreasing scanning rate (a, b, c). Additional CVs for another thickness can be found in Appendix (Figure A.2). (d) LFP film measured in the voltage window 2.00-4.00 V, film thickness is 150 nm.

$LiFePO_4$ crystal cell. Aside from this, no further peaks are detected, which confirms that no foreign phases overlap with the moving lithium between the electrodes. For more reliable overview, CV was also checked in the voltage window between 2.00 to 4.00 V (see Figure 4.3 (d)). The layer along the whole voltage range after some cycles does not show any foreign peaks indicating the absence of Li trappers like $Li_3Fe_2(PO_4)_3$ [15].

The measured currents systematically increase on the scanning rate, which is expected and is in line with previously published reports [14, 114]. At low scan rates, LFP shows a near equilibrium deintercalation and intercalation processes. With increasing the scanning rates, the deintercalation and intercalation peaks start to shift, indicating an increased overpotential to drive the ion transport [113]. Furthermore, at fast scan rates, the peaks become less defined and broader. Moreover, the capacity particularly during the lithiation is accumulated by the space charge zones, which is seen as a vertical translation at the edges of the potential window, while their overall linear slope almost indicates an ohmic loss [113].

4.2.2 Cycle stability

To document the cyclability (cycling stability) of the produced layers, a 100 nm thin LFP film was successfully cycled over 7000 cycles at a constant scan rate 2.00 mV s^{-1} (see Figure 4.4). By comparing the first and the last cycle, irreversible degradation appears negligible. In conjunction with increasing the cycle numbers, the intensities of the redox peaks show only a slight decrease. The dis-/charge capacities together with their retention are plotted in Figure 4.5.

The volumetric capacity is calculated by integrating the corresponding CV area for a single complete cycle with respect to voltage and divided by twice of the scan rate $\boldsymbol{v}$.

$$K = \frac{1}{2v} \cdot \int_{u_1}^{u_2} J(U)\,du \tag{4.1}$$

where $\boldsymbol{K}$ is the capacity, $\boldsymbol{J}$ is the current density and $\boldsymbol{U}$ is the voltage.

The initial capacity at 6 C amounts to 46 mAh g^{-1} and so the measured capacity of the thin film is lower than the theoretical expectation for LFP 170 mAh g^{-1}. Such capacity deficit is expected for thin films, which may be due to an excessive reliance of Li mobility on the Li concentration that results in formation of isolated Li pockets. Hence Li cannot be easily moved in or out

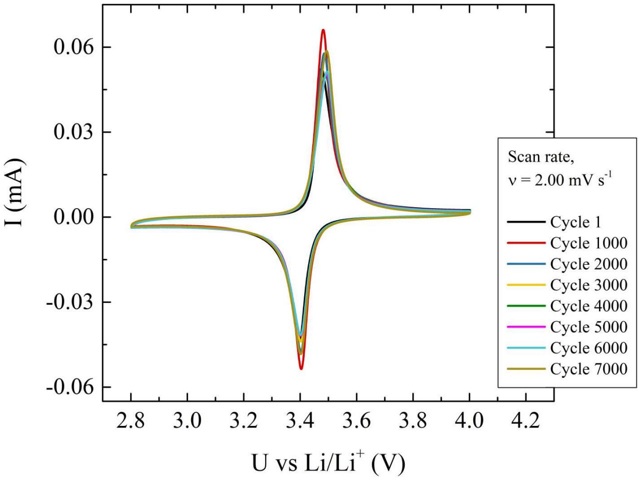

Figure 4.4: CV data for 100 nm thick at a constant scan rate 2.00 mV s^{-1} (6 C). The layer shows a stable dis-/charging cycling for 7000 cycles.

the cathode materials during the dis-/charging. In case of the uncoated LFP powder, 110 mAh g^{-1} (at 0.10 C) and 90 mAh g^{-1} (at 0.5 C) were reported in the literature [115]. By contrast, the capacity retention in this work is superior and even better than the reported. Capacity retention of 92 % after 7000 cycles is achieved, inset Figure 4.5. This points out stable Li kinetics inside the layer. Conversely, such quality has never before been achieved, neither the cyclic stability nor coulombic efficiency. The remarkable cycling reversibility of the produced LFP thin films proves an excellent electrochemical performance in consequence with no cracks [116]. Furthermore, LFP material in the form of thin films shows less stress and better stress relation. Finally, LFP thin films exhibit no loss from the solid electrolyte interphase (SEI). Thus, the produced layers are suitable for prolonged detail studies of LFP in a 3D view.

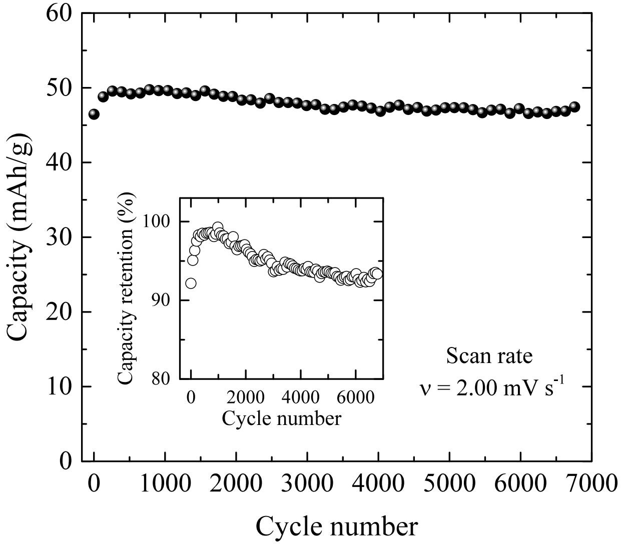

Figure 4.5: The calculated capacities for a 100 nm LFP thick film and their retention after 7000 dis-/charge cycles.

4.2.3 Li kinetics

Because of the systematical variations, peak currents and their relative potential shifts were used to quantify the kinetic behavior of the transport [113]. Current densities and potential shifts were calculated from the CV curves. For more details about the CV measurements, check section 4.2.1. Li kinetics were investigated under the variation of the scanning rate for over five orders of magnitude for different thicknesses. Swapping rates ranged from 0.004 to 400 mV s^{-1} for thicknesses from 25 to 250 nm.

Aoki et al. [117] suggested that the peak current density can be approximated as:

$$J_p = 0.446\, e \cdot C_{max} \cdot \frac{D}{h} \sqrt{\tilde{v}}\, tanh(0.56\sqrt{\tilde{v}} + 0.05\,\tilde{v}) \tag{4.2}$$

where $\boldsymbol{j_p}$ is the peak current density in (A m^{-2}), $\boldsymbol{e}$ is the electron charge in (coulombs), $\boldsymbol{C_{max}}$ is the bulk concentration of lithium (mol m^{-3}), $\boldsymbol{D}$ is the diffusion coefficient (m^2 s^{-1}), and $\boldsymbol{h}$ is the maximum diffusion depth, when defining a scaled scanning rate:

$$\tilde{v} = \frac{e\,h^2}{DK_B T}\,v \tag{4.3}$$

$\boldsymbol{K_B}$, $\boldsymbol{T}$ are the Boltzman constant (m^2 kg s^{-2} K^{-1}) and temperature (K), and $\boldsymbol{v}$ is the experimental scan rate (V s^{-1}).

Equation 4.2 can be simplified by two extreme cases: (i) small scan rate, fast diffusion or very thin layers:

$$J_p = 0.25\,e^2 \cdot C_{max}\,\frac{d}{K_B T} \cdot v \tag{4.4}$$

where the new symbol $\boldsymbol{d}$ is the film thickness in (m), which likely corresponds to the diffusion depth.

And (ii) for fast scan rate, slow diffusion, and thick films as:

$$J_p = 0.446\,e \cdot C_{max}\sqrt{\frac{eD}{K_B T}} \cdot \sqrt{v} \tag{4.5}$$

which is the same result given by Randles et al. [118] and is expected to become independent of the film thickness.

The double logarithmic plots, Figures 4.6 (a, b), for the deintercalation and intercalation peaks indicate different kinetic regimes. A close to linear dependence for the peak current density on the rate is observed at slow scanning. This is followed by the Randles-Sevick (R.-S.) regime (scan rate with an exponent close to 0.5) at fast rates. According to Randles-Sevick relation [118], the maximum current increases in proportion to the square root of the scan rate, whereas the slope in the respective plot demonstrates a direct measure of the diffusion coefficient. This is more clearly shown in Figures 4.7 (a, b). In these figures, a parabolic dependence of the current densities at fast scanning is demonstrated.

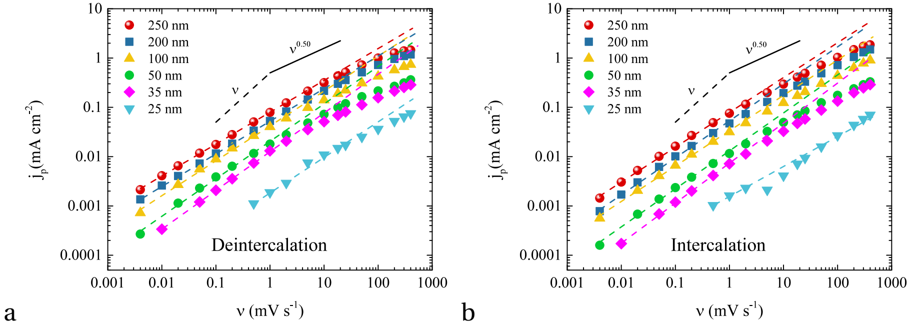

Figure 4.6: Randles-Sevcik (R.-S.) plots: (a, b) Double logarithmic plots of current density (j_p) versus the scan rate (ν) for the deintercalation and intercalation peaks, respectively. Linear regressions were plotted in dashed lines. As a reference for comparison with the experimental data, two black lines with exponents 0.50 (solid line) and 1.00 (dashed line) were drawn.

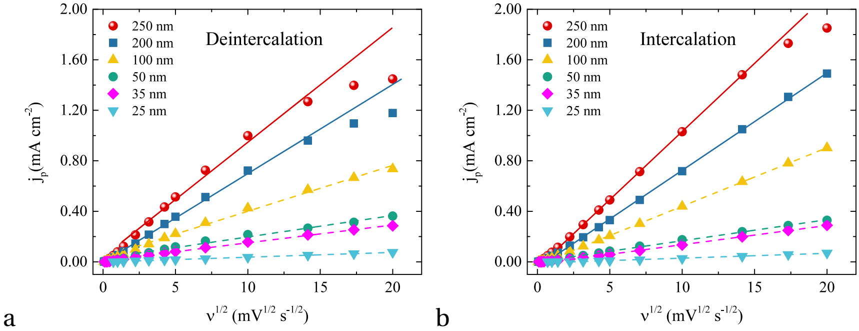

Figure 4.7: Randles-Sevcik (R.-S.) plots: (a, b) Current density (j_p) versus square root of the scan rate ($\nu^{1/2}$) for the deintercalation and intercalation peaks, respectively. Linear regressions were plotted in dashed lines, whereas two solid linear regressions were drawn in red and blue for the thickest films 250 and 200 nm, respectively.

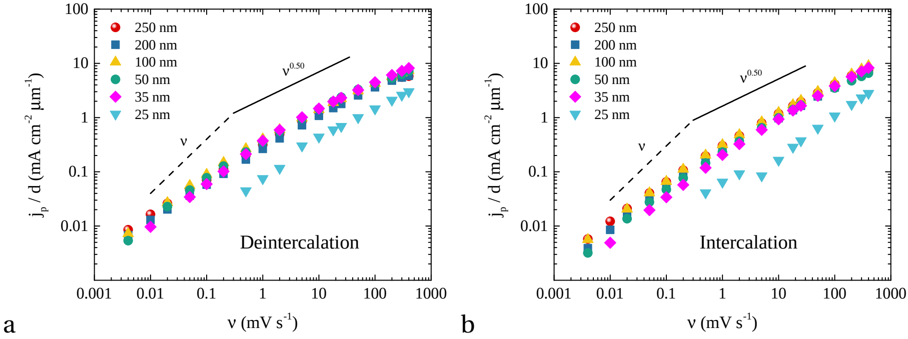

Figure 4.8: (a, b) Peak currents normalized to films thicknesses as a function of the scan rate for the deintercalation and intercalation peaks, respectively. As a reference for comparison with the experimental data, two black lines with exponents 0.50 (solid line) and 1.00 (dashed line) were drawn.

In remarkable contrast to the expected linear-parabolic R.S. behavior at fast scanning rates, however, the currents also surprisingly increase in proportion to the layer thickness (see Figures 4.6 and 4.7). Noteworthy, normalizing by the layer thicknesses -Figures 4.8 (a, b), peak fluxes are alike except for the thinnest layer (25 nm), because of formation of an inactive reaction layer [14]. Thus, a clear proportionality of the peak current versus the layer thickness is shown. Theoretically, the R.S. kinetics of phase separating materials should be independent of the layer thickness, since the peak current appears way before the phase boundary reaches the collector electrode. Only in the linear regime, a thickness dependence maybe accepted as the capacity per film area increases with increasing the layer thickness. However, in the R.S. regime, a significant dependence on the layer thickness is hardly understood. In consequence, the calculated diffusion coefficients - from Eq. 4.5- depend on the layer width, see Table 4.2. Conceptually, a diffusion coefficient is a characteristic property of matter and should be independent of the film thickness, if the grain structure remains the same for different thicknesses. However, from Table 4.2, it is at least suggested that the effective diffusivity is influenced by the layer thickness [113].

Table 4.2: Diffusion Coefficients (D) as a function of the layer thickness (d).

d (nm)	$\mathbf{D_{De}}$ **(cm^2 s^{-1})**	$\mathbf{D_{Int}}$ **(cm^2 s^{-1})**	$\mathbf{D_{De}/d}$ **(cm^2 s^{-1} nm^{-1})**	$\mathbf{D_{Int}/d}$ **(cm^2 s^{-1} nm^{-1})**
250	2.21×10^{-12}	4.03×10^{-12}	8.85×10^{-15}	1.61×10^{-14}
200	1.52×10^{-12}	2.56×10^{-12}	7.62×10^{-15}	1.28×10^{-14}
100	5.59×10^{-13}	9.13×10^{-13}	5.59×10^{-15}	9.13×10^{-15}
50	1.22×10^{-13}	1.18×10^{-13}	2.45×10^{-15}	2.36×10^{-15}
35	8.47×10^{-14}	9.87×10^{-14}	2.42×10^{-15}	2.82×10^{-15}
25	6.19×10^{-15}	6.29×10^{-15}	2.48×10^{-16}	2.52×10^{-16}

A point to note, the linear regime is independent of the diffusion coefficient due to the quasi-equilibrium loading conditions, meaning the insertion is controlled by the variation of the potential and not by the diffusion of ions. Only, at fast scanning, the lithium transport is controlling the insertion process and hence the flux can be affected by the diffusion coefficient. The parabolic regimes in Figures 4.7 (a, b) are very well confirmed, see Eq. 4.5. Only further deviation for the thickest films (250 and 200 nm) is seen at ultra-fast scan rates. To clarify this deviation, two solid regression lines considering only the scan rates $\leq$ 200 mv s^{-1} ($\sqrt{\nu} \leq 14.14$ mv$^{1/2}$ s$^{-1/2}$) are drawn in Figures 4.7 (a, b). This deviation is due to the fact that the strong overpotential shifts the hypothetical current maximum out of the scanned voltage window.

The slope of the double logarithmic graphs indicates the exponent of ν in equation 4.4. It is observed that the exponent increases towards 1.00 with decreasing the layer width, as an equilibrium is more easily established for small film thickness (except for the thinnest layer (25 nm)), as it is shown in Figure 4.9 (a). As per Wunde et al. [114], an exponent close to 1.00 would indicate a homogeneous distribution of Li-ions through the thin films. In a two-phase reaction material in thin film geometry, where the lithium is entering from the top surface, the only possibility would be the homogeneous distribution of nucleation sites throughout the whole film. On the other hand, the diffusivity can be calculated from the ($j_p/\nu^{1/2}$) ratios (Figure 4.9 (b)), for each thickness which represents the apparent diffusion coefficient, as shown

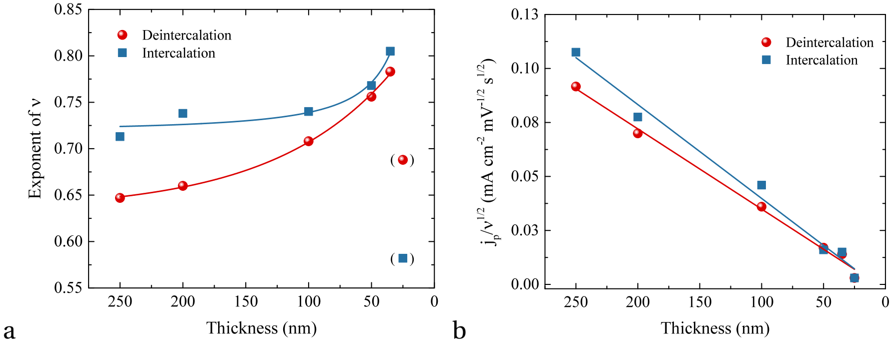

Figure 4.9: (a) Evolution of the kinetic exponent versus the layer thickness. Such exponents were calculated from the regression lines of Figures 4.6 (a, b) for low scan rates. (b) Calculated slopes ($j_p/\nu^{1/2}$) versus the layer thickness. They were calculated from the regression lines of Figures 4.7 (a, b) for fast scan rates.

in table 4.2. The apparent diffusion coefficient is the observed diffusivity that may have contribution from the grain boundaries.

Significant deviation of the thinnest layer (25nm) is ascribed to its vicinity to the zero capacity layer. Zero capacity layer is identified in previous reports by an inactive layer on the top of the measured film [14, 35, 51]. Indeed, Figure 4.10 outlines a linear regression line through the capacity at different thicknesses that does not cross through the origin, but at around 18 nm. This offset practically represents the zero capacity or in other words an inactive reaction layer [14]. Therefore, the current, exponent evolution and the apparent diffusion coefficient cannot be reliably interpreted in the case of the thinnest layer (25 nm).

The voltages at which the redox peaks positions appeared versus the scan rate are shown in Figure 4.11 (a). Each line represents the peak potential positions for a specific layer thickness at different scan rate. The top branch displays the potential positions of the deintercalation peaks, while the bottom is for the intercalation peaks. All curves start close to the equilibrium at low scan

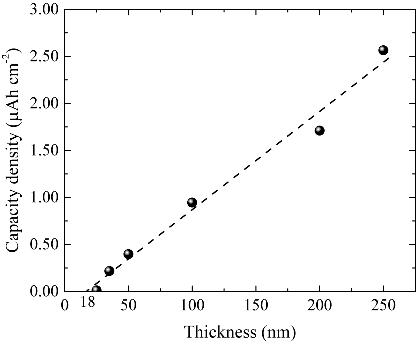

Figure 4.10: Linear relationship between the capacity per unit area and the layer thickness at ν = 1.00 mV s^{-1}. The intersection of the regression dashed line and the x-axis is determined to be around 18 nm.

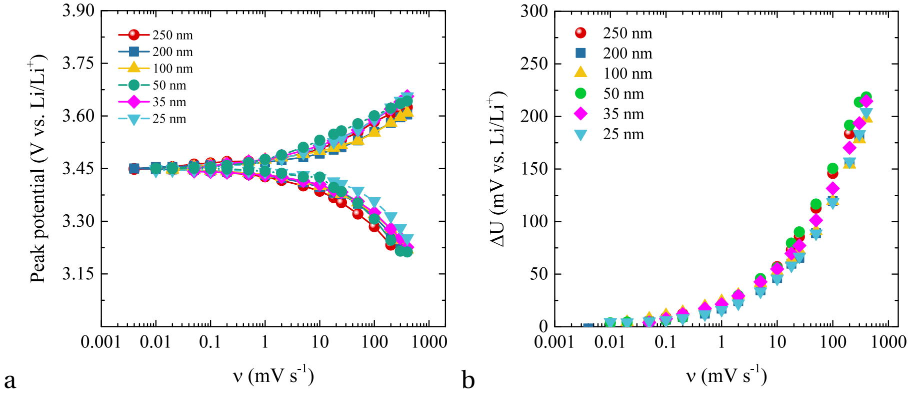

Figure 4.11: (a) Changes of the anodic and cathodic peak potentials for different thicknesses as a function of the scan rate (ν). (b) Overpotentials for different layer widths at different scan rates.

rates, until they commence together to diverge at 1.00 mV s^{-1}. The overpotential is the potential required to drive the transport. It may be conveniently quantified as the half of the difference between deintercalation and intercalation potential peaks. As a consequence of increasing the required driving force to transfer Li ions, overpotential must obviously be scan-rate dependent. On the other hand, opposite of the peak current density, no systematic dependence of the overpotential on the layer thickness is noticed (see Figure 4.11 (b)), although the flux increases with the layer thickness. From the Butler-volmer equation, Eq. 4.6, the current density is correlated to the overpotential, which means the atomic fluxes should be proportional to the driving force, which interestingly isn't the case.

$$f_{BV}(\Delta U) = j = j_0 \cdot \left\{ exp\left[\frac{\alpha_a z F \Delta U}{RT}\right] - exp\left[-\frac{\alpha_c z F \Delta U}{RT}\right]\right\} \tag{4.6}$$

where $\boldsymbol{j}$ is the electrode current density in (A m^{-2}), $\boldsymbol{J_0}$ is the equilibrium exchange current density in (A m^{-2}), $\boldsymbol{\alpha_a}$, $\boldsymbol{\alpha_c}$ anodic and cathodic charge transfer coefficient (dimensionless), respectively. z is the number of electrons involved in the electrode reaction. ***F, R, T*** have their normal meanings Faraday's constant in (coulombs mol^{-1}), the universal gas constant in (Kg m^2 K^{-1} mol^{-1} s^{-2}), and the absolute temperature (K), respectively. $\boldsymbol{\Delta U}$ is the overpotential (V).

Additionally, considering the electrical resistance part, Butler-Volmer's equation might be modified to

$$J_P = f_{BV}(\Delta U) + \frac{\Delta U}{AR'} \tag{4.7}$$

where $\boldsymbol{J_p}$ is the maximum peak current, $\boldsymbol{f_{BV}(\Delta U)}$ is the Butler-volmer's equation, $\boldsymbol{\Delta U}$ is the overpotential, ***A*** is electrode area, and ***R'*** is the electrical resistance of the setup.

Eq. 4.7 is fitted to the measured current density as shown in Figure 4.12 (a). The anodic charge transfer coefficient (α_a) was found to be 0.42, while the cathodic charge transfer coefficient (α_c = 1 - α_a) was 0.58.

Less electrical driving force is required to force the same current in thicker films as clearly demonstrated in Figures 4.12 (a, b). It is an appealing consid-

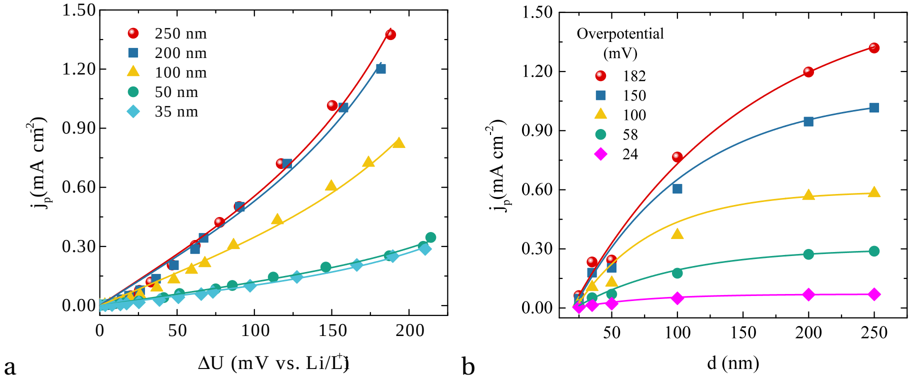

Figure 4.12: (a) Peak current density (j_p) versus the overpotentials (ΔU) for different thicknesses. (b) Peak current density (j_p) versus the layer thickness (d) at different overpotentials.

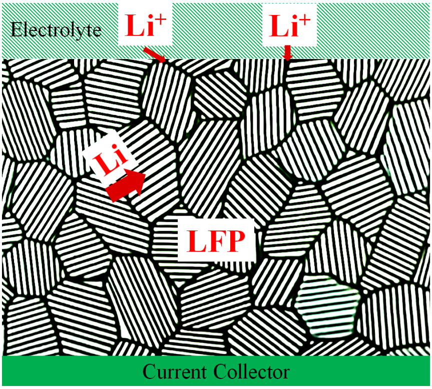
Electrolyte
Li$^+$
Li$^+$
Li
LFP
Current Collector

Figure 4.13: Schematic diagram represents the Li transport. Thin arrows: ionic transport through the LFP grains, thick arrows: intercalation in LFP.

eration that the thicker the films are, the more grain boundary areas they contain. This indicates that the grain boundaries may represent an electroactive interface at which the overpotential appears. And hence, the grain boundaries work as short circuits (fast conduction paths) for faster Li ions diffusion [114, 119]. It means that the intercalation would appear from the grain boundaries into the grain interior. Thus, the total current is controlled by the total grain boundary area within the film rather than the thin film surface. In this way, the peak current is influenced by the total grain boundary (GB) area. Possible Li transports in LFP thin films are represented in Figure 4.13. Thus, the current density can be simplified in terms of the grain boundary area and the overpotential as

$$J_P \propto A_{GB} \cdot f_{BV}(\Delta U) \tag{4.8}$$

where $\boldsymbol{J_P}$ is the maximum peak current density, $\boldsymbol{A_{GB}}$ is the grain boundary area, and $\boldsymbol{\Delta U}$ is the overpotential.

Figures 4.14 (a-d) represent the cross-section TEM micrographs of the produced LFP layers for selected thicknesses 250 nm and 100 nm. Rather equisized grains were found, average grain sizes 56 ± 3 nm with standard deviation 38 nm for 250 nm thick and 57 ± 3 nm with standard deviation 25 nm for 100 nm thick. Grain boundary area in this work comes in agreement with the previously observed size -50 nm- reported by Wunde et al. [114]. The microstructure begins from an amorphous state during the annealing treatment, which discards any obvious correlation to the layer thickness [114]. Contrary to the columnar grain structure Li materials like $LiMn_2O_4$ and $LiCoO_2$, grain size of $LiFePO_4$ is independent of the layer thickness. Therefore, the unexplained peak current dependence on the layer thickness is then naturally interpreted in terms of increasing the grain boundary (GB) area. Again, grain boundaries work as short circuits for faster Li ions diffusion [114, 119]. Consequently, different peak current densities at the same overpotentials are observed Figures 4.12 (a, b).

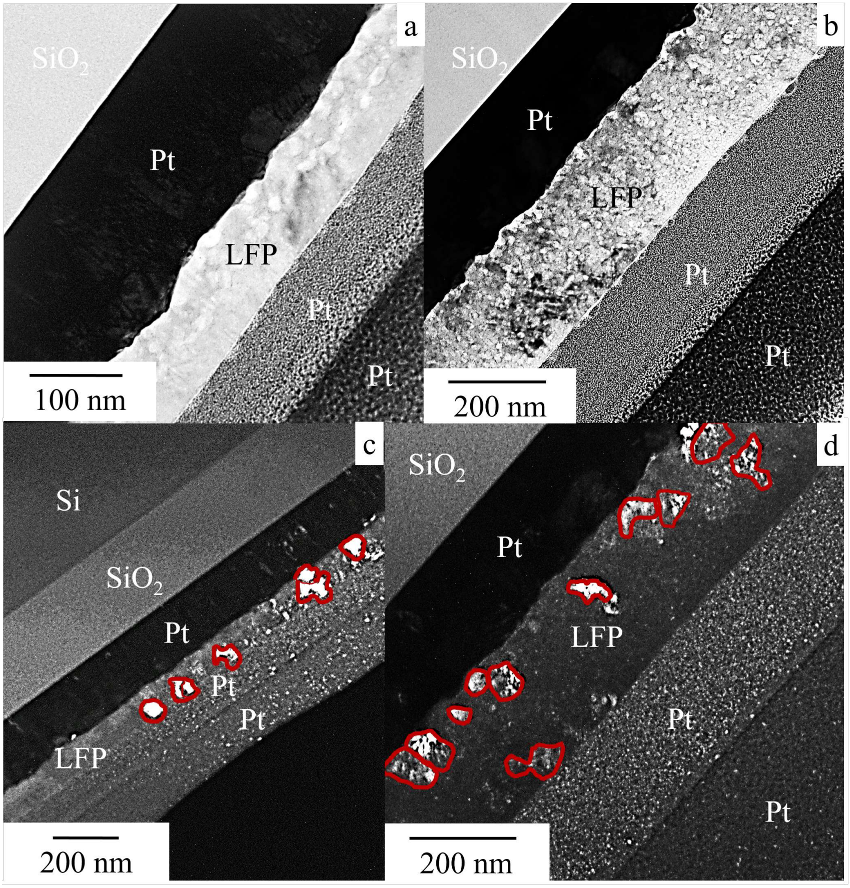
a
SiO2
Pt
LFP
Pt
Pt
100 nm
b
SiO2
Pt
LFP
Pt
Pt
200 nm
c
Si
SiO2
Pt
Pt
Pt
LFP
200 nm
d
SiO2
Pt
LFP
Pt
Pt
200 nm

Figure 4.14: (a, b) Bright and (c, d) dark field TEM images of LFP thin films for thickness 250 nm and 100 nm, respectively. LFP layers locate directly next to the highlighted Pt electrode collector.

5 3D Analyses of Amorphous and Crystalline LFP

Cathode performance has been observed to be affected by the transition metal cation/Li distributions. Intercalation would appear from the grain boundaries (GB) into the grain interior. Besides, GB work as fast conduction paths. Now, it is attempted to check them by laser-assisted atom probe tomography (APT). Three-dimensional chemical maps of lithium with atomic spatial resolution were provided. The results were correlated to the distributions of the transition metal cation (Fe), phosphorous, and oxygen.

5.1 Evaporation field of Lithium Iron Phosphate (LFP)

Great efforts have been made to reveal the microstructural and chemical properties of LFP on a three dimensional atomic (3D) level. 3D analysis by APT requires the determination of the evaporation field of the measured material. In most cases, evaporation fields were resolved by using calibration layers. Such layers are sputtered on the material of interest before the APT measurements. These layers play an important role not only to calibrate the evaporation fields but also to protect the materials of interest. Unfortunately, this strategy has failed with LFP. The unsuccessful behavior of such layers is attributed to the strong evaporation field differences between Li/LFP and the layers themselves. It is worth noting that many different layers were tested, e.g. Al, Ni, Co, and Pt. Appendix Figures A.3 and A.4 display an example of such trials. It was also considered choosing a layer with an evaporation field located close to the Li's evaporation field ($14\ \mathrm{V\,nm^{-1}}$) and/or around the expected value of LFP ($30\ \mathrm{V\,nm^{-1}}$).

5.1.1 LFP/W bi-layers

A tungsten (W) needle with a curvature radius <100 nm is produced by the standard electropolishing method [120] (see Figure 5.1 (a)). Prior to LFP deposition, the needles are developed to 10 KV by the Field Ion Microscope (FIM) in order to get a smooth, well rounded needle apex. This geometry of the tip is crucial for the APT measurements. Figure 5.1 (b) recognizes a homogeneous distribution of the tungsten poles. The characteristic crystallographic features of the shown tungsten surface prove the absence of any distortions or deformations.

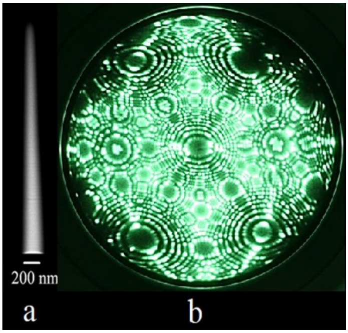

Figure 5.1: (a) SEM image of a tungsten needle. (b) Typical field ion micrograph of a pure W observed along the (110) direction.

A 40 nm of amorphous LFP layer was deposited upon a smoothed curved W surface. The specimens were then mounted into the APT chamber. Due to the high mobility of Li, very low temperatures are preferred. Cooling below 60 K, on the other hand, led to frequent sample fracture. In APT, elements of samples are evaporated by applying a DC voltage besides laser or electrical pulses. Figure 5.2 shows the quite complex mass spectrum of a-LFP/W. Here, laser-assisted APT was used to map and correlate the three-dimensional distribution of Lithium (Li), the transition metal cations (Fe), phosphorous (P) and oxygen (O). Li, Fe, and W peaks are well distinguished. Additionally, their complex oxide combinations, e.g. $FePO_3$, are found. The observed characteristic isotopes ratio of $^7Li^+$ and $^6Li^+$ is 11.84, which agrees well with its natural

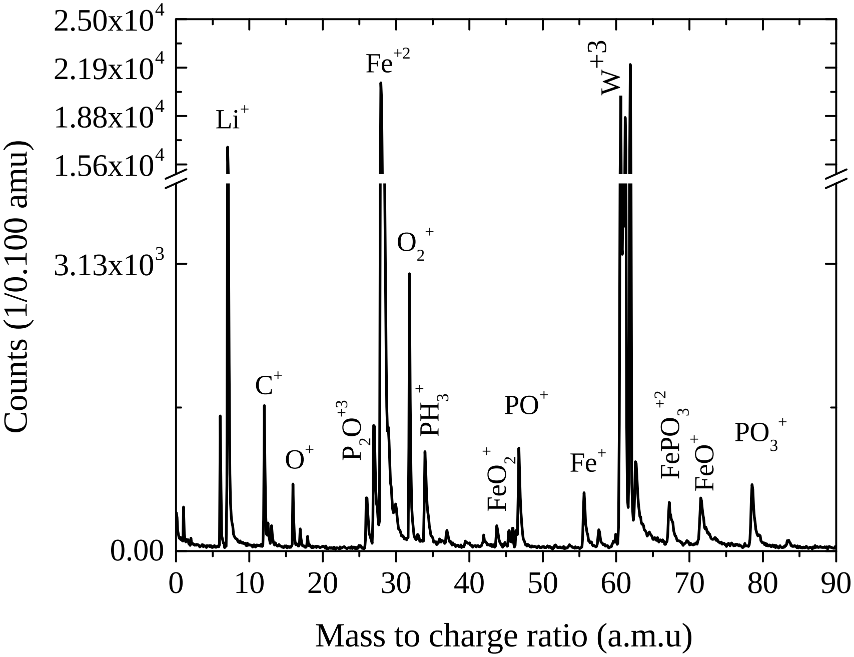

Figure 5.2: Defined mass spectrum of the LFP/W bi-layers system.

abundance ratio of 12.16 [19]. Besides, slight amount of C^{+2} is seen at 6.00 a.m.u. Residual hydrogen gas at m/z = 1.00, 2.00, 3.00 a.m.u is field ionized at the sample apex and originates probably from the chamber environment itself [95, 121]. Also, a small amount of the undesired water was recorded at 17.00, 18.00, 19.00 a.m.u (see Figure 5.2). A list of all possible peaks is tabulated in Appendix A.1. Peak identifications are discussed further in the coming sections.

Figure 5.3 (a) shows the 3D distributions of lithium, iron, phosphorous and oxygen on the tungsten needle. A BCC tungsten (110) with a lattice constant 0.316 nm was used. Considering the cubic crystal structure, the interplanar spacing between lattice planes $\boldsymbol{d_{hkl}}$ is identified as

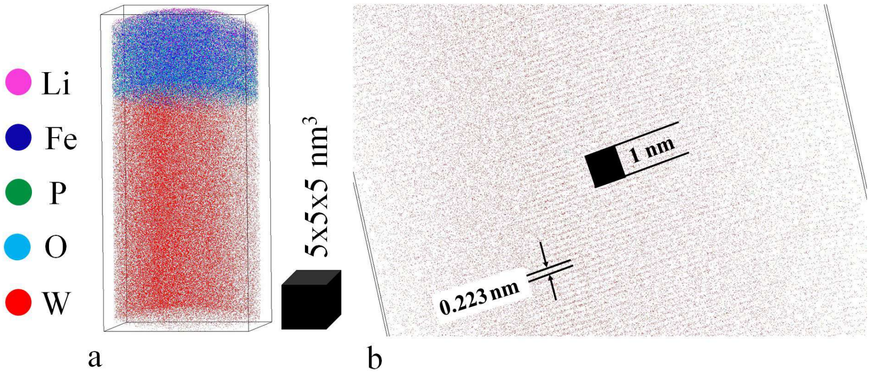

Figure 5.3: (a) Atomic reconstruction of the LFP/W bi-layers. (b) An enlarge image of the lattice planes of tungsten. Li (pink), Fe (blue), P (green), O (cyan), and W (red).

$$d_{hkl} = \frac{a}{\sqrt{h^2 + k^2 + l^2}} \tag{5.1}$$

where ***a*** is the lattice constant. ***h***, ***k***, and ***l*** are the Miller indices of the cubic plane.

$$E = \frac{V}{\beta R} \tag{5.2}$$

where ***E*** is the evaporation field. ***β*** is the compression factor ≈ 4 and ***R*** is the apex radius.

An enlarged volume of the reconstruction shows the lattice planes of tungsten displayed in Figure 5.3 (b). The volume reconstruction was calibrated using the interplanar spacing of tungsten d_{110} ≈ 0.223 nm closest packed plane. In addition, the tip geometry (radius and shaft angle) was adjusted, to set the evaporation field of the second layer at the known evaporation field of tungsten (52 V nm^{-1}). Thereby, the unidentified evaporation field of LFP is approximately calibrated by the known evaporation field of tungsten, which is ≈ 21 V nm^{-1} (see Figure 5.4).

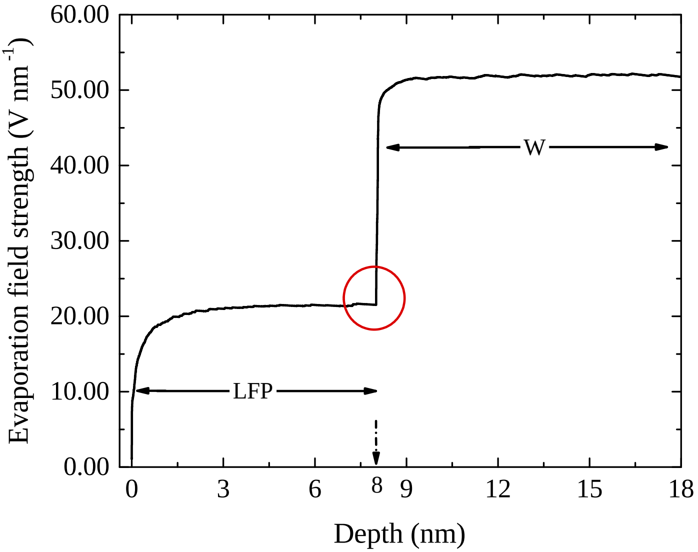

Figure 5.4: Evaporation field difference between the LFP and W. The red circle interprets a sharp unstable transition between the two layers.

Figure 5.3 (a) depicts the 3D reconstruction of LFP/W. A homogeneous distribution of atoms on both sides of the interface between the LFP layer and W can be seen. Distributions details along the tip axis are shown in these compositions profile Figure 5.5. A cylinder with thin slice of 0.50 nm was used to calculate the compositions. Elements were counted for each slice and then plotted against the z-coordinate (tip axis). Excess of Li at the surface points out the migration of Li ions [122]. More details about Li enrichment to the top surface of the tip are represented in section 5.5. To clarify the homogeneity of the measurement, top and side views of 20.00 % Li iso-compositions and 2D Li composition maps are shown in Figures 5.6 (a-d). Quantitative composition data were calculated from the overall measurement. The measured concentrations from the APT were 16.1 ± 1 at % Li, 39.3 ± 1 at % Fe, 13.4 ± 1 at % P, and 31.2 ± 1 at % O. The nominal atomic concentrations are 14.2 at % Li, 14.2 at % Fe, 14.2 at % P, and 57.1 at % O, reinforcing the good

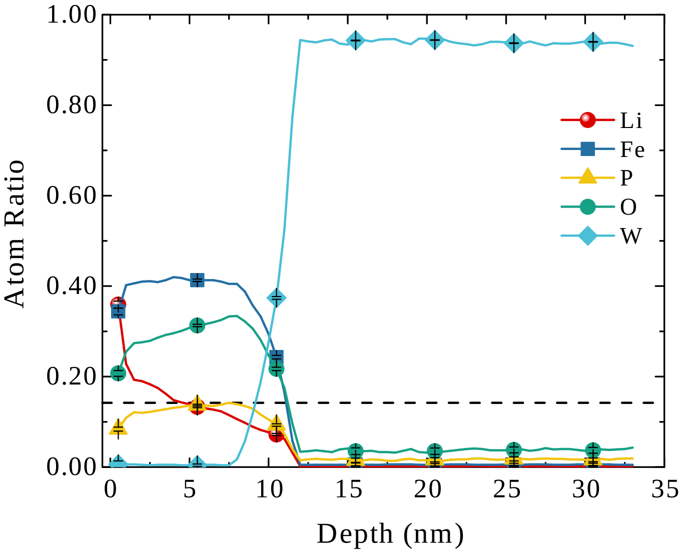

Figure 5.5: Composition depth profile extracted axially along the APT reconstruction of LFP/W. The standard nominal ratio of Li in $LiFePO_4$ is plotted as a black dashed line.

accuracy of APT in measuring Li and P in this sample. For real stoichiometry, artificial water-type species, (e.g., OH^+, H_2O^+, and H_3O^+), were excluded from the calculations. Oxygen showed a noticeable deficiency, as compared to the nominal standard ratios of LFP. From literatures [19, 123–126], except at extremely low laser energies, oxygen is generally known to be deficient during laser-assisted APT of oxides. The evidence points at an eventual loss of neutral O_2 species induced by the high electronegativity of oxygen [19, 127]. Moreover, because of the strong P-O bond, numerous peaks corresponding to P_xO_y complex ions are seen. Iron, on the other hand, is overestimated. Iron excess has been recorded before by D. Santhanagopalan et al. [123], which in some cases can be attributed to Ar^+ plasma hitting of the wall of the sputtering chamber.

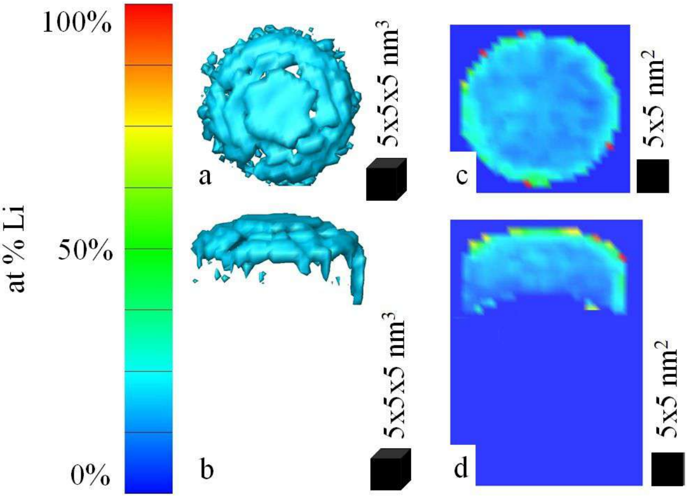

Figure 5.6: Iso-surfaces and the 2D Li composition maps highlighting the Li-rich regions. (a, b) 20.00 at % Li isocomposition top and side views. (c, d) Top and side 2D Li composition maps.

Inspection of Figures 5.4 and 5.5 indicates that only 8 nm out of 40 nm could be measured. The remarkable instability of the LFP layer is mostly due to the geometry of the sample at the curved tungsten surface. APT standard tips have diameters <100 nm and shank angles <10°, but LFP tips display early fractures with these parameters [123]. An illustration of such difficulty can be noticed by a non-smooth field transition between LFP and W, see the red circle in Figure 5.4. However, the smooth transition in the compositions profile indicates non-fracture. Possible layer thickness inaccuracy can also be expected from the thickness monitor and/or a non homogeneous layer growth on the tiny apex. The actual case, however, as good as could be expected, the evaporation threshold of the sputter-deposited LFP layer is identified to be around 21 V nm^{-1}.

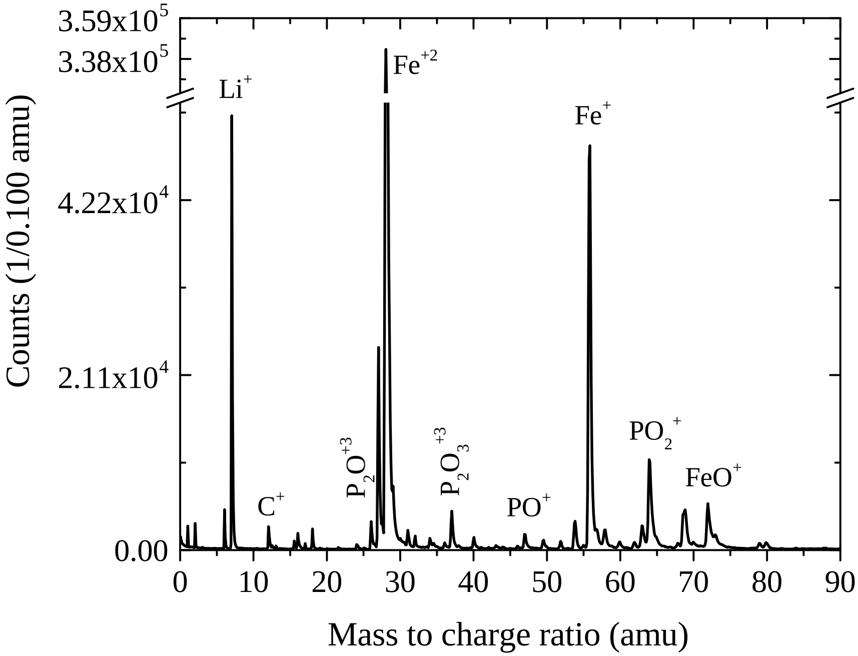

Figure 5.7: Mass spectrum of the LFP$_{5nm}$/Fe$_{5nm}$ stack covered by a protective layer from iron.

5.1.2 LFP/Fe multilayers

For a more stable measurement, LFP layers 5 nm thick each, were stacked in between Fe layers with the same thickness. The LFP$_{5nm}$/Fe$_{5nm}$ sequential was then covered by a protective layer made of pure iron. The structure was reshaped and mounted into the APT chamber at 60 K. Figure 5.7 shows a very similar mass spectrum as recorded before from the LFP/W bi-layers with the absence of tungsten and natural abundance of iron. All peaks are identified. For a more precise evaporation field determination, LFP's evaporation field is again recalibrated using not only the evaporation field of iron (33 V nm^{-1}),

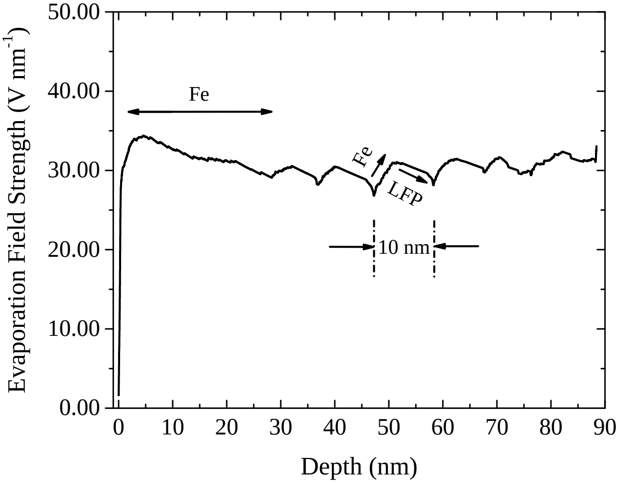

Figure 5.8: Evaporation Fields of the LFP_{5nm}/Fe_{5nm} stack covered by a protective layer from iron.

but also by the thickness of the Fe/LFP layers (10 nm) (see Figure 5.8). The multilayers stack is seen in the 3D reconstruction Figure 5.10.

Figure 5.9 represents the concentration profile along the tip axis. The stoichiometric ratios are found to be substantially far from the nominal values. The measured concentrations in only one LFP layer were 3.2 ± 1 at % Li, 75.3 ± 1 at % Fe, 9.4 ± 1 at % P, and 12.1 ± 1 at % O, whereas the nominal atomic concentration values are 14.2 at % Li, 14.2 at % Fe, 14.2 at % P, and 57.1 at % O. Strong deficiencies in Li, P, and O were observed. Furthermore, a higher evaporation field in the multilayers system than the bi-layers system (LFP/W) is seen, as shown in Figure 5.8. Non-stable stoichiometric measurements or field conditions could be achieved in the multilayers system. As a result of evaporating the LFP and Fe from the sides of the next layer at the same time, the evaporation field is influenced. And because of the high evaporation field, Li evaporates between the pulses leading to a loss of Li. Overall, the evaporation field of LFP is, however, again specified to locate around 25 V nm^{-1}. Lastly, Li layers in Figure 5.10 (b) show thinner thickness than what

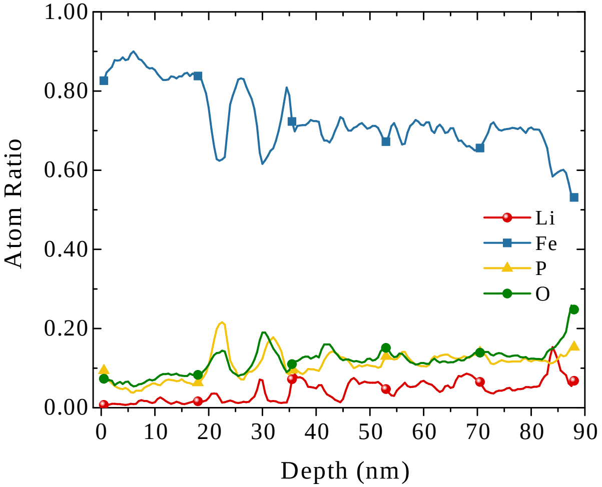

Figure 5.9: Composition profile of the LFP$_{5nm}$/Fe$_{5nm}$ stack covered by a protective layer from iron.

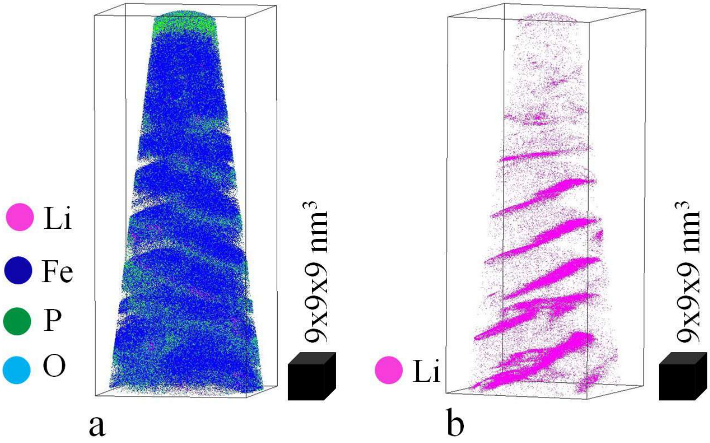

Figure 5.10: (a) 3D atomic reconstruction of the LFP$_{5nm}$/Fe$_{5nm}$ stack covered by a protective layer from iron. (b) Distribution of Li through the stack. Li (pink), Fe (blue), P (green), and O (cyan).

was sputtered (5 nm). Li in LFP layers shows a movement to the top interface leaving empty FP layers. This phenomenon is explained in detail in the following sections.

5.2 Amorphous LFP

A reliable interpretation of APT measurements for LFP requires a reasonable large amount of atoms, which isn't practically possible in needles with sharp shank angles and/or multilayers stacks, especially in view of the poor mechanical stability of LFP. Furthermore, the strong P-O bonds and the highly mobile Li atoms are challenges [128]. Tips are cooled down during the measurements to 60 K by which Li evaporates only by applying an external field and it is sufficient to immobilize atoms during the measurements.

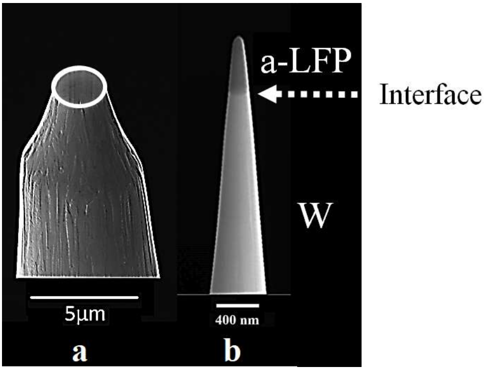

Figure 5.11: (a) SEM image of the 2 μm W post after flatting by the FIB. The top surface is marked by a white circle. (b) The same 2 μm W post after sputtering a thick 1-2 μm layer of LFP then reshaped by the FIB. The LFP is capped as a dark black colour on the tungsten.

Due to the probable stress evolving during the crystallization of LFP, which would make APT analysis even more difficult, the amorphous LFP state was studied first. For preparation of amorphous film, flat cross section of tungsten posts (2 μm diameter) served as substrates (see Figure 5.11 (a)). These posts are made by the electropolishing method, see section 3.1, then followed by some flatting using the FIB, see section 3.4.2. A thick amorphous LFP layer 1-2 μm was deposited on the W posts. Figure 5.12 shows the quite complex mass spectrum of the amorphous LFP. The dominating single Li^+ and Fe^{+2} ions parallel to other ions of O^+ and Fe^+, are clearly seen. On the other hand, complex molecular fragments of Li_2O^{+2}, FeO^{+3}, $O_2{}^+$, $PH_2{}^+$, $PH_3{}^+$, FeO^{+2}, $P_2O_3{}^{+3}$, $PO_3{}^{+2}$, $P_2O_4{}^{+3}$, $FeO_2{}^{+2}$, $P_2O_3{}^{+2}$, $P_2{}^+$, $PO_2{}^+$, $P_2H_2{}^+$, $P_2H_3{}^+$, $FePO_3{}^{+2}$, FeO^+, $PO_3{}^+$, $Fe_2O_3{}^{+2}$, $P_4O_8{}^{+3}$, $PO_4{}^+$, $HPO_4{}^+$, $FePO_3{}^+$, $P_2O_5{}^+$, $FePO_4{}^+$, $P_2O_6{}^+$ appear. Again, Appendix A.1 lists all possible peaks.

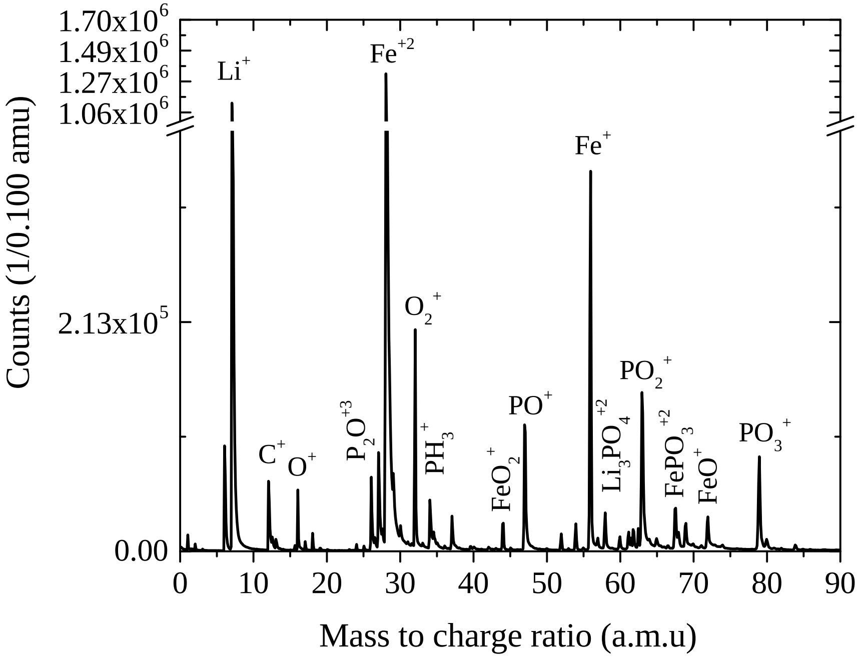

Figure 5.12: An example of a mass spectrum of the amorphous LFP measured at laser power 30 mW. Each peak is well separated and has a good signal to noise ratio. To clarify the background, the figure was drawn with broken y-axis.

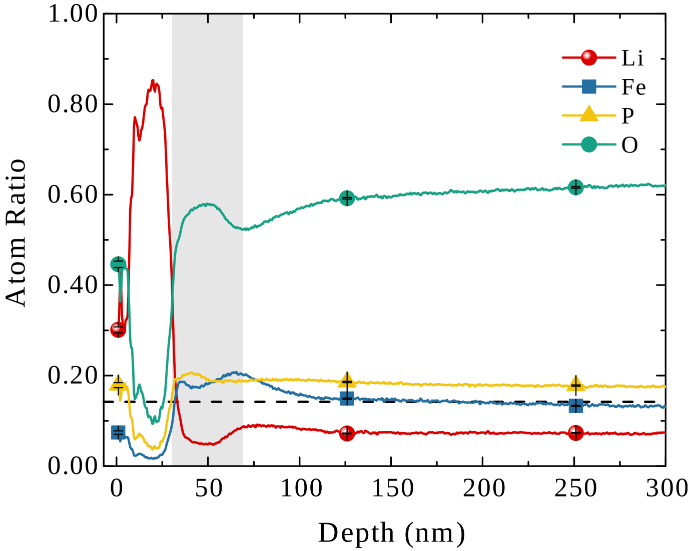

Figure 5.13: Concentration profile extracted along the tip axis of the amorphous LFP. The tip was measured at laser power 60 mW. The standard nominal ratio of Li in $LiFePO_4$ is plotted as a black dashed line. The gray area marks the depletion region.

To explore the analysis of the amorphous LFP, a wide range of laser powers was examined. The measured concentrations for the amorphous LFP at laser energy 60 mW were 11.8 ± 1 at % Li, 15.2 ± 1 at % Fe, 16.9 ± 1 at % P, and 56.1 ± 1 at % O, which fit convincingly to the nominal atomic concentration values 14.2 at % Li, 14.2 at % Fe, 14.2 at % P, and 57.1 at % O. It is worth mentioning that the sputtered LFP layer was independently measured by Inductively Coupled Plasma - Optical Emission Spectrometry (ICP-OES) and found to be $Li_{1.12}Fe_{1.00}P_{0.93}O_{4.00}$ assuming no oxygen loss. The measured APT concentration values are not far from the ICP-MS values. For more reliable comparisons, APT datasets can be renormalized independently of O and compared with the sum of Li, Fe, and P or directly to the anchor element Fe. The measured ratios as compared to Li+Fe+P were 26.9 ± 1 at % Li, 34.5 ± 1 at

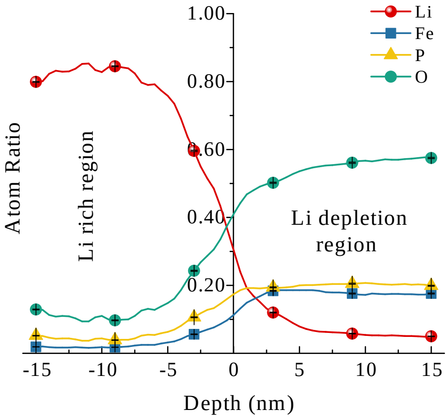

Figure 5.14: Proximity histogram obtained across ±15 nm of the interface showing the concentration partitioning between the Li rich and poor regions.

% Fe, and 38.5 ± 1 at % P, which are slightly under estimation of the nominal concentration values are 33.3 at % Li, 33.3 at % Fe, and 33.3 at % P. The composition ratios verify a reasonable quantification of the APT.

Figure 5.13 depicts the depth concentration profile along the tip axis. Li enrichment at the surface is recorded that appears to correlate with some Li depletion observed in later stages of the measurement. This clear observation points out a migration of Li ions during the analysis [122]. Due to field-driven ion migration, Li redistributes within the dielectric LFP material [122, 123]. At the beginning of the measurement, practically only Li is measured. The majority of the Li is apparent at the top surface (see Figure 5.15). In correspondence, a steady axial variation is evident for Fe, P, O concentrations.

To get a better understanding of this Li redistribution, a compositional partitioning analysis across ±15 nm of the Li rich and poor regions was checked. A perpendicular crop cylinder was used to quantify the region of interest. Figure 5.14 quantitatively represents the composition profile of the Li rich and poor regions. An apparent interface appears as a result of strong Li redistribution during measurement between the Li rich/poor regions. Before the interface, the concentrations were estimated to be 78.9 ± 1 at % Li, 2.9 ± 1 at

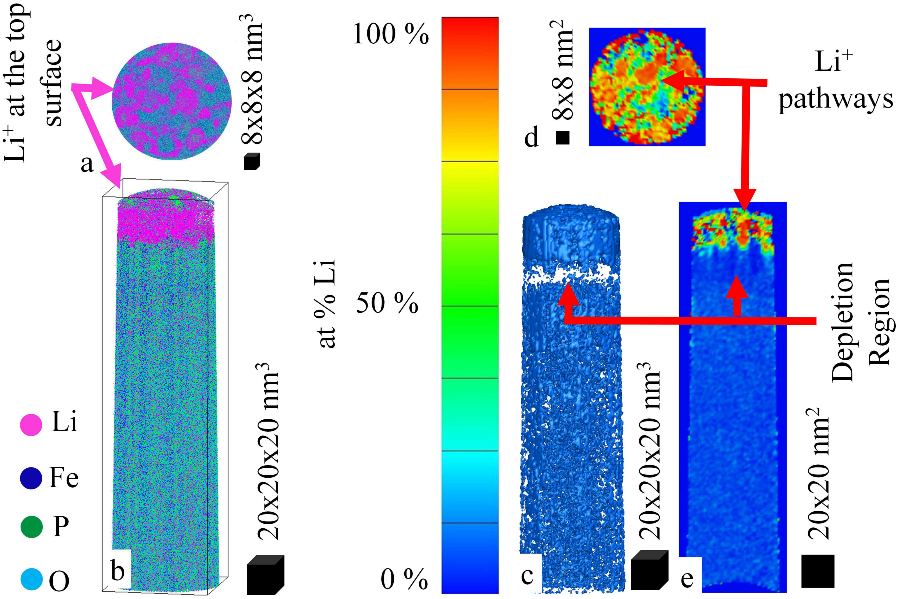
Li+ at the top surface
a
8x8x8 nm3
Li
Fe
P
O
b
20x20x20 nm3
at % Li
100 %
50 %
0 %
d
8x8 nm2
Li+ pathways
c
20x20x20 nm3
e
20x20 nm2
Depletion Region

Figure 5.15: (a) Top and (b) side views of the 3D reconstruction for the amorphous LFP; Li (pink), Fe (blue), P (green), and O (cyan). (c) A 10.00 at % Li iso-composition surface highlights the Li-enriched/poor regions throughout the reconstructed volume. (d) Top and (e) side inner views of 2D Li composition maps, red regions represent high charge Li density, while lower densities are illustrated in green and blue. The colour scale bar of sub-figures (c-e) is shown in the middle of the Figure. The geometrical scale bar is drawn as a black box beside each sub-figure.

% Fe, 5.4 ± 1 at % P, and 12.8 ± 1 at % O in the Li rich region, while the poor region after the interface had 13.8 ± 1 at % Li, 17.5 ± 1 at % Fe, 19.0 ± 1 at % P, and 49.7 ± 1 at % O. Except for low laser energies, Li rich region is directly followed by a depleted Li region (see Figures 5.13, 5.14, and 5.15 (c, e)). Depletion volume is directly related to the laser energy and partly reflects the amount of Li moved to the top surface. Under the impact of the fields, Li is pulled from the sublayers leaving a partly depleted Li region. Li is pulled out

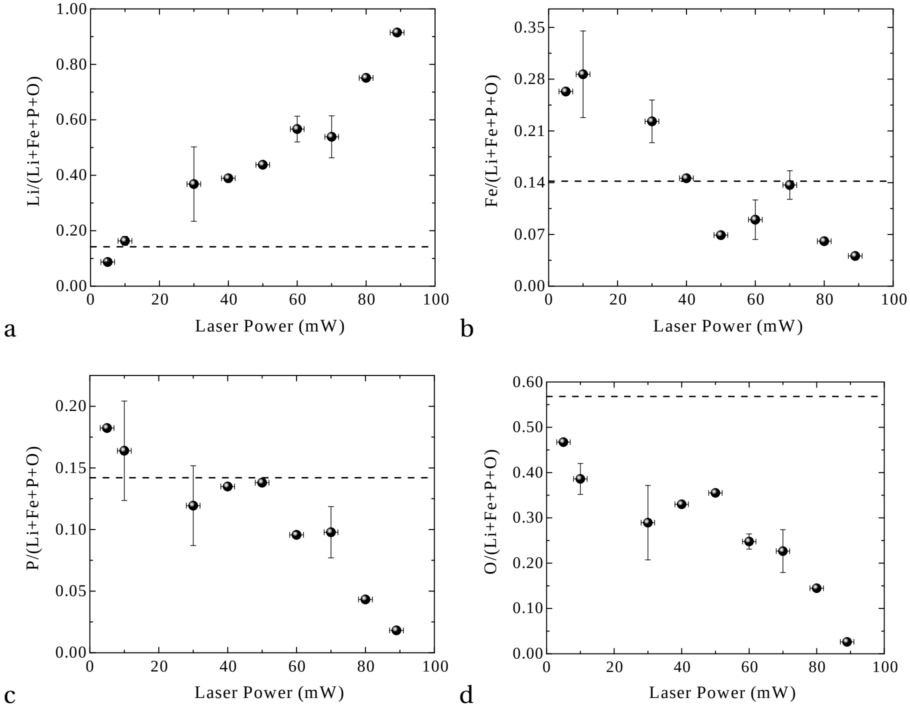

Figure 5.16: (a) Li, (b) Fe, (c) P, and (d) O concentrations with respect to (Li+Fe+P+O) as a function of the laser power. The standard nominal ratio of each element in $LiFePO_4$ is plotted in black dashed line.

from the tips from self created spots, see 2D Li composition map Figure 5.15 (d, e). Lastly, further analyses were carried out to quantify the Li migrations in detail.

The averaged compositions measured by APT for amorphous LFP are shown in Figure 5.16. The experimental measurements and the expected nominal values (dashed lines) are presented. In general, Li is strongly influenced by the laser power in a direct relationship; conversely, Fe, P, and O show reverse dependence to the laser power (see Figure 5.16). In contrast, Santhanagopalan et al. had found constant Li, Fe, and P concentrations in the crystalline LFP [123]. O, on the other hand, had a remarkable reduction with increasing the laser power. However, amorphous LFP in this work shows a Li leading enrichment at the tip front, which makes possible significant deviations to the stoichiometric ratios. The Li local enrichment observed here confirms a faster Li diffusivity in amorphous samples than crystalline samples. Inevitable redistribution of Li was observed before by Greiwe et al. in APT of dielectric Li-Borate glass tips [122]. To clarify the dependence of the laser power on the local enrichment and therefore the compositions, concentration profiles extracted along the tip axis measured at low laser power (10 mW) are shown in Figure Appendix A.10. The figure represents no Li enrichment at all.

5.3 Crystalline LFP

Crystalline thin films were prepared through an additional annealing of amorphous thin films in ultrahigh vacuum ($<10^{-6}$ mbar) for 5 h at 500 °C. Remarkably, crystalline LFP shows a different mass spectrum as compared to the amorphous LFP. Figure 5.17 shows the mass spectrum of the crystalline LFP measured at laser power 30 mW. Structure of the cathode materials obviously has a decisive influence on the local ion transport and so on the APT analysis. The distinct $^{7}Li^{+}/^{6}Li^{+}$ ratio is 16.38, which is somehow higher than the natural ratio of Li 12.16 [122]. This may be caused by the broadening of the peaks in addition to the background to noise ratio. A major difference between the two LFP structures in the APT measurement is the background level.

Crystalline samples show a higher thermal tailing, potentially as a result of the lower heat conductivity [123]. In the laser-pulsing mode, an unfavorable impact like thermal tailing may occur. Even the ultrashort femtosecond laser shows a slow dissipation for materials with poor thermal conductivity [129]. The poor heat dissipation results in evaporation of atoms delayed after the pulses, which leads to a thermal tail on the higher mass side. Since such tailing might overlap with other peaks at higher masses, it can affect the accurate

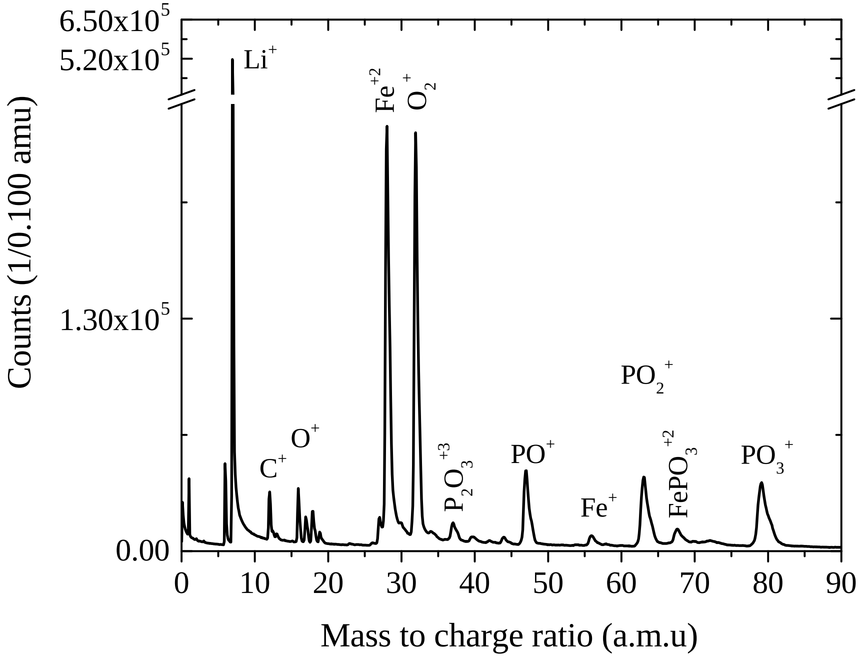

Figure 5.17: An example of a mass spectrum of the crystalline LFP measured at a laser power of 30 mW. To clarify the background to noise ratio, the figure was drawn with broken y-axis.

compositional analysis. Furthermore, this problem not only depends on the pulse width, wavelength, and frequency of the laser, also radius, shaft angle, and heat conductivity of specimens are important factors [130]. In general, the lift out lamella method -the way of preparing tips out of crystalline thin films- has resulted in high background noise level with other battery materials [19]. In preparation details, lift out lamella is cut from a layer structure of LFP/Pt on SiO_2/Si substrate. Because of the poor thermal conductivity of the SiO_2 layer, LFP can demonstrate broader peaks and/or higher noise level.

It should be noted that, unlike the amorphous samples at some laser powers, phosphorous and oxygen of the crystalline samples show stoichiometric im-

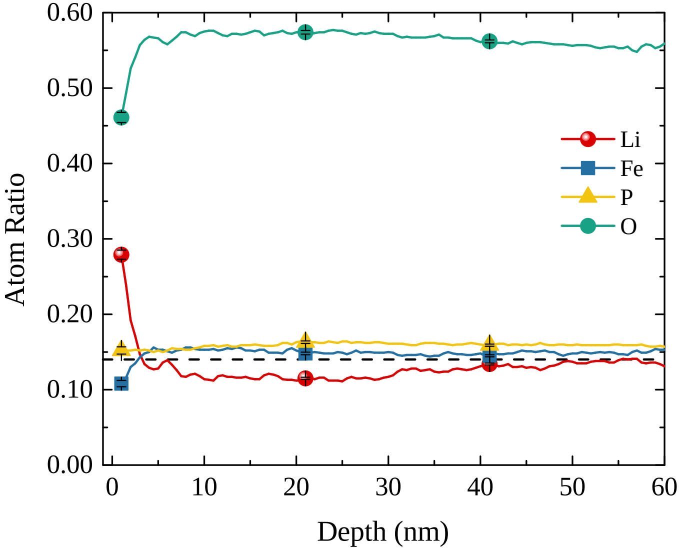

Figure 5.18: Axial extracted composition profiles of the annealed LFP along the tip axis. The tip was measured at a laser power of 40 mW. The standard nominal ratio of Li in $LiFePO_4$ is plotted as a black dashed line.

provements throughout the entire laser range. On the other hand, iron and lithium have showed slight losses as compared to the amorphous state. The concentrations of the crystalline LFP measured at 40 mW laser power were 13.2 ± 1 at % Li, 14.8 ± 1 at % Fe, 15.9 ± 1 at % P, and 56.1 ± 1 at % O. The nominal concentrations are 14.2 at % Li, 14.2 at % Fe, 14.2 at % P, and 57.1 at % O, in excellent agreement with APT results.

Figure 5.18 depicts the axial composition profiles extracted from the 3D reconstruction of the crystalline LFP. Remarkably, in crystalline samples, Li shows a different diffusion behavior than in the amorphous. Only a slight sharp Li peak appeared at the surface referring to remaining low Li diffusion in the crystalline LFP or just initial preferential evaporation. Figure 5.19 illustrates the Li distribution along the tip axis and in top view. Unlike amorphous samples, crystalline samples record a homogeneous distribution of Li along

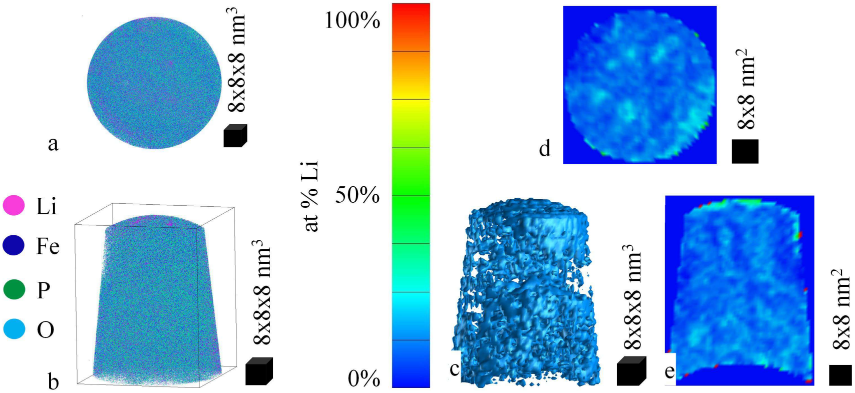

Figure 5.19: (a) Top and (b) side views of the 3D reconstruction of the crystalline LFP; Li (pink), Fe (blue), P (green), and O (cyan). (c) A 14.00 at % Li iso-composition surface. (d, e) Top and side inner views of 2D Li composition maps. The colour scale bar of sub-figures (c-e) is shown in the middle of the figure. The geometrical scale bar is drawn as a black box beside each sub-figure.

the whole axis and only very little enrichment of Li at the top surface. The measured ratios as compared to the Li+Fe+P were 30.1 ± 1 at % Li, 33.8 ± 1 at % Fe, and 36.1 ± 1 at % P, which comes reasonably close to the nominal ratios of 33.3 at %. Checked atomic stoichiometries for all elements in crystalline samples offer nearly perfect composition values over the whole laser range (5 to 60 mW) and throughout the whole tips axes. In contrast to many reports on oxygen related deficiency in APT of oxides. A slightly higher oxygen content is observed.

5.4 LFP at different laser powers

A more reliable evaluation can be achieved by normalizing possible geometrical influence -radius and shaft angle, laser to apex position. To get an overview of the general behavior, laser powers were changed during the mea-

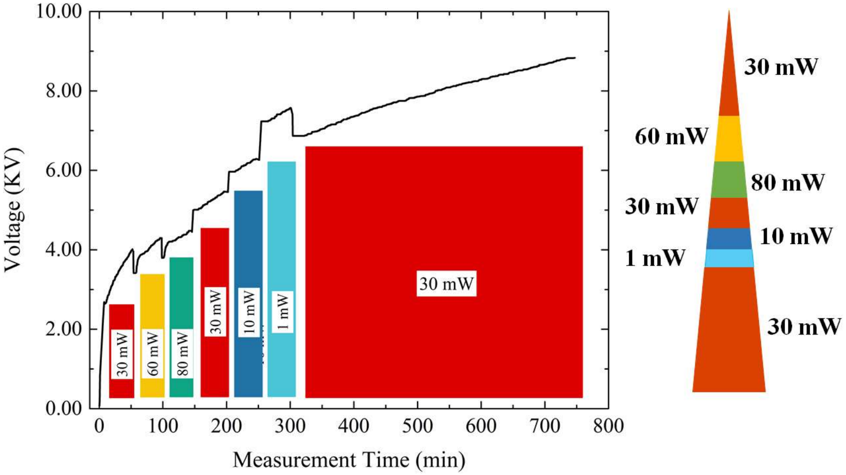

Figure 5.20: (Left) DC voltage evolution curve of the amorphous LFP at different laser powers. Laser powers are represented in different colours. (Right) Schematic diagram shows the laser power values and their orders during the measurement. At each laser power 2 millions of events were counted, except the last laser power, which delivered 18 millions of events. The laser power of 30 mW was selected as a measurement reference.

surement of a single tip with an amorphous LFP layer. Figure 5.20 represents the DC voltage evolution in terms of the laser power. The DC voltage is automatically controlled to keep evaporation rate constant at the desired preset level. General increase of the DC voltage during the measurement as a result of tip blunting is noticeable. In addition, however, the DC voltage correlates closely with the laser power. During the analysis, a DC voltage is applied in such a way that the electric field is slightly lower than the evaporation threshold of the surface atoms. Femtosecond pulses are superposed to the DC voltage to achieve the evaporation condition of the material. DC voltage relates directly to the applied laser power to achieve the evaporation field of the material. The number of atoms that can be evaporated per second called evaporation rate $\boldsymbol{\Phi_{evap}}$ and can be written as an Arrhénius law, Eq. 5.3.

Table 5.1: Stepwise variation of laser power in the experiment shown in Figure 5.20, laser powers and their orders at the same tip.

Measurement Order	Laser Power (mW)	No. of Events (milion atom)
1	30	2
2	60	2
3	80	2
4	30	2
5	10	2
6	1	2
7	30	18

$$\Phi_{evap} = \nu_0 \cdot exp\left(\frac{-Q(E)}{K_B T}\right) \tag{5.3}$$

where $\boldsymbol{\nu_0}$ is the frequency of the vibrated atoms on the surface as a result of the thermal agitation. $\boldsymbol{K_B}$ and $\boldsymbol{T}$ are the Boltzmann constant and the absolute temperature, respectively. ***Q(E)*** is the field dependant height of the barrier and can be written as

$$Q(E) = Q_0 - \sqrt{\frac{n^3 e^3}{4\pi\epsilon_0} E} \tag{5.4}$$

where $\boldsymbol{Q_0}$ is the energy required to remove an atom from the surface when no electric field is applied to the tip. $\boldsymbol{n}$ and $\boldsymbol{e}$ are the ionization state and the electron charge, respectively. $\boldsymbol{\epsilon_0}$ is the dielectric permittivity of the vacuum. $\boldsymbol{E}$ is the applied electric field.

Table 5.1 represents the powers and their sequence. After collecting 2 million atoms, laser power was varied. The measurement ended by 18 million atoms. Three periods at the same laser power of 30 mW were chosen to test for any kind of instabilities and/or fluctuating compositions. The three regions can be extrapolated to each other giving rise to the reliable stability of the measurement.

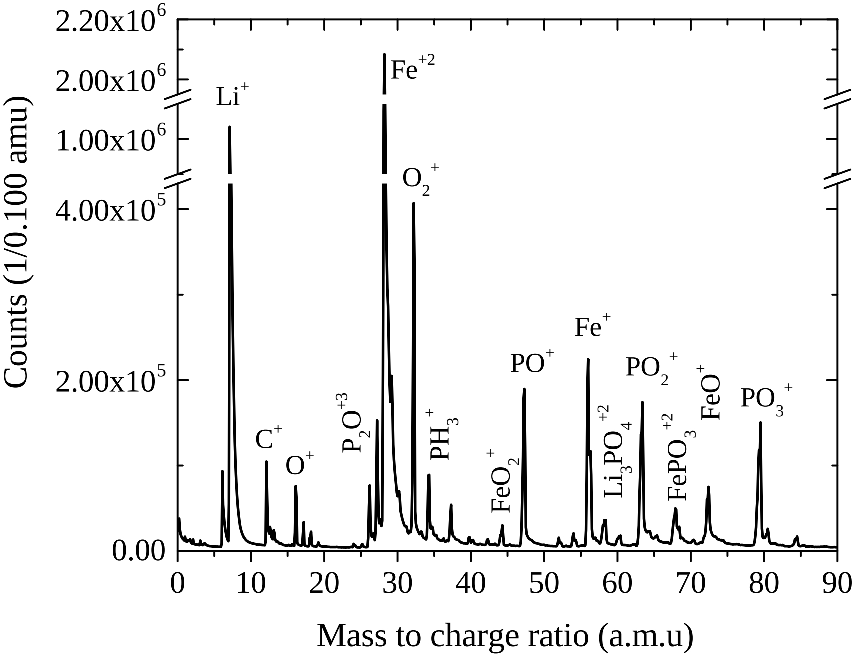

Figure 5.21: A defined mass spectrum of the amorphous LFP measured at different laser powers. Table 5.1 illustrates the laser powers and their ranks.

Figure 5.21 shows the overall mass spectrum of this measurement, for comparison see Figure 5.12. The characteristic $^{7}Li^{+}/^{6}Li^{+}$ ratio is found to be 12.20, close to the literature value of 12.17. The measured concentrations from the APT were 12.4 ± 1 at % Li, 28.6 ± 1 at % Fe, 16.0 ± 1 at % P, and 43.0 ± 1 at % O, and compared to the nominal atomic concentrations 14.2 at % Li, 14.2 at % Fe, 14.2 at % P, and 57.1 at % O. Similar deficiencies and excesses of elements for the amorphous LFP were discussed in detail before in section 5.2.

Fe^{+} and Fe^{+2} are measured simultaneously which enables the determination of the field strength. The measured charge states ratio $Fe^{+2}/(Fe^{+} + Fe^{+2})$ as a

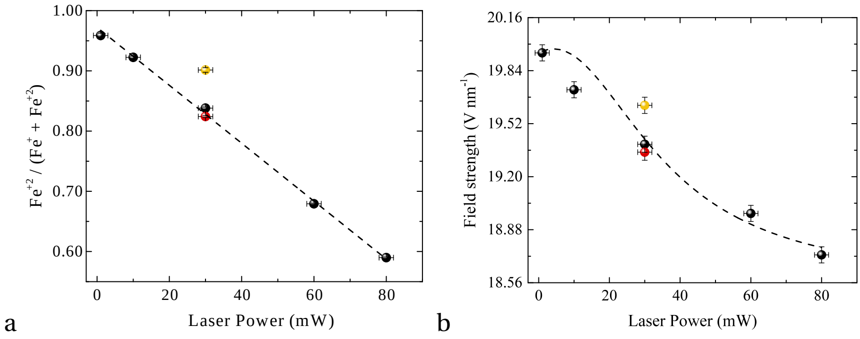

Figure 5.22: (a) Iron charge state ratios $Fe^{+2}/(Fe^{+} + Fe^{+2})$ of the amorphous LFP at different laser powers of the experiment shown in Figure 5.20. (b) The corresponding field strength as compared to the laser power. Field strength was estimated from the Kingham's Fe curves. For a state of clarity, the beginning of the measurement is represented in red colour. This region is interrupted by the Li drift. On the other side, the end of the measurement is represented in yellow colour.

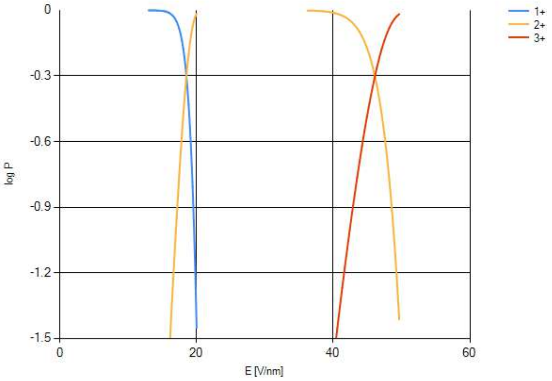

Figure 5.23: Kingham curves of Fe derived from the post field ionization theory [131], (Fe^{+} blue, Fe^{+2} orange, and Fe^{+3} red). After [132].

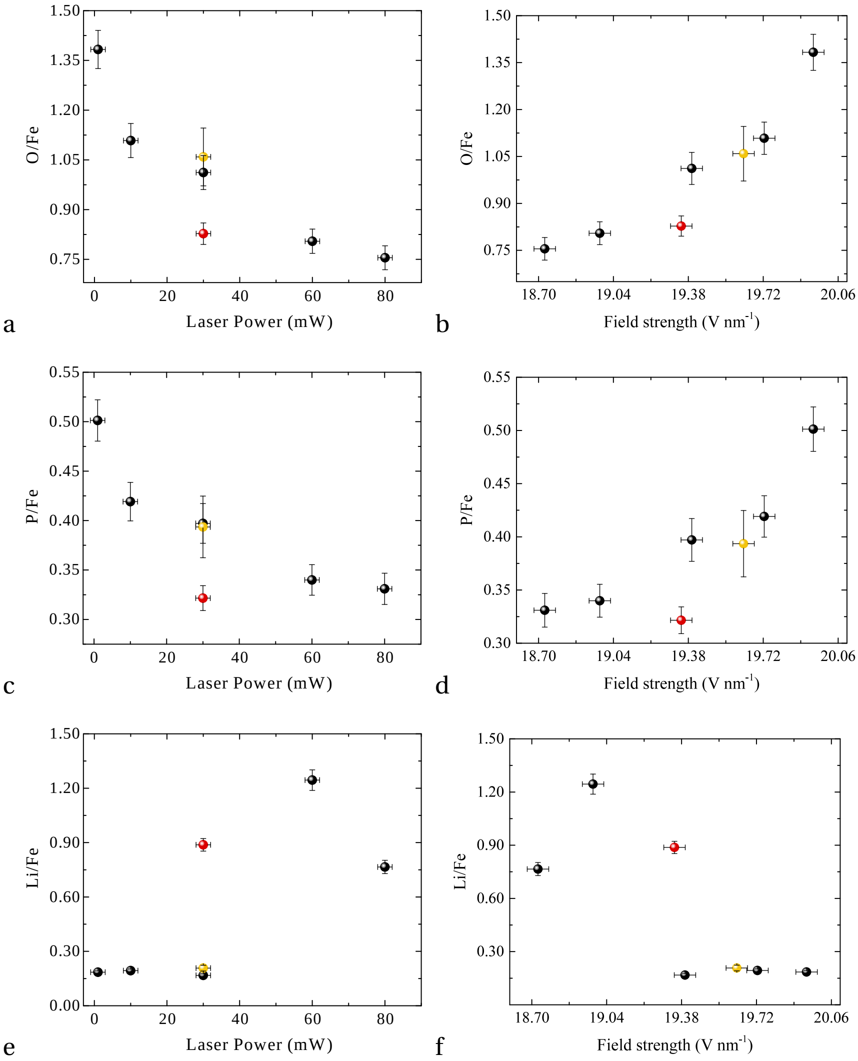

Figure 5.24: Elemental concentration ratios with respect to Fe as a function of the laser power (left) and the field strength (right). (a, b) O/Fe, (c, d) P/Fe, and (e, f) Li/Fe, respectively. For a state of clarity, the beginning of the measurement (30 mW) is represented in red colour. This stage is distinguished by the strong Li drift. On the other side, the end of the measurement (30 mW) is represented in yellow colour.

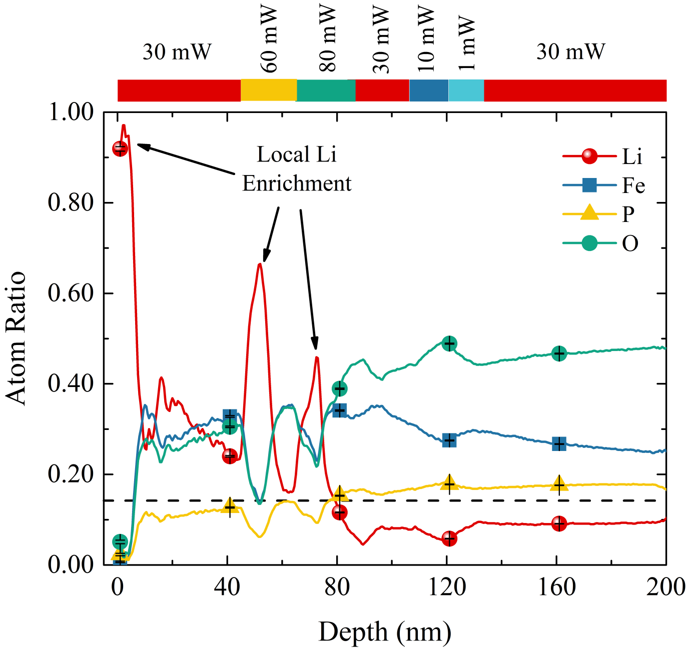

Figure 5.25: Concentration profile extracted along the tip axis of the amorphous LFP. The tip was measured at different laser powers, see table 5.1. The scale bar of the laser powers is put above the figure. Colours of the scale bar are synchronized with Figure 5.20. The standard nominal ratio of Li in $LiFePO_4$ is plotted as a black dashed line.

function of the applied laser power is plotted in Figure 5.22 (a). Almost, linear transition from primarily Fe^{+2} to Fe^{+} with increasing the laser power is observed. This concludes that the higher the laser power is, the less likely is the occurrence of higher charge states. This clearly fits the Kingham's theorem [131]. Figure 5.23 shows the Kingham's Fe curves derived from the post field ionization theory [131]. According to Kingham [131], post-ionization, described by the detected ratio of charge states, is field-dependent and so inversely correlated to the laser power. The corresponding field strengths were calculated from the Kingham curves of Fe and plotted against the laser powers (see Figure 5.22 (b)).

Li movements throughout the tip create inhomogeneous stoichiometry. In this section, the main point is to work out a clear relation of the measured stoichiometry versus the laser power. The stoichiometric ratios of O/Fe, P/Fe, and Li/Fe as a function of the laser power and the field strength are represented in Figure 5.24. The ratios are identified with respect to the stable element Fe. The pair elements, oxygen and phosphorous, show a clear inverse relationship against the laser power and a direct relationship to the field strength (see Figures 5.24 (a-d)). This is well correlated to the strong chemical bonds between the two elements. An oxygen loss at high laser energy has been registered before in the case of $Mg(OH)_2$, CeO_2, and FeO [126, 127, 133]. Devaraj et al. [127] and Kirchhofer et al. [133] have separately explained the O/laser energy related deficiency to the formation of neutral oxygen molecules at lower evaporation fields. The probability of ionizing any desorbed neutral molecules increases with increasing field strength. Reactivity between phosphorous and oxygen appears in our mass spectra by little amount of free phosphorous. This might support the combined P/O related deficiencies in dependence of laser power presented here. P/O are detected together in both deficit in both nature. Contrary to the P/laser power related deficiency presented here in the amorphous phase, D. Santhanagopalan et al. [123] found a relatively small phosphorous variation with respect to the laser energy in the crystalline phase. Amorphous phase behaves differently than crystalline.

Finally, Li shows the pronounced Li enrichment at the tip front, while its total stoichiometric ratio doesn't show a clear trend with neither laser power nor field strength (see Figures 5.24 (e, f)). To explain the Li stoichiometric ratio in detail, concentrations along the whole tip in comparison to the laser power are plotted in Figure 5.25. A Li capped layer is formed at the surface, which confirms the migration of Li ions [122]. Due to field-driven ion migration, Li redistributes [122, 123]. Further new local Li enrichments are seen in the intermediate layers whenever the laser power is temporarily increased. On the other hand, the Li stoichiometric ratios show an unexpected inverse proportion to the laser power. This discrepancy is attributed to the Li movements through the tip during the measurement. Under the impact of laser fields,

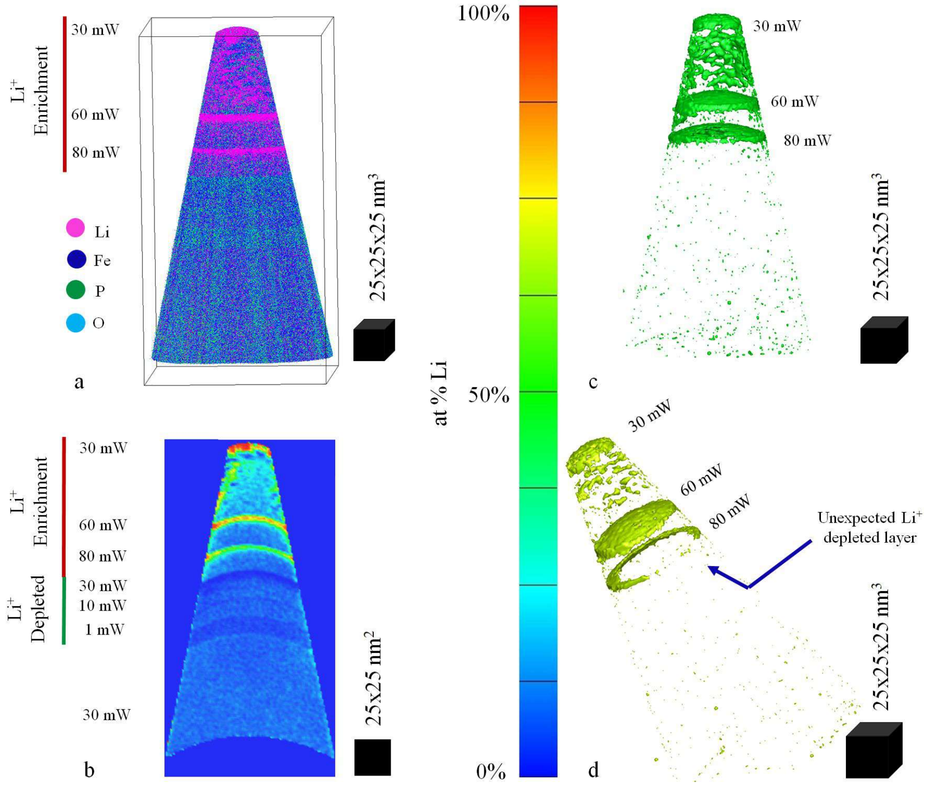
Li$^+$ Enrichment
30 mW
60 mW
80 mW
Li
Fe
P
O
a
25x25x25 nm^3
Li$^+$ Enrichment
30 mW
60 mW
80 mW
Li$^+$ Depleted
30 mW
10 mW
1 mW
30 mW
b
25x25 nm^2
100%
50%
0%
at % Li
30 mW
60 mW
80 mW
c
25x25x25 nm^3
30 mW
60 mW
80 mW
Unexpected Li$^+$ depleted layer
d
25x25x25 nm^3

Figure 5.26: Amorphous LFP at different laser powers; (a) the 3D reconstruction Li (pink), Fe (blue), P (green), and O (cyan). (b) Inner view of the 2D Li composition map. (c, d) 47 and 69 at % Li iso-composition surface. The scale colour bar of the sub-figures (b-d) is shown in the middle of the figure. The geometrical scale bar is drawn as a black box beside each sub-figure.

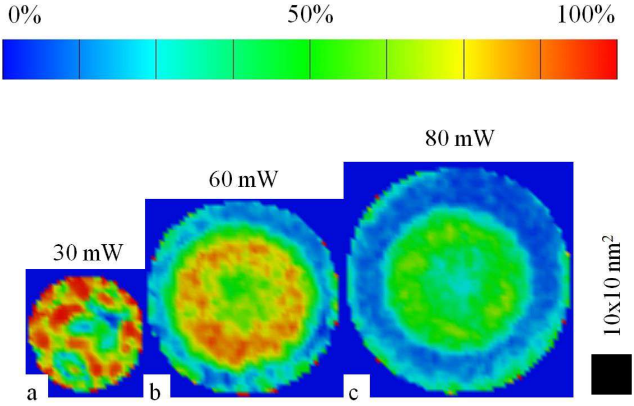

Figure 5.27: Lateral 2D Li composition map of the amorphous LFP at different laser powers; (a) at the top 30 mW, (b) at 60 mW, (c) at 80 mW. The scale colour bar is shown on the top of the figure. The geometrical scale bar is drawn as a black box.

Li is obviously pulled toward the surface, leaving partly depleted Li zones underneath (see section 5.5). By diffusion, empty Li areas are refilled again from the underneath layers. When another laser pulse hits the sample, this process is repeated. The laser power is, however, positively correlated to the remaining Li atoms in the tip. That is the measured Li amount that is affected by the former laser power. In other words, in spite of the stability of the measurement, at the same laser power of 30 mW at top, middle, bottom of the tip, in the measurement stages produces different Li amount as a result of the previous Li movements. Figures 5.26 (a, b) represent the 3D reconstruction of all atoms and the 2D Li composition map respectively. The figures display the longitudinal distribution of Li through the tip. Three Li rich regions are visualized at the top 30, 60, and 80 mW, while other three Li depleted regions are displayed at the middle 30, 10, and 1 mW. The 30 mW stages -top, middle, and bottom- clearly show different Li amounts. Furthermore, an unexpected Li depleted region at the highest laser power 80 mW, displayed in Figures 5.26 (c, d), points out the migrated Li and the created practically empty Li region. These, Li redistributions perceptibly fit to the afore-presented stoichiometric ratios in Figures 5.24 (e, f). Figures 5.27 (a-c) illustrate lateral insights at the top 30 mW, 60 mW, and 80 mW.

5.5 Local Li Enrichment

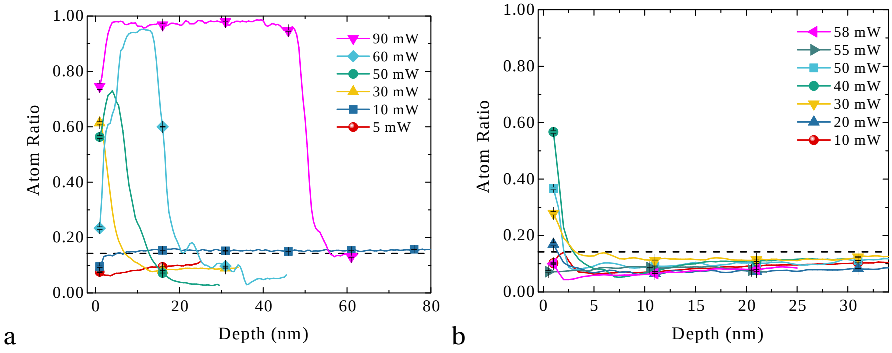

Figure 5.28: Li distribution of both LFP states through the axes of the tips as compared to the laser powers. (a) for amorphous LFP and (b) for crystalline LFP. The standard nominal ratio of Li in $LiFePO_4$ is plotted in two black dashed lines.

A new idiom "Li shooting" is introduced to express the Li segregation to the tip front, which unavoidably appears during the measurement. The physical understanding of this phenomenon is based on the diffusion of Li during the measurement. Both amorphous and crystalline LFP were systematically analyzed over a wide range of laser powers. Figures 5.28 (a, b) represent some of the Li profiles for both amorphous (a) and crystalline (b), LFP at different laser powers. Figures 5.29 (a, b) summarize the areas and FWHMs of the leading Li peaks, as shown in Figures 5.28 (a, b). An example of how both area and FWHM were calculated is illustrated in Figure 5.30 (a). It is obvious that the amorphous LFP shows high Li amounts at the tip front, which is more and more emphasized with increasing laser power, whereas the crystalline phase shows a steady and way smaller segregation amplitude at the surface.

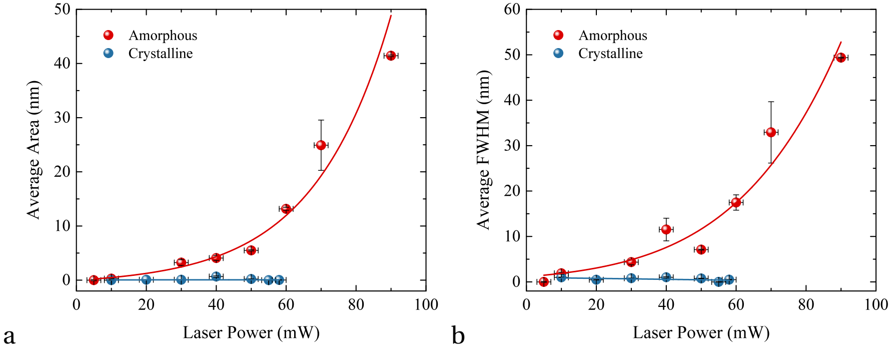

Figure 5.29: (a) Areas and (b) FWHMs of the Li enrichment peaks at different laser powers.

Both lattice structures behave similarly at low laser powers, but they start to diverge at 20 mW. At very high laser powers, the concentration profiles have occasionally some tendency to become unstable as a consequence of non-constant evaporation rates. Figure 5.30 (b) represents an example for this problem in an amorphous LFP measured at laser power of 70 mW. Against normal experience, a ruptured behavior at very high laser power (> 60 mW) is on some occasions possible. This behavior is attributed to the poor mechanical stability and/or the strong Li movement to the surface front.

Li redistribution in case of amorphous LFP is enormous, up to some tens of nanometers, while only a little amount of Li diffuse in crystalline samples. Li redistribution in the amorphous structure cannot be interpreted in terms of the preferential evaporation. It authentically originates from the migration of Li ions when applying the electric field.

Below, a model is presented to understand the observed Li migration. Figure 5.31 schematically poses the theoretical assumption of the proposed diffusion model. Let us assume, the tip is divided into N slices stacked along the tip axis and a_0 is the width of each slice "lattice distance". dt is the time of one diffusion step. Initially, a homogeneous distribution of Li through the tip and constant evaporation flux of atoms were assumed.

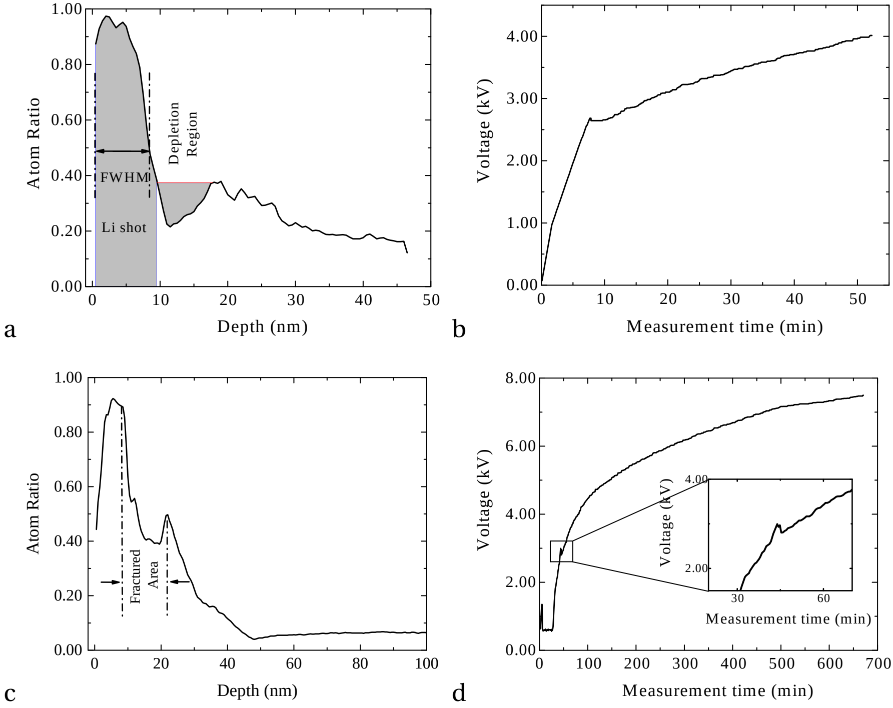

Figure 5.30: (a, b) An example shows the Li axial composition profile and the DC voltage evolution of an amorphous LFP sample measured at laser power 30 mW. The shadowed regions represent the areas of the Li shot and the Li depletion, while the FWHM is represented in the figure. (c, d) Li concentration profile and the DC voltage evolution for an amorphous LFP measured at laser power 70 mW. A possible fracture period of the measurement is shown.

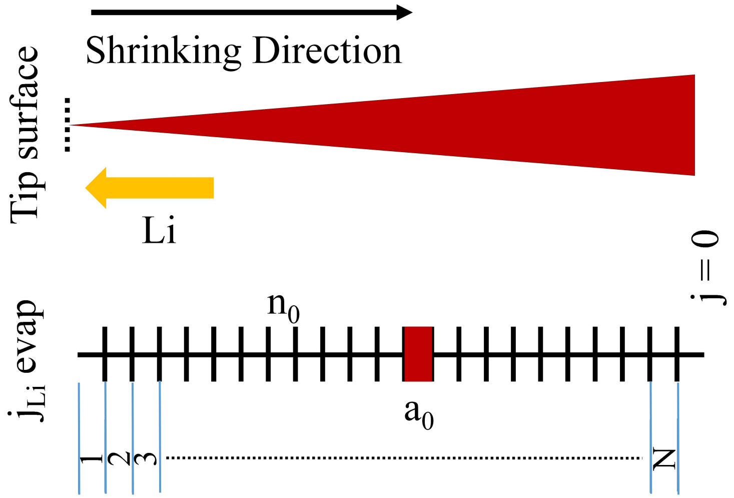

Figure 5.31: Schematic simulates the Li diffusion along the tip. The tip is divided into N slices, a_0 is the lattice plane distance, while n_0 represents the initial Li content in each slice.

By applying a laser pulse, atoms are evaporated from the tip front. Because of the low evaporation field of Li (14 V nm^{-1}) in comparison to the other constituents of LFP or FP (33 V nm^{-1}) as a host, the probability (η) of evaporating Li atoms becomes relatively way higher than that of the remnant atoms.

The over amount of lithium ions taken from the tip leaves empty sites. As a result of lithium mobility inside the tip, other lithium atoms from the underneath volume fill the empty gaps. By this way, Li movements are assumed to be unidirectional parallel to the tip axis and eventually towards the front slice. The first slice is evaporated with ηn_0 of Li atoms, where n_0 is the Li content in the surface. As a consequence of the electronic conductivity of LFP, Li diffuses in absence of any internal electric field. It is only driven by the Li concentration gradient. Movements of Li atoms to the front leave a depleted region at the back of the tip. This distribution of Li goes until the diffusion flux and the surmount in evaporation rate become equal. Then, a steady state profile has developed in the tip.

Li flux $\boldsymbol{J_{Li}}$ inside the tip is quantified by the Fick's law:

$$J_{Li} = -D\frac{dC}{dx} \cdot \frac{1}{\Omega} \approx -D\frac{\Delta C}{a_0} \cdot \frac{1}{\Omega} \tag{5.5}$$

where $\boldsymbol{D}$ is the diffusion coefficient. $\boldsymbol{dC}$ and $\boldsymbol{\Delta C}$ are the atomic fractions of Li gradient. $\boldsymbol{dx}$ is the lattice plane distance ($\boldsymbol{a_o}$). $\boldsymbol{\Omega}$ is the volume per Li atom.

The initial atomic fraction of Li is 0.142 with evaporation field 14 V nm^{-1}, while the host matrix is evaporated at evaporation field 33 V nm^{-1}. The chosen grid distance (a_0) is 1 nm with an integration time step (dt) 0.04 s.

The flux ***J(k)*** in slice number k is identified as

$$J(k) = \frac{C(k+1) - C(k)}{a_0} \cdot D_{Li} \cdot \frac{1}{\Omega} \tag{5.6}$$

where ***J(k)*** is the flux during evaporating slice number k. $\boldsymbol{C_k}$ and $\boldsymbol{C_{k+1}}$ are the concentrations in slice number k and its next slice, respectively. $\boldsymbol{D_{Li}}$ is the Li diffusivity. $\boldsymbol{a_0}$ is the lattice distance. $\boldsymbol{\Omega}$ is the volume per Li atom.

The total evaporation flux from the tip surface is described as

$$J_0 = v_0 \cdot \left\{ C_{Li} \cdot exp\left[\frac{-Q_{Li}(1 - \frac{E}{E_{Li}})}{RT}\right] + C_{Fe} \cdot exp\left[\frac{-Q_{Fe}(1 - \frac{E}{E_{Fe}})}{RT}\right]\right\} \tag{5.7}$$

where $\boldsymbol{v_0}$ is the frequency of the vibrated atoms on the surface. $\boldsymbol{Q_{Li}}$ and $\boldsymbol{Q_{Fe}}$ are the activation energies for Li and Fe in the free field case, respectively. $\boldsymbol{E}$, $\boldsymbol{E_{Li}}$, and $\boldsymbol{E_{Fe}}$ are the present surface electric field, the evaporation threshold fields of Li and Fe, respectively. $\boldsymbol{K_B}$ and $\boldsymbol{T}$ are the Boltzmann constant and the absolute temperature, respectively.

Using an evaporation rate 0.01 atom s^{-1}, the program solves equation 5.7 to get the actual evaporation field on the surface (E). The flux of Li evaporation is represented by: $J_{Li}^{evap} = J_o \cdot \eta C_{Li}$, while the non Li atoms (Fe, P, and O) show an evaporation flux: $J_{Fe,P,O}^{evap} = J_o \cdot (1 - \eta C_{Li})$.

where $\boldsymbol{C_{Li}}$ is the Li concentration. η is the probability of evaporating Li atoms and calculated as

$$\eta = \frac{exp\left(\frac{-Q_{Li}(1-\frac{E}{E_{Li}})}{RT}\right)}{exp\left(\frac{-Q_{Li}(1-\frac{E}{E_{Li}})}{RT}\right)+exp\left(\frac{-Q_{Fe}(1-\frac{E}{E_{Fe}})}{RT}\right)} \tag{5.8}$$

In first attempts, D_{Li} was considered to be independent of Li concentration. But with this, the simulated Li concentration couldn't describe the experimental results, see Figure 5.32

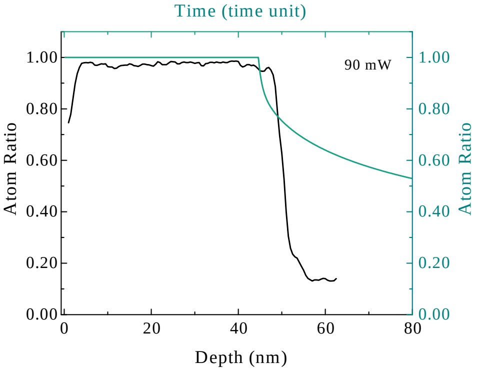

Figure 5.32: Simulated Li concentration profile as compared to the measured one at laser power 90 mW at a constant diffusivity. The black colour shows the experimental result, while cyan colour represents the computed outcome. Note the bad matching after 50 nm depth.

Kirchheim et al. [134] has reported the diffusivity of interstitial solute atoms in disordered materials as a function of concentration. He assumed that a random arrangement of host atoms can provide interstitial sites with different free enthalpies, see Figure 5.33. He has used the well known Fermi-Dirac distribution to describe the occupation of each interstitial sites with only one solute atom at minimum. And dissolved atoms are distributed among the trap sites. At low concentrations, nearly all Li atoms are trapped in low energy sites. With further increase, the amount of mobile Li atoms at sites of higher energy increases.

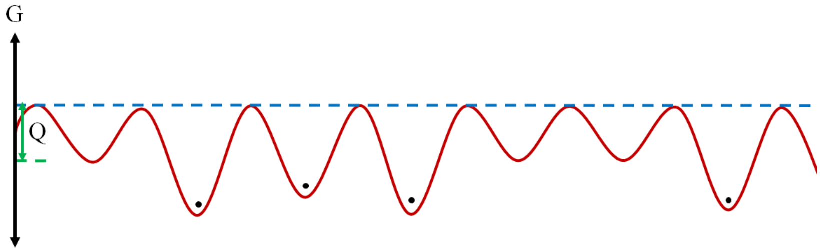

Figure 5.33: Potential trace for solute in a disordered material. The black dots represent the solute atoms. G is the Gibbs free energy. Q is the activation energy.

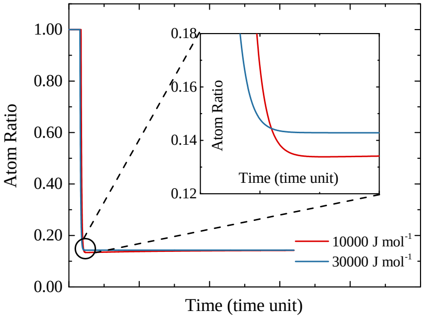

Figure 5.34: Simulated composition profile with different σ values at the same initial diffusivity. An enlarged is set to clarify differences.

The energy distribution of sites ***n(G$_i$)*** in the amorphous material may be represented by a Gaussian function:

$$n(G_i) = \frac{1}{\sigma\sqrt{2\pi}}\, exp\left(-\frac{1}{2}\frac{(G_i - G_0)^2}{\sigma^2}\right) \tag{5.9}$$

where ***G$_0$*** and ***G$_i$*** are the mean free enthalpy and free enthalpy of site i, respectively. ***2σ*** is the Gaussian width of the probability density function.

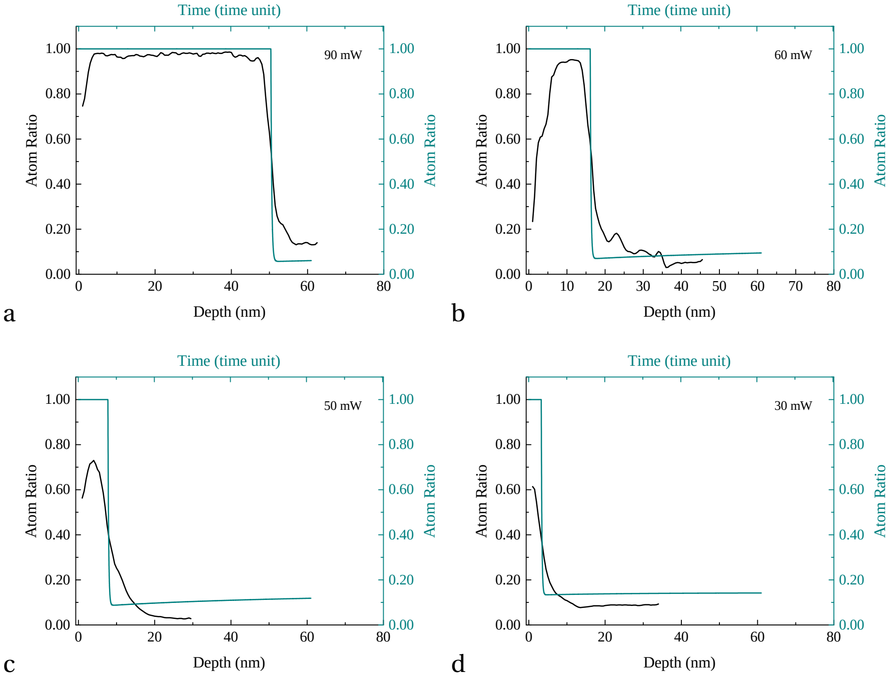

Figure 5.35: Simulated Li concentrations profiles as compared to the measured ones at different laser powers (a) 90 mW, (b) 60 mW, (c) 50 mW, (d) 30 mW. The black colour shows the experimental results, while cyan colour represents the computed outputs of the theoretical model.

With these presumptions Kirchheim calculated the diffusion coefficient for mobile interstitials in an amorphous material as

$$D_{eff} = \frac{D_0\,\sigma\sqrt{\pi}}{RT}\, exp\left(erf^{-1}\left|2C-1\right|\right)^2 \cdot exp\left(\frac{\sigma\, erf^{-1}\left|2C-1\right|}{RT}\right) \qquad (5.10)$$

where $\boldsymbol{D_{eff}}$ is the effective diffusivity. $\boldsymbol{D_0}$ is the hypothetical diffusivity for material at constant side energy. $\boldsymbol{R}$ and $\boldsymbol{T}$ have their normal meanings.

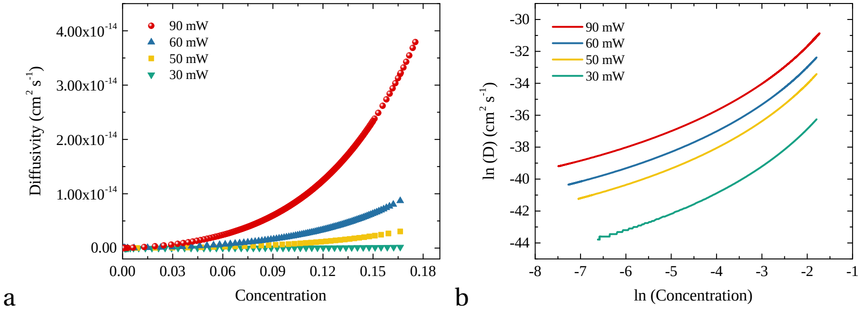

Figure 5.36: The simulated diffusivities at different Li concentrations for different laser power.

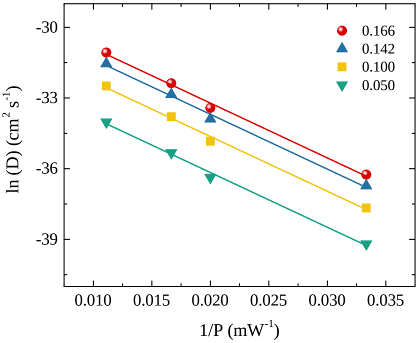

Figure 5.37: The simulated diffusivities at different laser power for different Li concentrations.

$\mathrm{erf}^{-1}(x)$ is the inverse error function (both erf(x) and $\mathrm{erf}^{-1}(x)$ are plotted in Appendix A.21).

Using these concepts, the evaporation and APT analysis of the tips were simulated. First, Kirchheim's diffusion parameters were checked. The impact of width of the density function (σ) was checked by variation from 1000 to 3000 J mol^{-1} at the same diffusivity, but it has shown no significance influence, see Figure 5.34. So, the effect of the width of density function is neglected and only initial diffusivity and temperature are left as free parameters to fit the experimental data.

By fitting the FWHMs, the simulated Li profiles are compared to the experimental results in Figure 5.35. The diffusivity determined by fitting is shown in Figure 5.36. As the applied laser power increases, the diffusivity increases as a result of increasing the efficient temperature. The diffusivity values are in the order of 10^{-14} $\mathrm{cm}^2\ \mathrm{s}^{-1}$ which reasonably fit to the expected values [14].

Figure 5.37 shows the relation between the natural logarithm of diffusivity at different Li concentration vs. reciprocal of the applied laser power in amorphous LFP. The relation obeys the Arrhenius's equation.

$$D_{eff} = D_0\, exp\left(-\frac{Q}{R\omega P}\right) \tag{5.11}$$

where $\boldsymbol{D_{eff}}$ is the effective diffusivity; $\boldsymbol{D_0}$ is a prefactor; $\boldsymbol{Q}$ is the activation energy. $\boldsymbol{R}$ is the universal gas constant. $\boldsymbol{\omega P}$ represents the local temperature in Kelvin. $\boldsymbol{\omega}$ is a converter factor between the local temperature and the applied laser power under the reasonable assumption of proportionality.

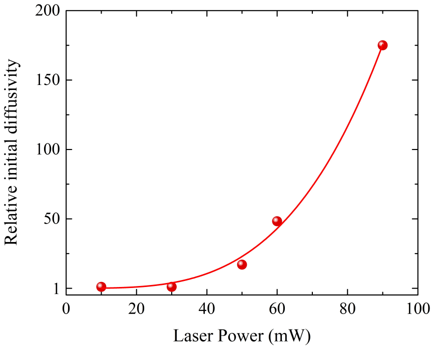

Figure 5.38: Relative initial diffusivity for amorphous LFP calculated from the theoretical model.

Therefore, laser power can represent the local temperature on the tip apex during the measurement. The product of the slope of the plot, Boltzmann constant and ω gives the activation energy of the amorphous LFP.

Figure 5.38 shows the relative change of the "initital" diffusivities as compared to the applied laser power. Li migration in amorphous LFP becomes two orders of magnitudes faster as the laser power increases from 10 mW to 90 mW. Increase of the diffusivity in case of amorphous phase is due to a gradual filling of the low energy sites which decreases trapping. Furthermore, thermal agitation increases the jumping frequencies of Li atoms which in turn can settle Li atoms in high energy states and increase the Li diffusivity. By contrast, the crystalline phase shows no significant diffusion over the investigated laser range. Interstitial sites of the crystalline phase have the same energy and so on a constant diffusivity. While the open network of the amorphous phase requires presumably in general less activation, so that the diffusivity is significantly higher than in the crystalline variant.

6 3D Analysis of Dis-/charged LFP

6.1 LFP at different de-/lithiation states

The local chemistry of the metal cation distributions together with the spatial distributions of lithium are the main factors affecting the battery performance. Understanding of nanoscale distributions of all battery constituent elements as a function of electrochemical cycling is a critical test for the analytical method of battery materials [18]. With this goal in mind, the first evidence for achieving 3D studies of the charging and discharging LFP thin films is provided in this section.

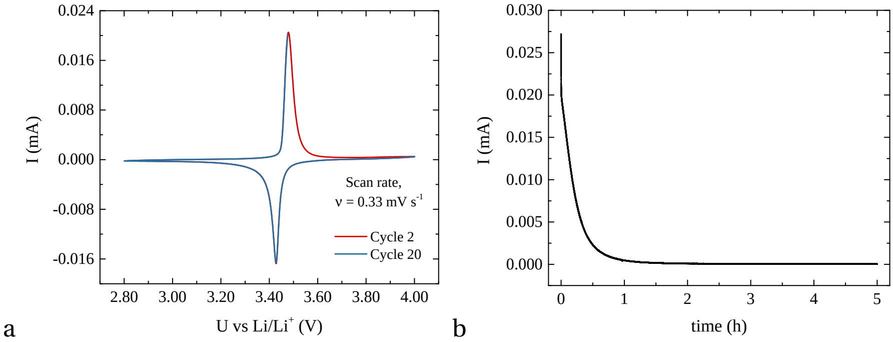

Figure 6.1: (a) CV data of a 300 nm thin LFP film obtained at a scan rate of 0.33 mV s^{-1}, the 2nd (red) and the last 20th (blue) cycles are shown. (b) After the 20^{th} cycle, a constant potential, in this example 3.48 V, was applied for 5 hours to establish an equilibrium distribution of the Li ions.

Crystalline LFP thin films, 300 nm in thickness, were prepared, then electrochemically cycled, see sections 3.2 and 3.3 for more details. The films were initialized at 1.00 mV s^{-1} for 5 cycles then cycled at 0.33 mV s^{-1} (1 C) for 20 cycles between 2.80-4.00 V versus Li/Li^+. To study de-/lithiation with APT

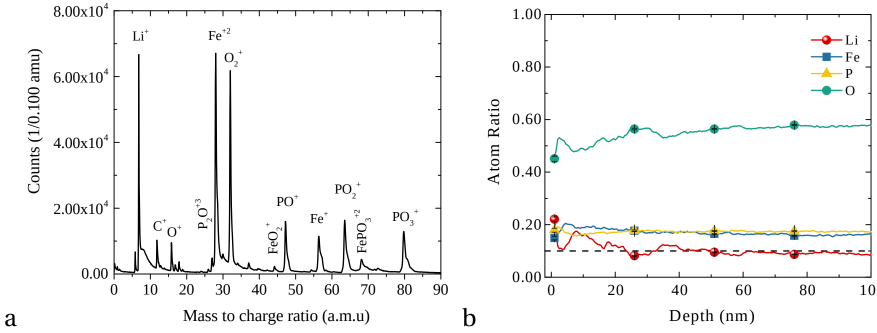

Figure 6.2: (a) Mass spectrum of a discharged LFP, lithiation state 70.00 %. The tip was measured at a laser power of 40 mW. (b) Concentration profiles extracted along the tip axis of a discharged LFP, lithiation state 70.00 %. The tip was measured at a laser power of 40 mW. The standard nominal ratio of Li in $LiFePO_4$ at this lithiation state (70.00 %) is plotted as a black dashed line.

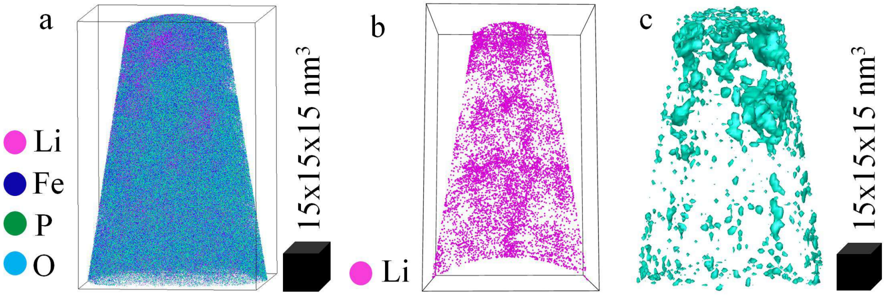

Figure 6.3: 3D reconstruction of the discharged LFP (70.00 %) -(a) All elements ; Li (pink), Fe (blue), P (green), and O (cyan) (b) A slice of 1 nm thick of only Li element, slice size 160x120x1 nm^3. (c) A 28.00 at % Li iso concentration surface highlights the Li-enriched/poor regions throughout the reconstructed volume. Geometrical scale bars are drawn as black boxes beside each sub-figure.

analysis, electrochemical cycling was ended at a characteristic dis/charge potentials for each thin film. An example of a thin film ending at 3.48 V is shown in Figures 6.1 (a, b). The second and the last cycles are shown in Figure 6.1 (a). To equilibrate the Li ions through the whole layer, the constant end potential (E) has been supplied for 5 hours. The exemplary Chronoamperometry (CA) is shown in Figure 6.1 (b).

Dis/charged LFP shows a qualitatively similar mass spectrum as the as-prepared crystalline LFP, as presented in section 5.3. Figure 6.2 (a) displays the mass spectrum of the discharged LFP (termination voltage, 3.48 V equivalent to lithiation state 70.00 %) measured at laser power 40 mW. As observed in the crystalline samples, a high thermal tailing level is also recorded here (see section 5.3 for more details).

The axial compositions of the discharged LFP at a lithiation state 70.00 % are presented in Figure 6.2 (b). The total measured concentrations of this discharged LFP were 12.0 ± 1 at % Li, 18.1 ± 1 at % Fe, 16.2 ± 1 at % P, and 53.7 ± 1 at % O. The expected ratios for LFP at this lithiation state are at 10.4 % Li, 14.9 at % Fe, 14.9 at % P, and 59.7 at % O, in very good agreement with APT results, reinforcing the reliably of APT in measuring the overall content of dis-/charged cathode material. Fe, P, and O select as expected a steady axial concentration. Li, on the other hand, shows a new wavy profile, which has not been seen before and may indicate some heterogeneity in the Li distribution. Only a minute amount of Li has diffused to the top surface indicating that the cryo temperature is sufficient to measure Li ions in their original lattice positions. Elemental maps throughout the tip axis and the top surface are presented in Figures 6.3 and 6.4.

Figure 6.3 separately displays the 3D reconstructions of both (a) all elements and (b) only the Li component to locate possible heterogeneity inside the LFP. To get further microscopic details, 2D density maps were plotted in Figure 6.4. Dis/charged LFP shows concentrated regions over the whole tip where the density of detected atoms is significantly increased (see Figure 6.4). These regions are clearly visible in the 2D maps for the Li component only in Figure 6.5. The figures clearly confirm some heterogeneities. Moreover to be truly sure that the regions of high density represent the Li rich phase, Li density orthoslices and iso-surfaces are shown in Figure 6.6. Li agglomeration is

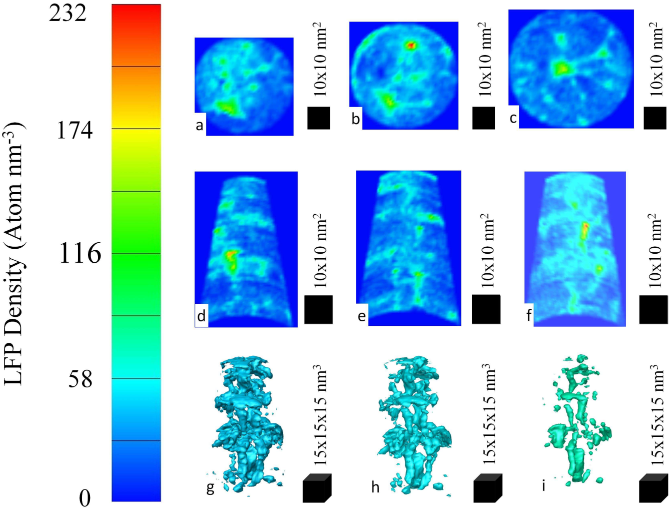

Figure 6.4: (a-c) Top and (d-f) side inner views of 2D density maps of all atoms, red regions represent high density, while lower densities are illustrated in green and blue. (g-i) 47.1, 54.8, and 73.1 atom nm^{-3} iso-density surfaces show the dense regions throughout the reconstructed volume in 3D views. The scale colour bar is shown in the left of the figure. Geometrical scale bars are drawn as black boxes beside each sub-figure.

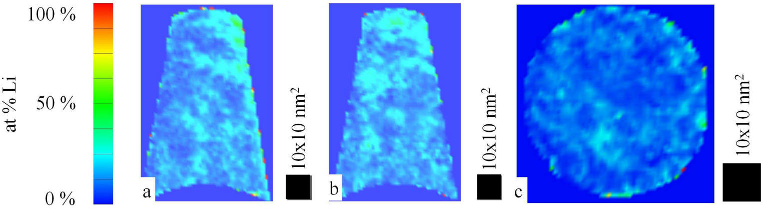

Figure 6.5: (a, b) Side and (c) top inner views of 2D composition maps of Li, red regions represent high concentrated Li regions density, while lower regions are illustrated in green and blue. The scale colour bar is shown in the left of the figure. Geometrical scale bars are drawn as black boxes beside each sub-figure.

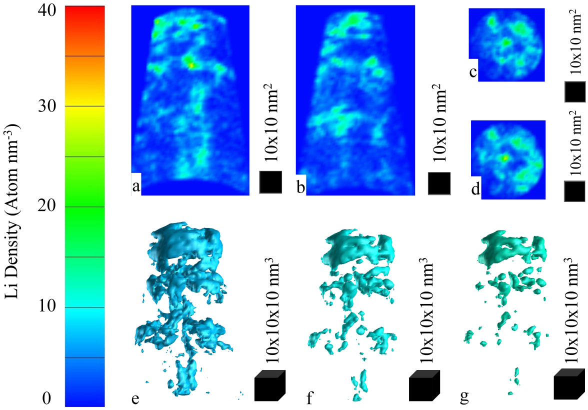

Figure 6.6: (a, b) Side and (c, d) top inner views of 2D Li density maps. (e-g) 7.7, 8.8, and 12.1 atom nm^{-3} Li iso-density surfaces highlight the Li rich/poor regions throughout the reconstructed volume. Lithiation state is 70 %. The scale colour bar is shown in the left of the figure. Geometrical scale bars are drawn as black boxes beside each sub-figure.

clearly visible, which indicates that the detected high density regions are the Li rich LFP phase.

To scan the full de-/lithiation processes, dis/charged thin films were analyzed at different lithiation states. Figure 6.7 (a) represents the CV curve of a 300 nm thin film. In different thin films, the electrochemical reactions were terminated at specific potentials. CV curves are converted to the current to time domain in order to determine the Li concentrations in each film (see Figure 6.7 (b)). Lithiation states can be identified as the ratio between areas of the last half cycle and one half cycle before, displayed in Figure 6.7 (b). Figure 6.7 (a) displays the terminated potentials at the CV curve of crystalline LFP. De-/lithiation processes were checked at different terminating potentials (Lithiation states). Thin film terminated at around 4.00 V exemplify the fully delithiated phase (α), whereas the fully lithiated phase (β) is represented by a film terminated at around 2.80 V. Between 2.80 - 4.00 V a heterogeneous two-phase structure is expected. The full delithiated phase (α) shelled by the full lithiated phase (β) is expected in the intermediate intercalation states for

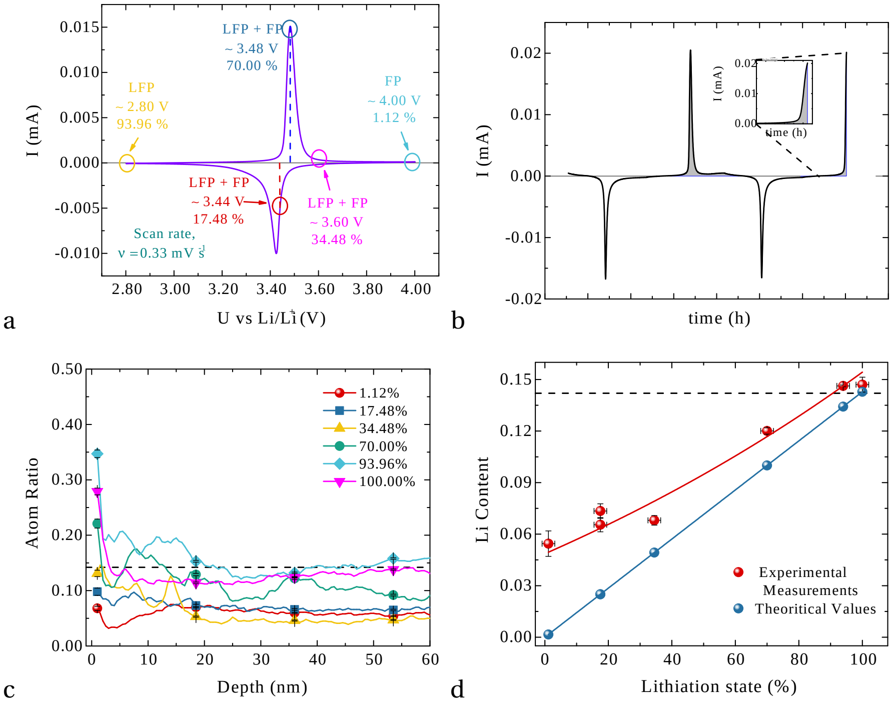

Figure 6.7: (a) CV spectrum of a 300 nm thin LFP film at scan rate 0.33 mV s^{-1}. The figure represents the termination potentials. (b) CV curve in the current versus time domain. (c) Axial extracted Li composition profiles for LFP at different dis/charge states. The tips were measured at laser power 40 mW. (d) Observed Li contents as compared to the theoretical values at different lithiation states. Li amounts were calculated from the whole tips. The standard nominal ratio of Li in $LiFePO_4$ at lithiation state 100.00 % is plotted as black dashed lines in sub-figures (c) and (d).

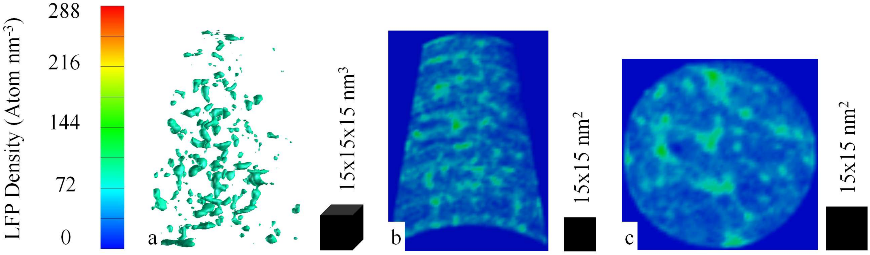

Figure 6.8: (a) 91.4 atom nm^{-3} LFP iso-density surface highlight the rich/poor regions of all elements throughout the reconstructed volume. (b, c) Side and top inner views of 2D density maps of all elements, red regions represent high charge LFP density, while lower densities are illustrated in green and blue. Lithiation state is 1.12 %. The scale colour bar is shown in the left of the figure. Geometrical scale bars are drawn as black boxes beside each sub-figure.

thin film at around 3.44 V. Moreover, the fully lithiated phase (β) shelled by in the full delithiated phase (α) is expected in terminated thin films at around 3.48 and 3.60 V.

Figure 6.7 (c) outlines the axial Li concentration profiles for all dis/charged thin films at different lithiation states. The measured Li amounts as compared to the expected ones are shown in Figure 6.7 (d). Lithiation of the fully delithiated phase ends by filling up all available sites which is reflected by getting the complete Li amount in the APT measurement. By contrast, delithiation of the fully lithiated phase surprisingly records a higher amount of Li than expected. Such surplus of Li in the full delithiated phase may be described by inactive LFP regions inside the grains and can also explain the limited practical capacity of the films.

Existing of such high amount of Li at the fully delithiated phase proves that LFP isn't entirely transformed to FP during the delithiation. This is compatible with the radial model proposed by Anderson and Thomas et al. [35, 51], while it contradicts the classical shrinking core model [15]. When the limited mobility of Li ions through the interface can't sustain the current density, the electrochemical reaction stops without fully transforming the active materi-

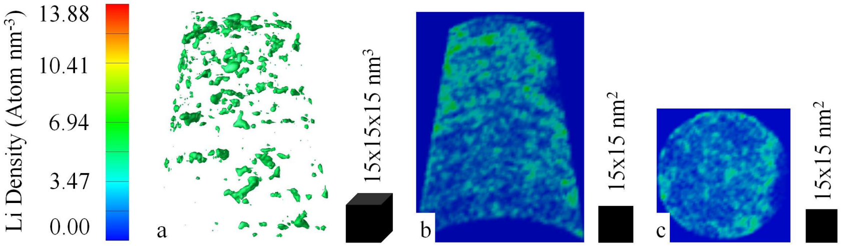

Figure 6.9: (a) 5.7 atom nm^{-3} Li iso-density surface highlight the rich/poor regions of Li element throughout the reconstructed volume. (b, c) Side and top inner views of 2D density maps of Li elements, red regions represent high charge LFP density, while lower densities are illustrated in green and blue. Lithiation state is 1.12 %. The scale colour bar is shown in the left of the figure. Geometrical scale bars are drawn as black boxes beside each subfigure.

als. The reaction leaves inactive $LiFePO_4$ inside the two phase reaction during charging and remnant of $FePO_4$ after discharging [35, 51]. Alternatively, according to Köhler et al. [14], an inactive reaction layer could also be formed in thin films, but our APT measurements contradict Köhler's assumption.

In dead regions or inactive regions, the lithium encounters some barrier to diffusion. To locate such inactive cores in this work, density analyses of the fully delithiated phase were performed for both all elements and the Li component only. Figure 6.8 represents the iso-density surfaces and 2D density maps of all elements, whereas the lithium component is shown in Figure 6.9. As can be seen, the fully delithiated phase still shows the Li rich phase which strongly supports the idea of inactive regions. To quantify the possible phase separation, statistical analysis called frequency distribution analysis was introduced.

6.2 Frequency distribution analyses

In frequency distribution analyses, a reasonable number of events using a cylinder of dimensions 20x20x60 nm^3 was used to statistically observe the

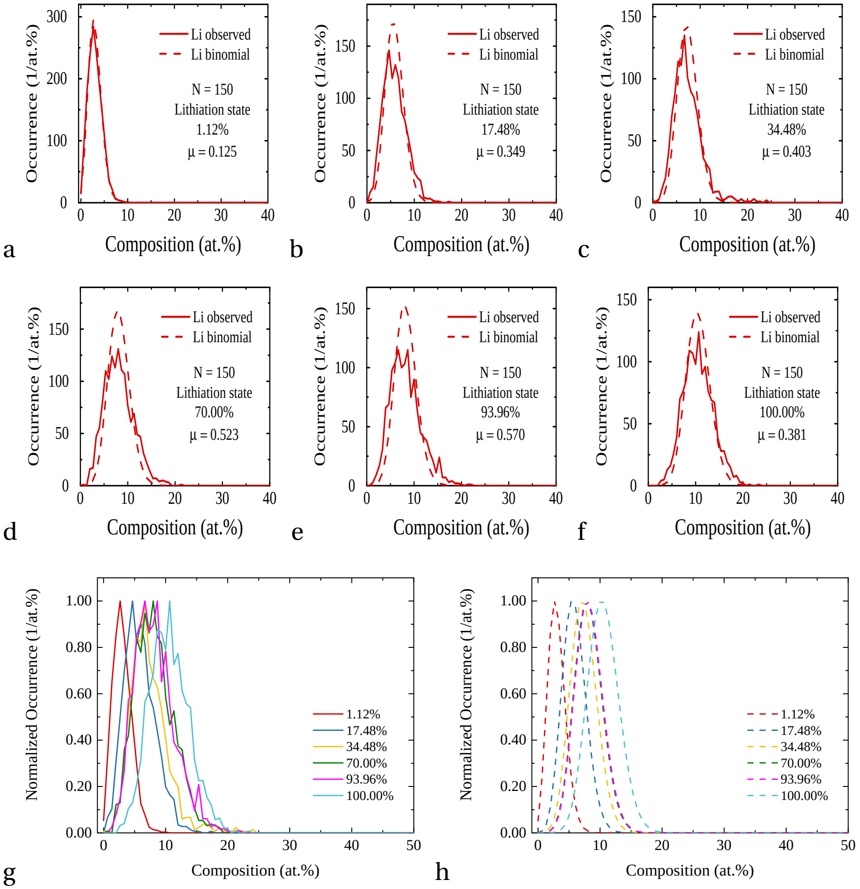

Figure 6.10: Statistical analyses of the Li distribution at different lithiation states. Observed frequency distributions (solid line) in comparison to their binomial distributions (dashed line) with corresponding Pearson coefficients. (a-f) represent lithiation states 1.12 %, 17.48 %, 34.48 %, 70.00%, 93.96 %, and 100.00 %, respectively. (g, h) Normalized frequency distributions for observed and binomial distributions for Li at different lithiation states, respectively.

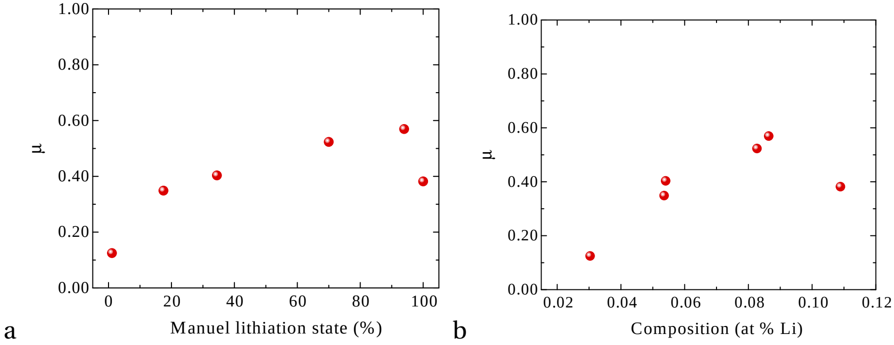

Figure 6.11: (a, b) Pearson coefficients of Li distribution in dis/charged LFP versus the lithiation states and Li concentrations measured by APT, respectively.

possible phase separation. Events were then divided into bins of 150 atom. The composition was calculated for each bin and plotted in a histogram form. A binomial frequency distribution is expected for a random solid solutions [18]. Any deviation from randomness is expressed by a deviation from the binomial distribution [96]. The frequency distribution analyses of Li, Fe, P, and O in LFP at different dis/charge states are shown in Figures 6.10, 6.13, 6.15, 6.17. The statistical relevance of the observed data from the randomness can be indicated by the Pearson coefficient test [86, 92, 96], see section 2.20 for more details. The Pearson coefficient (μ) is a statistical method that measures the linear correlation between two variables, while its value ranges from 0 and 1. This statistical test comes to replace the conventional χ^2 statistic which is unsuitable for comparison of quantities with differently sized system. Pearson coefficient is shown to normalize χ^2 with respect to the sample size. A statistically relevant compositional segregation is indicated by Pearson coefficients tending towards 1.00 [92, 96, 135], while 0 indicates a uniform distribution of elements [96].

Pearson coefficient evolution for the Li component versus the lithiation states and the average composition of Li are summarized in Figures 6.11 (a, b). A low Pearson coefficient of 0.125 is observed for the fully delithiated phase

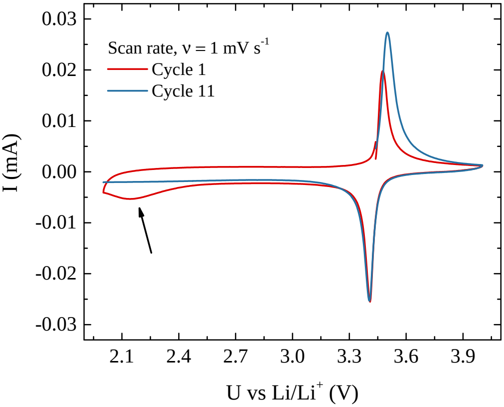

Figure 6.12: CV curves of a 150 nm LFP thin film. The 1st and 11th cycles are shown. The black arrow in the figure refers to the existence of uninterested phases before cycling.

(1.12 %). A Pearson coefficient value <0.10 indicates a uniform distribution [92, 96, 135]. Low Pearson coefficient values for fully de-/lithiated phases are expected indicating a homogeneous distribution of Li. On the other hand, high values indicate phase separation [33]. Even though inactive LFP regions are present in the fully delithiated phase, its Pearson coefficient is close to 0.100 which indicates a homogeneous background of Li and must be smaller than the box size (150 atom per box). The radial model could identify the inactive regions, but it showed some shortcomings in locating them practically. Otherwise, our APT results have confirmed the single phase nature of LFP at low Li concentration and microscopically located the inactive regions. On the other hand, microscopic result wasn't clear as it was expected.

With further lithium intercalation (>1.12 %), the Pearson coefficient for Li element does increase (see Figure 6.11). A relevant compositional segregation is indicated and heterogeneous Li distributions are formed. As the lithiation further proceeds, Li ions are being transported into the material resulting in an increase of the lithiated phase fraction. As a result of the evolution towards a heterogeneous microstructure, a systematic increase of the Pearson coefficient is noticed (see Figure 6.11). At the final end in the fully lithiated

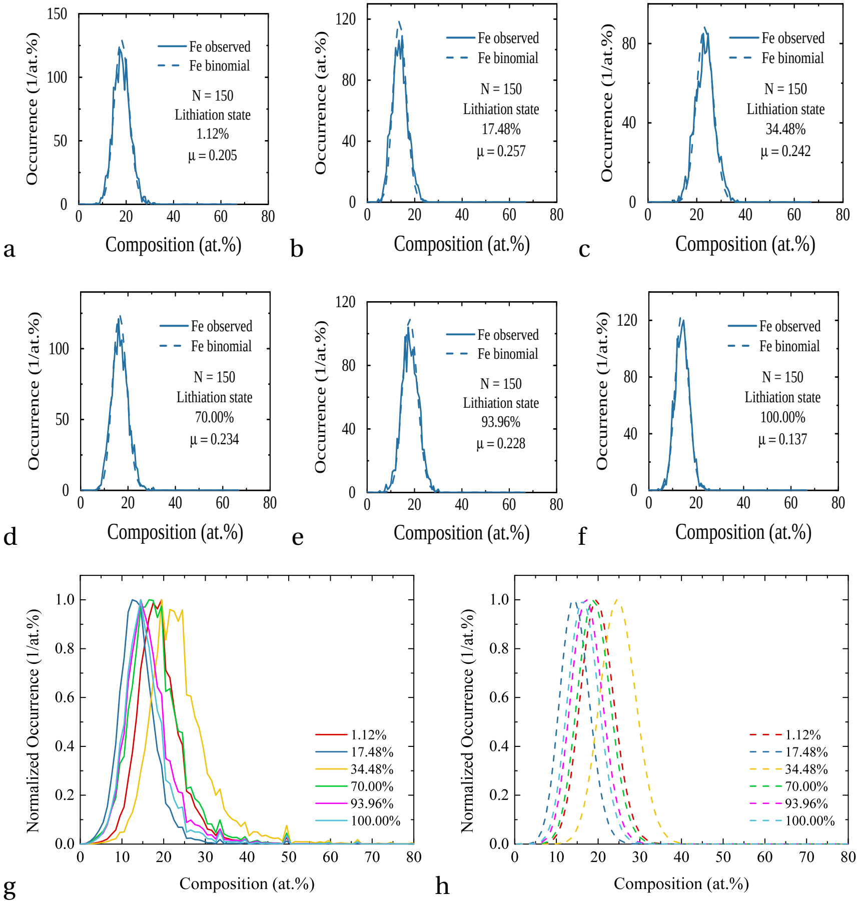

Figure 6.13: Statistical analyses of the Fe distribution at different lithiation states. Observed frequency distributions (solid line) in comparison to their binomial distributions (dashed line) with corresponding Pearson coefficients. (a-f) represent lithiation states 1.12 %, 17.48 %, 34.48 %, 70.00%, 93.96 %, and 100.00 %, respectively. (g, h) Normalized frequencies for observed and binomial distributions of Fe at different lithiation states, respectively.

phase (100 %), the Pearson coefficient decreases again to 0.382. Even though the Pearson coefficient has decreased, it still shows a higher value than what is expected for the single phase (<0.1). This discrepancy might be attributed to the existence of some foreign phases like $Li_3Fe_2(PO_4)_3$ [15]. Presence of such phases is reflected by a high Pearson coefficient. To figure out such uncommon phases, the electrochemistry was checked in the voltage window from 2.00 to 4.00 V (see Figure 6.12). The 1st and 11th cycles are compared to each other. The first cycle shows a lithiation peak at 2.15 V confirming the existence of other phases. This peak disappears after some cycles.

The normalized frequency for both the observed and the ideal binomial distributions were plotted in Figures 6.10 (g, h). Li concentrations increase in a systematic way with the lithiation state. Moreover, phase separation at intermediate concentrations is readable from the broadening of the peaks. The FWHM of the observed curves are increased with lithiation indicating heterogeneity or phase separation.

Opposite to the lithium component, iron shows a stable behavior over the whole de-/lithiation range. Figure 6.13 shows the observed frequency distributions as compared to the binomial distributions at different lithiation states. Almost unchanged Pearson coefficients for the stationary element Fe are explored (see Figure 6.14). Fe thereby tends to be unaffected during the de-/lithiation processes. FWHMs in Figures 6.13 (g, h) can in a normalized way represent the element composition and its heterogeneity through the samples. Some iron composition scattering has been detected which possibly happened during the sputtering process.

Figure 6.15 shows the observed frequency distributions for phosphorous as compared to the binomial distributions at different lithiation states. Sharp frequency distributions over the whole de-/lithiation range are observed which confirm the non heterogeneity of phosphorous during the de-/lithiation process. Figures 6.16 (a, b) summarize the Pearson coefficient values as a function of the lithiation states and phosphorous compositions. Phosphorous has an almost unchanged Pearson value. Again like Fe, P redistribution is inactive during de-/lithiation processes. Compositions, on the other hand, have nearly consistent values (see Figures 6.15 (g, h)).

Figure 6.17 shows the observed frequency distributions for oxygen as compared to the binomial distributions at different lithiation states. Like iron

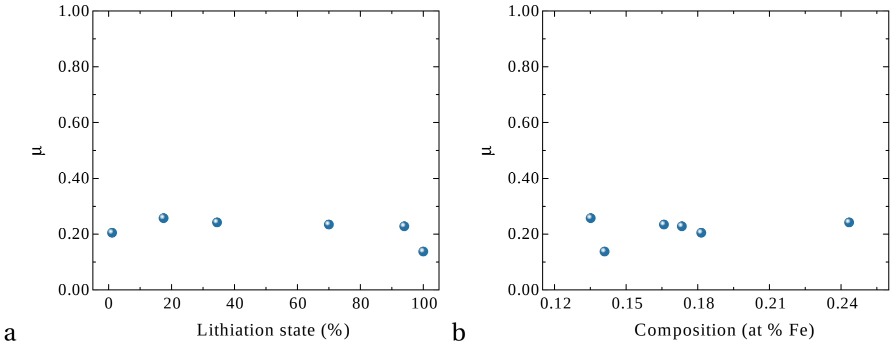

Figure 6.14: (a) and (b) Pearson coefficients of the Fe distribution in dis/charged LFP versus the lithiation states and Fe concentration measured by APT, respectively.

and phosphorous, oxygen doesn't display a decomposition over the whole de-/lithiation range. Figures 6.18 (a, b) summarize the Pearson coefficient values as a function of the lithiation states and phosphorous compositions. Pearson coefficients have virtually no change. Opposite to the well known deficiency in APT, oxygen has achieved in this work good stoichiometric ratios (see Figures 6.17 (g, h)).

Lastly, Li analysis can statistically represent the two phase intercalation reaction of LFP, although it had some drawbacks. Fe/P/O analyses prove the suitable linkages between them. As a result of their unchanged Pearson coefficients, this analysis can partially draw the great crystal stability of LFP. Strong covalent bonds between oxygen and P^{5+} ions. Thus, oxygen atoms are hard to be extracted. The antibonding Fe^{3+}/Fe^{2+} state is also stabilized as a result of its strong covalency.

In general, this is the first study to our knowledge to investigate the capabilities of APT in investigating Li interclation in LFP at different dis/charge states. Our results provide compelling evidence to statistically understand the local microstructural evolution in battery materials which centered a great perceptivity of batteries progression. On the other hand, serious limitations are

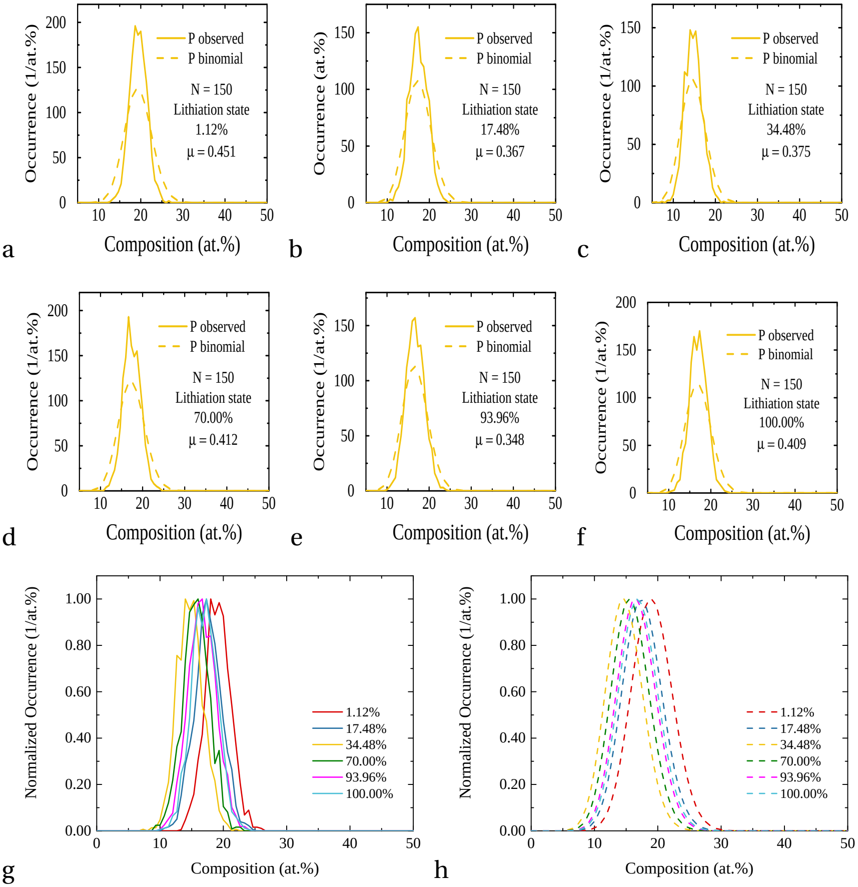

Figure 6.15: Statistical analyses of the P distribution at different lithiation states. Observed frequency distributions (solid line) in comparison to their binomial distributions (dashed line) with corresponding Pearson coefficients. (a-f) represent lithiation states 1.12 %, 17.48 %, 34.48 %, 70.00%, 93.96 %, and 100.00 %, respectively. (g, h) Normalized frequencies for observed and binomial distributions of P at different lithiation states, respectively.

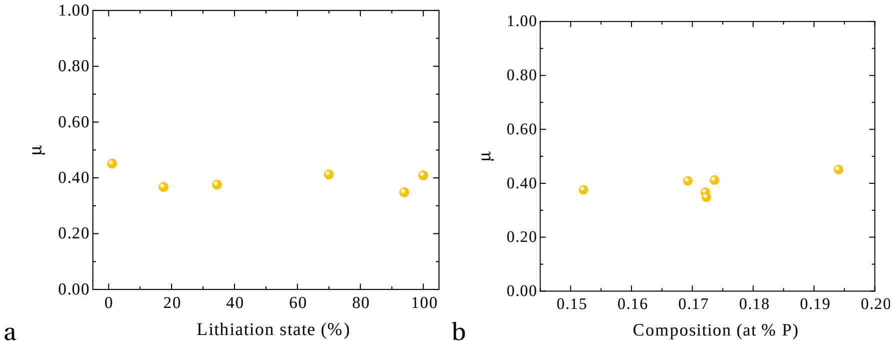

Figure 6.16: (a) and (b) Pearson coefficients of the P distribution in dis/charged LFP versus the lithiation states and P concentration measured by APT, respectively.

worth nothing. APT has showed some constraints to microscopically differentiate between the two phases. Li atoms suffer from some migrations during the measurements, even though they were performed at cryo-temperature. Contrastingly, low temperatures effect materials to fracture.

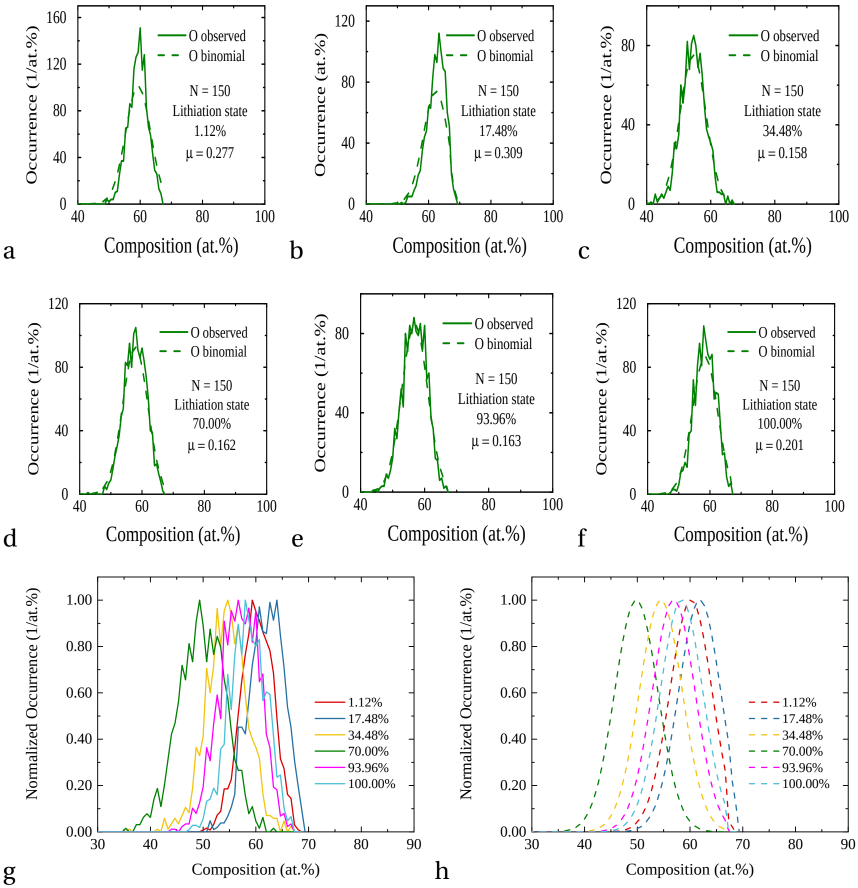

Figure 6.17: Statistical analyses of the O distribution at different lithiation states. Observed frequency distributions (solid line) in comparison to their binomial distributions (dashed line) with corresponding Pearson coefficients. (a-f) represent lithiation states 1.12 %, 17.48 %, 34.48 %, 70.00%, 93.96 %, and 100.00 %, respectively. (g) and (h) Normalized frequencies for observed and binomial distributions of O at different lithiation states, respectively.

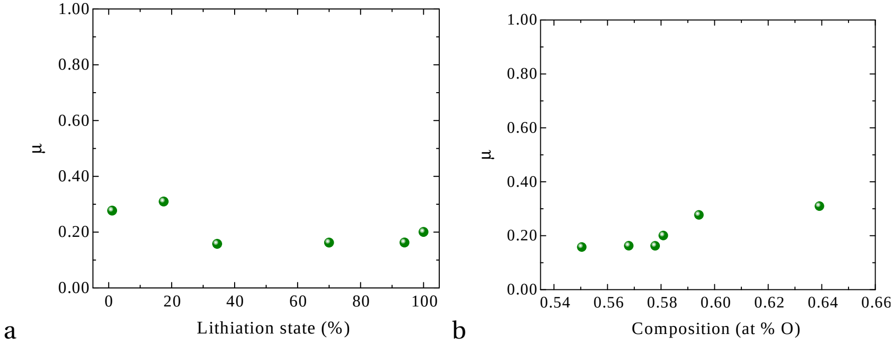

Figure 6.18: (a) and (b) Pearson coefficients of the O distribution in dis/charged LFP versus the lithiation states and O concentration measured by APT, respectively.

7 Summary

Lithium-Ion batteries (LIB) are a critical source of power in several everyday products such as laptops, cell phones, power tools, and even vehicles. The strategic importance of Li-ion batteries is massive and steadily on the rise. The possibilities of applying atom probe tomography (APT) to the atomic-scale structure of lithium iron phosphate (LFP) were explored. Local microscopic analyses of the atomic transport in amorphous, crystalline, and de-/lithiated LFP phases are studied. Prior works have documented indirect interpretations of electrochemical measurements for battery materials. However, these studies have either been short-term studies of the ionic transport on a microscopic or on the atomic scale. In this study, 3D microstructure of LFP was demonstrated by APT in a sub-nanometer spatial resolution. High quality thin films/tips were produced by ion beam sputtering. X-ray diffraction (XRD) and Transmission Electron Microscope (TEM) were used to observe the thin films structural, while electrochemical characterizations were obtained by means of Cyclic Voltammetry (CV).

The material produced for this study had excellent structural stability and cycling reversibility. Over 7000 cycles with retention > 92 % have been achieved. Moreover, details of the Li transport were documented by electrochemical measurements. Currents show a linear to parabolic transition with accelerating the scan rate and surprisingly increase with increasing the layer thickness. Overpotential, on the other hand, opposite to what was expected shows no dependence on the layer thickness. Less electrical driving force is required to force the same current in thick films. It is indicated that grain boundaries represent an electroactive interface at which the overpotential appears. And hence, the grain boundaries work as short circuits (fast conduction paths) for faster Li ions diffusion.

$LiFePO_4$ (LFP) is then 3 dimensionally studied by APT. Systematic quantitative investigations of the amorphous LFP by APT were discussed. The transition metal element (Fe) clearly fits the post-ionization theorem described by Kingham. Stoichiometric ratios relative to all elements (Li+Fe+P+O) and to the stable element (Fe) were calculated. P and O reveal a reverse relationship against the laser power and a direct relation with the field strength. Li ions, on the other hand, in response to the applied fields, undoubtedly redistribute. As a consequence of the its migration during the measurements, Li increases with the laser power and decreases with the field strength.

Enrichment/depletion regions as a result of Li migrations during APT measurements are created. A new idiom -Li shooting- is addressed to describe this drift. Li gradients towards the tip front relative to the applied laser power are seen in amorphous phase, whereas the crystalline phase isn't affected. Moreover, the remaining host elements, Fe, P, and O, remain homogeneously distributed in both phases. The diffusion at cryogenic temperatures of the APT measurements is evaluated using a mathematical model. It is shown that the diffusivity in amorphous structure is orders of magnitude faster than that of the crystalline state at a temperature of 60 K.

Most notably, this is the first study to our knowledge to investigate the capabilities of APT in LFP at different de-/lithiation states. Our results provide a guidance to statistically understand the local microstructure evolution in battery materials. Inactive LFP regions in the fully delithiated phase (FP) were, for the first time, experimentally highlighted. On the other hand, serious limitations are worth nothing. APT was unable to microscopy differentiate between the two phases. Although APT measurements were performed at cryo-temperature, Li showed a displacement during measurements. Contrastingly, most materials are early fractured at ultra low temperatures. This study therefore provides some insights toward the atomic-scale mechanism of capacity degradation as a function of cycling, and assist to create Li materials with prolonged lifetimes. Future work should therefore explore follow up work on conversion battery materials.

Bibliography

[1] Michael D. Slater, Donghan Kim, Eungje Lee, and Christopher S. Johnson. Sodium-ion batteries. *Advanced Functional Materials*, 23(8):947–958, feb 2013.

[2] Bing Li, Fang Dai, Qiangfeng Xiao, Li Yang, Jingmei Shen, Cunman Zhang, and Mei Cai. Activated Carbon from Biomass Transfer for High-Energy Density Lithium-Ion Supercapacitors. *Advanced Energy Materials*, 6(18), sep 2016.

[3] Eric C Evarts. To the limits of lithium. *Nature*, 526:S93–S95, 2015.

[4] Chaofeng Liu, Zachary G. Neale, and Guozhong Cao. Understanding electrochemical potentials of cathode materials in rechargeable batteries. *Materials Today*, 19(2):109–123, 2016.

[5] J. M. Tarascon and M. Armand. Issues and challenges facing rechargeable lithium batteries. 414(6861):359–367, nov 2001.

[6] Jason R. Croy, Ali Abouimrane, and Zhengcheng Zhang. Next-generation lithium-ion batteries: The promise of near-term advancements. *MRS Bulletin*, 39(5):407–415, 2014.

[7] Yuping Wu. *Lithium-ion batteries: Fundamentals and Applications*, volume 4. CRC Press, 2015.

[8] Emrullah KARGIN. DESIGN AND TEST OF AN ALL-SOLID-STATE Li-ion BATTERY. (November), 2016.

[9] Christian; Julien, Alain; Mauger, Ashok; Vijh, and Karim Zaghib. *[textbook] Lithium Batteries.* Springer International Publishing, Oct 2016.

[10] Xiaoyu Zhang, Martijn Van Hulzen, Deepak P. Singh, Alex Brownrigg, Jonathan P. Wright, Niels H. Van Dijk, and Marnix Wagemaker. Direct view on the phase evolution in individual Li_xFePO_4 nanoparticles during Li-ion battery cycling. *Nature Communications*, 6(May):1–7, 2015.

[11] Xiaodong Xu, Sanghan Lee, Sookyung Jeong, Youngsik Kim, and Jaephil Cho. Recent progress on nanostructured 4v cathode materials for Li-ion batteries for mobile electronics. *Materials Today*, 16(12):487 – 495, 2013.

[12] Mehul Oswal, Jason Paul, and Runhua Zhao. A comparative study of lithium-ion batteries. *USA: University of Southen California*, 2010.

[13] CÃ©line, Loic Dupont, Kun Tang, Hong Li, X.J. Huang, and Emmanuel Baudrin. Structural and textural characterization of $LiFePO_4$ thin films prepared by pulsed laser deposition on si substrates. 518:5447–5451, 07 2010.

[14] Mathias Köhler, Frank Berkemeier, Tobias Gallasch, and Guido Schmitz. Lithium diffusion in sputter-deposited lithium iron phosphate thin-films. *Journal of Power Sources*, 236:61–67, 2013.

[15] A. K. Padhi, K. S. Nanjundaswamy, and J. B. Goodenough. Phospho-olivines as Positive-Electrode Materials for Rechargeable Lithium Batteries. *Journal of The Electrochemical Society*, 144(4):1188, 1997.

[16] Zhihua Li, Duanming Zhang, and Fengxia Yang. Developments of lithium-ion batteries and challenges of $LiFePO_4$ as one promising cathode material. *Journal of Materials Science*, 44(10):2435–2443, 2009.

[17] Aiko Bünting, Sven Uhlenbruck, Doris Sebold, H. P. Buchkremer, and R. Vaßen. Three-Dimensional, Fibrous Lithium Iron Phosphate Structures Deposited by Magnetron Sputtering. *ACS Applied Materials and Interfaces*, 7(40):22594–22600, oct 2015.

[18] A. Devaraj, M. Gu, R. Colby, P. Yan, C. M. Wang, J. M. Zheng, J. Xiao, A. Genc, J. G. Zhang, I. Belharouak, D. Wang, K. Amine, and S. Thevuthasan. Visualizing nanoscale 3D compositional fluctuation of lithium in advanced lithium-ion battery cathodes. *Nature Communications*, 6(August), 2015.

[19] Johannes Maier, Björn Pfeiffer, Cynthia A Volkert, and Carsten Nowak. Three-dimensional microstructural characterization of lithium manganese oxide with atom probe tomography. *Energy Technology*, 4(12):1565–1574, 2016.

[20] David A. Muller. Structure and bonding at the atomic scale by scanning transmission electron microscopy. 8(4):263–270, 2009.

[21] Baptiste Gault, Michael P. Moody, Julie M. Cairney, and Simon P. Ringer. Atom probe crystallography. *Materials Today*, 15(9):378–386, 2012.

[22] Michael K. Miller and Richard G. Forbes. *Atom-probe tomography: The local electrode atom probe*, volume 9781489974. 2014.

[23] M. Drechsler. Erwin Müller and the early development of field emission microscopy. *Surface Science*, 70(1):1–18, jan 1978.

[24] Mohammed Reda Chellali, Zoltan Balogh, Houari Bouchikhaoui, Ralf Schlesiger, Patrick Stender, Lei Zheng, and Guido Schmitz. Triple junction transport and the impact of grain boundary width in nanocrystalline Cu. *Nano Letters*, 12(7):3448–3454, 2012.

[25] Andreas Stoffers, Christian Oberdorfer, and Guido Schmitz. Controlled field evaporation of fluorinated self-assembled monolayers. *Langmuir*, 28(1):56–59, 2012.

[26] Alfred Cerezo, Peter H. Clifton, Mark J. Galtrey, Colin J. Humphreys, Thomas F. Kelly, David J. Larson, Sergio Lozano-Perez, Emmanuelle A. Marquis, Rachel A. Oliver, Gang Sha, Keith Thompson, Mathijs Zandbergen, and Roger L. Alvis. Atom probe tomography today. 10(12):36–42, dec 2007.

[27] Günter Möbus and Beverley J. Inkson. Nanoscale tomography in materials science. 10(12):18–25, dec 2007.

[28] Thomas Maxisch and Gerband Ceder. Elastic properties of olivine $LiFePO_4$ from first principles. *Phys. Rev. B*, 73:174112, May 2006.

[29] Jianjun Yang and John S. Tse. Li ion diffusion mechanisms in Li_xFePO_4: An ab initio molecular dynamics study. *Journal of Physical Chemistry A*, 115(45):13045–13049, nov 2011.

[30] Dong-Han Kim and Jaekook Kim. Synthesis of $LiFePO_4$ nanoparticles in polyol medium and their electrochemical properties. *Electrochemical and Solid State Letters*, 9(9):A439, 2006.

[31] Nan Ji Yun, Hyung-Wook Ha, Kyung Hee Jeong, Heon-Yong Park, and Keon Kim. Synthesis and electrochemical properties of olivine-type $LiFePO_4/c$ composite cathode material prepared from a poly (vinyl alcohol)-containing precursor. *Journal of power sources*, 160(2):1361–1368, 2006.

[32] Juliane Greta Mürter. Chair of Materials Physics Production and Characterization of $LiMn_2O_4$ thin film battery electrodes Master thesis submitted by. (April), 2016.

[33] De Li and Haoshen Zhou. Two-phase transition of Li-intercalation compounds in Li-ion batteries. *Materials Today*, 17(9):451–463, 2014.

[34] A. Van der Ven, K. Garikipati, S. Kim, and M. Wagemaker. The Role of Coherency Strains on Phase Stability in Li[sub x]FePO[sub 4]: Needle Crystallites Minimize Coherency Strain and Overpotential. *Journal of The Electrochemical Society*, 156(11):A949, 2009.

[35] Zhigao Yang, Yu Dai, Shengping Wang, and Jingxian Yu. How to make lithium iron phosphate better: a review exploring classical modification approaches in-depth and proposing future optimization methods. *Journal of Materials Chemistry A*, 4(47):18210–18222, 2016.

[36] Anton Van Der Ven, Jishnu Bhattacharya, and Anna A. Belak. Understanding Li diffusion in Li-intercalation compounds. *Accounts of Chemical Research*, 46(5):1216–1225, may 2013.

[37] A. Van der Ven and M. Wagemaker. Effect of surface energies and nanoparticle size distribution on open circuit voltage of Li-electrodes. *Electrochemistry Communications*, 11(4):881–884, apr 2009.

[38] Man Huon Han, Elena Gonzalo, Gurpreet Singh, and Teofilo Rojo. A comprehensive review of sodium layered oxides: powerful cathodes for na-ion batteries. *Energy Environ. Sci.*, 8:81–102, 2015.

[39] M Stanley Whittingham. Lithium batteries and cathode materials. *Chemical reviews*, 104(10):4271–4302, 2004.

[40] C Delacourt, L Laffont, R Bouchet, C Wurm, J-B Leriche, M Morcrette, J-M Tarascon, and C Masquelier. Toward understanding of electrical limitations (electronic, ionic) in limpo$_4$ (m= fe, mn) electrode materials. *Journal of the Electrochemical Society*, 152(5):A913, 2005.

[41] Atsuo Yamada, Hisroshi Koizumi, Shin Ichi Nishimura, Noriyuki Sonoyama, Ryoji Kanno, Masao Yonemura, Tatsuya Nakamura, and Y. O. Kobayashi. Room-temperature miscibility gap in Li_xFePO_4. *Nature Materials*, 5(5):357–360, may 2006.

[42] Guoying Chen, Xiangyun Song, and Thomas J. Richardson. Electron microscopy study of the Li_xFePO_4 to $FePO_4$ phase transition. *Electrochemical and Solid-State Letters*, 9(6):A295, jun 2006.

[43] Zhaohui Chen, Zhonghua Lu, and JR Dahn. Staging phase transitions in $li_x coo_2$. *Journal of the Electrochemical Society*, 149(12):A1604, 2002.

[44] Shin Ichi Nishimura, Genki Kobayashi, Kenji Ohoyama, Ryoji Kanno, Masatomo Yashima, and Atsuo Yamada. Experimental visualization of lithium diffusion in Li_xFePO_4. *Nature Materials*, 7(9):707–711, aug 2008.

[45] C. Delmas, M. Maccario, L. Croguennec, F. Le Cras, and F. Weill. Lithium deintercalation in $LiFePO_4$ nanoparticles via a domino-cascade model. *Nature Materials*, 7(8):665–671, 2008.

[46] M. Saiful Islam, Daniel J. Driscoll, Craig A.J. Fisher, and Peter R. Slater. Atomic-scale investigation of defects, dopants, and lithium transport in the $LiFePO_4$ olivine-type battery material. *Chemistry of Materials*, 17(20):5085–5092, oct 2005.

[47] D Morgan, A Van Der Ven, and G Ceder. Li Conductivity in Li_xMPO_4 (M = Mn, Fe, Co, Ni) Olivine Materials. *Electrochemical and Solid-State Letters*, 7(2):A30, 2003.

[48] Gopi Krishna Phani Dathar, Daniel Sheppard, Keith J. Stevenson, and Graeme Henkelman. Calculations of Li-ion diffusion in olivine phosphates. *Chemistry of Materials*, 23(17):4032–4037, sep 2011.

[49] Byoungwoo Kang and Gerbrand Ceder. Battery materials for ultrafast charging and discharging. *Nature*, 458(7235):190–193, 2009.

[50] Venkat Srinivasan and John Newman. Discharge model for the lithium iron-phosphate electrode. *Journal of the Electrochemical Society*, 151(10):A1517, 2004.

[51] AS Andersson and John Oswald Thomas. The source of first-cycle capacity loss in lifepo$_4$. *Journal of Power Sources*, 97:498–502, 2001.

[52] Cheng Kai ChiuHuang and Hsiao Ying Shadow Huang. A diffusion model in a two-phase interfacial zone for nanoscale lithium-ion battery materials. In *ASME International Mechanical Engineering Congress and Exposition, Proceedings (IMECE)*, volume 6, pages 1231–1237, 2012.

[53] Wolfgang Dreyer, Janko Jamnik, Clemens Guhlke, Robert Huth, Jože Moškon, and Miran Gaberšček. The thermodynamic origin of hysteresis in insertion batteries. *Nature Materials*, 9(5):448–453, apr 2010.

[54] M Stanley Whittingham. Ultimate limits to intercalation reactions for lithium batteries. *Chemical reviews*, 114(23):11414–11443, 2014.

[55] Fredrick Omenya, Natasha A Chernova, Ruibo Zhang, Jin Fang, Yiqing Huang, Fred Cohen, Nathaniel Dobrzynski, Sanjaya Senanayake, Wenqian Xu, and M Stanley Whittingham. Why substitution enhances the reactivity of $LiFePO_4$. *Chemistry of Materials*, 25(1):85–89, 2013.

[56] Fredrick Omenya, Natasha A Chernova, Qi Wang, Ruibo Zhang, and M Stanley Whittingham. The structural and electrochemical impact of li and fe site substitution in $LiFePO_4$. *Chemistry of Materials*, 25(13):2691–2699, 2013.

[57] G. Brunetti, D. Robert, P. Bayle-Guillemaud, J. L. Rouvière, E. F. Rauch, J. F. Martin, J. F. Colin, F. Bertin, and C. Cayron. Confirmation of the domino-cascade model by $LiFePO_4/FePO_4$ precession electron diffraction. *Chemistry of Materials*, 23(20):4515–4524, oct 2011.

[58] L. Laffont, C. Delacourt, P. Gibot, M. Yue Wu, P. Kooyman, C. Masquelier, and J. Marie Tarascon. Study of the $LiFePO_4/FePO_4$two-phase system by high-resolution electron energy loss spectroscopy. *Chemistry of Materials*, 18(23):5520–5529, nov 2006.

[59] C. V. Ramana, A. Mauger, F. Gendron, C. M. Julien, and K. Zaghib. Study of the Li-insertion/extraction process in $LiFePO_4/FePO_4$. *Journal of Power Sources*, 187(2):555–564, feb 2009.

[60] Hui Wu and Yi Cui. Designing nanostructured si anodes for high energy lithium ion batteries. *Nano today*, 7(5):414–429, 2012.

[61] MN Obrovac and VL Chevrier. Alloy negative electrodes for Li-ion batteries. *Chemical reviews*, 114(23):11444–11502, 2014.

[62] M Zhang, T Wang, and G Cao. Promises and challenges of tin-based compounds as anode materials for lithium-ion batteries. *International Materials Reviews*, 60(6):330–352, 2015.

[63] Subrahmanyam Goriparti, Ermanno Miele, Francesco De Angelis, Enzo Di Fabrizio, Remo Proietti Zaccaria, and Claudio Capiglia. Review on recent progress of nanostructured anode materials for Li-ion batteries. *Journal of power sources*, 257:421–443, 2014.

[64] Qifeng Zhang, Evan Uchaker, Stephanie L Candelaria, and Guozhong Cao. Nanomaterials for energy conversion and storage. *Chemical Society Reviews*, 42(7):3127–3171, 2013.

[65] Antonino Salvatore Arico, Peter Bruce, Bruno Scrosati, Jean-Marie Tarascon, and Walter Van Schalkwijk. Nanostructured materials for advanced energy conversion and storage devices. In *Materials for sustainable energy: a collection of peer-reviewed research and review articles from Nature Publishing Group*, pages 148–159. World Scientific, 2011.

[66] B. D. Cullity and John W. Weymouth. Elements of X-Ray Diffraction. *American Journal of Physics*, 25(6):394–395, sep 1957.

[67] Bertram Eugene Warren. *X-ray Diffraction*. 1990.

[68] AL Patterson. The scherrer formula for x-ray particle size determination. *Physical review*, 56(10):978, 1939.

[69] Georg Haberfehlner. 3d nanoimaging of semiconductor devices and materials by electron tomography. 09 2013.

[70] David B Williams and C Barry Carter. The transmission electron microscope. In *Transmission electron microscopy*, pages 3–17. Springer, 1996.

[71] Baptiste Gault, Michael P. Moody, Julie M. Cairney, and Simon P. Ringer. Field Ion Microscopy. pages 9–28. 2012.

[72] Baptiste Gault, Michael P. Moody, Julie M. Cairney, and Simon P. Ringer. From Field Desorption Microscopy to Atom Probe Tomography. pages 29–68. 2012.

[73] Erwin W. Müller. Field desorption. *Physical Review*, 102(3):618–624, may 1956.

[74] Robert Gomer. Field desorption. *The Journal of Chemical Physics*, 31(2):341–345, aug 1959.

[75] M. K. Miller and R. G. Forbes. Atom probe tomography. *Materials Characterization*, 60(6):461–469, 2009.

[76] C A Volkert and A M Minor. Focused ion beam microscopy and micromachining. 32(5):389–395, 2007.

[77] Erwin W. Müller, John A. Panitz, and S. Brooks McLane. The atom-probe field ion microscope. *Review of Scientific Instruments*, 39(1):83–86, jan 1968.

[78] Tien T. Tsong. *Atom-Probe Field Ion Microscopy*. Cambridge University Press, aug 1990.

[79] M. Pichaud, A. Müller, and M. Drechsler. Temperature distribution along metal tips. (For field emission microscopy and the study of surface phenomena). *Surface Science*, 26(1):14–20, 1971.

[80] C M C de Castilho and D R Kingham. Resolution of the field ion microscope. *Journal of Physics D: Applied Physics*, 20(1):116–124, jan 1987.

[81] Baptiste Gault, Michael P. Moody, Julie M. Cairney, and Simon P. Ringer. Introduction. pages 3–7. 2012.

[82] Lei Zhang. Structural analysis of polyelectrolyte - multilayer system with atom probe tomography, 2016.

[83] P. Bas, A. Bostel, B. Deconihout, and D. Blavette. A general protocol for the reconstruction of 3D atom probe data. *Applied Surface Science*, 87-88(C):298–304, mar 1995.

[84] Baptiste Gault, Michael P. Moody, Julie M. Cairney, and Simon P. Ringer. Tomographic Reconstruction. pages 157–209. 2012.

[85] J. M. Hyde, A. Cerezo, and T. J. Williams. Statistical analysis of atom probe data: Detecting the early stages of solute clustering and/or co-segregation. *Ultramicroscopy*, 109(5):502–509, apr 2009.

[86] Michael P. Moody, Leigh T. Stephenson, Anna V. Ceguerra, and Simon P. Ringer. Quantitative binomial distribution analyses of nanoscale like-solute atom clustering and segregation in atom probe tomography data. *Microscopy Research and Technique*, 71(7):542–550, jul 2008.

[87] Philipp Seeger. Atom Probe Tomography of AlBGaN Layers for Optoelectronic Devices, 2018.

[88] Tien T Tsong. *Atom-probe field ion microscopy: field ion emission, and surfaces and interfaces at atomic resolution.* Cambridge University Press, 2005.

[89] TJ Godfrey, MG Hetherington, JM Sassen, and GDW Smith. The characterization of spinodal structures in duplex cf3 steels. *Le Journal de Physique Colloques*, 49(C6):C6–421, 1988.

[90] I. Vurgaftman and J. R. Meyer. Band parameters for nitrogen-containing semiconductors. 94(6):3675–3696, sep 2003.

[91] Karl Pearson. *On the theory of contingency and its relation to association and normal correlation; On the general theory of skew correlation and non-linear regression.* Cambridge University Press, 1904.

[92] Michael P Moody, Leigh T Stephenson, Peter V Liddicoat, and Simon P Ringer. Contingency table techniques for three dimensional atom probe tomography. *Microscopy research and technique*, 70(3):258–268, 2007.

[93] B Gault, MP Moody, DW Saxey, JM Cairney, Z Liu, R Zheng, RKW Marceau, PV Liddicoat, LT Stephenson, and SP Ringer. Atom probe tomography at the university of sydney. In *Frontiers in Materials Research*, pages 187–216. Springer, 2008.

[94] Eric Camus and Christian Abromeit. Analysis of conventional and three-dimensional atom probe data for multiphase materials. *Journal of applied physics*, 75(5):2373–2382, 1994.

[95] Baptiste Gault, Michael P Moody, Julie M Cairney, and Simon P Ringer. *Atom probe microscopy*, volume 160. Springer Science & Business Media, 2012.

[96] Baptiste Gault, Michael P. Moody, Julie M. Cairney, and Simon P. Ringer. Analysis Techniques for Atom Probe Tomography. pages 213–297. 2012.

[97] Arun Devaraj, Tiffany C Kaspar, Sathvik Ramanan, S Walvekar, Mark E Bowden, V Shutthanandan, and Richard J Kurtz. Nanoscale phase separation in epitaxial cr-mo and cr-v alloy thin films studied using atom probe tomography: Comparison of experiments and simulation. *Journal of Applied Physics*, 116(19):193512, 2014.

[98] Bing Feng Ju, Yuan Liu Chen, Mingming Fu, Ye Chen, and Yunhai Yang. Systematic study of electropolishing technique for improving the quality and production reproducibility of tungsten STM probe. *Sensors and Actuators, A: Physical*, 155(1):136–144, oct 2009.

[99] G. Stephen Kelsey. The Anodic Oxidation of Tungsten in Aqueous Base. *Journal of The Electrochemical Society*, 124(6):814, 1977.

[100] Qiangxian Huang and Takeshi Hatsuzawa. A novel tapping-mode stylus with a polyvinylidene fluoride unimorph sensor. *Measurement Science and Technology*, 15(3):520, 2004.

[101] WX Sun, ZX Shen, FC Cheong, GY Yu, KY Lim, and JY Lin. Preparation of cantilevered w tips for atomic force microscopy and apertureless near-field scanning optical microscopy. *Review of scientific instruments*, 73(8):2942–2947, 2002.

[102] Yoshiaki Nakamura, Yutaka Mera, and Koji Maeda. A reproducible method to fabricate atomically sharp tips for scanning tunneling microscopy. *Review of Scientific Instruments*, 70(8):3373–3376, 1999.

[103] Inger Ekvall, Erik Wahlström, Dan Claesson, Håkan Olin, and Eva Olsson. Preparation and characterization of electrochemically etched w tips for stm. *Measurement Science and Technology*, 10(1):11, 1999.

[104] Donald M Mattox. *Handbook of physical vapor deposition (PVD) processing*. William Andrew, 2010.

[105] Susann Nowak, Frank Berkemeier, and Guido Schmitz. Ultra-thin LiPON films - Fundamental properties and application in solid state thin film model batteries. *Journal of Power Sources*, 275:144–150, 2015.

[106] L. M. Sender, I. Escapa, A. Benedetti, R. Cúneo, and J. B. Diez. Exploring the interior of cuticles and compressions of fossil plants by FIB-SEM milling and image microscopy. *Journal of Microscopy*, 269(1):48–58, jan 2018.

[107] A. Bünting, S. Uhlenbruck, C. Dellen, M. Finsterbusch, C. L. Tsai, D. Sebold, H. P. Buchkremer, and R. Vaßen. Influence of titanium nitride interlayer on the morphology, structure and electrochemical performance of magnetron-sputtered lithium iron phosphate thin films. *Journal of Power Sources*, 281:326–333, may 2015.

[108] C. Legrand, L. Dupont, C. Davoisne, F. Le Marrec, J. Perrire, and E. Baudrin. Unexpected formation by pulsed laser deposition of nanostructured Fe/olivine thin films on MgO substrates. *Journal of Solid State Chemistry*, 184(2):351–356, feb 2011.

[109] DP Chen, A Maljuk, and CT Lin. Floating zone growth of lithium iron (ii) phosphate single crystals. *Journal of crystal growth*, 284(1-2):86–90, 2005.

[110] V Palomares, I Ruiz de Larramendi, J Alonso, M Bengoechea, A Goni, O Miguel, and T Rojo. $LiFePO_4$ thin films grown by pulsed laser deposition: Effect of the substrate on the film structure and morphology. *Applied surface science*, 256(8):2563–2568, 2010.

[111] Kun Tang, Jinpeng Sun, Xiqian Yu, Hong Li, and Xuejie Huang. Electrochemical performance of $LiFePO_4$ thin films with different morphology and crystallinity. *Electrochimica Acta*, 54(26):6565–6569, 2009.

[112] K-F Chiu. Optimization of synthesis process for carbon-mixed $LiFePO_4$ composite thin-film cathodes deposited by bias sputtering. *Journal of the Electrochemical Society*, 154(2):A129, 2006.

[113] Juliane Mürter, Susann Nowak, Efi Hadjixenophontos, Yug Joshi, and Guido Schmitz. Grain boundary transport in sputter-deposited nanometric thin films of lithium manganese oxide. *Nano Energy*, 43(October 2017):340–350, 2018.

[114] Fabian Wunde, Susann Nowak, Juliane Mürter, Efi Hadjixenophontos, Frank Berkemeier, and Guido Schmitz. Ion transport and phase transformation in thin film intercalation electrodes. *International Journal of Materials Research*, 108(11):984–998, 2017.

[115] YZ Dong, YM Zhao, and H Duan. Crystal structure and lithium electrochemical extraction properties of olivine type $LiFePO_4$. *Materials Chemistry and Physics*, 129(3):756–760, 2011.

[116] Joshua P Pender, Gaurav Jha, Duck Hyun Youn, Joshua M Ziegler, Ilektra Andoni, Eric J Choi, Adam Heller, Bruce S Dunn, Paul S Weiss, Reginald M Penner, et al. Electrode degradation in lithium-ion batteries. *ACS nano*, 14(2):1243–1295, 2020.

[117] Koichi Aoki, Koichi Tokuda, and Hiroaki Matsuda. Theory of linear sweep voltammetry with finite diffusion space: Part ii. totally irreversible and quasi-reversible cases. *Journal of Electroanalytical Chemistry and Interfacial Electrochemistry*, 160(1):33–45, 1984.

[118] J E B Randles. A cathode ray polarograph.The current-voltage curves. *Transactions of the Faraday Society*, 44:327–338, 1948.

[119] Zhen Quan, Shouya Ohguchi, Masayasu Kawase, Hiroshi Tanimura, and Noriyuki Sonoyama. Preparation of nanocrystalline limn2o4 thin film by electrodeposition method and its electrochemical performance for lithium battery. *Journal of Power Sources*, 244:375–381, 2013. 16th International Meeting on Lithium Batteries (IMLB).

[120] F J Hunt. A method for electropolishing tungsten filaments and baskets. *Journal of Physics E: Scientific Instruments*, 9(11):921, 1976.

[121] T. T. Tsong, T. J. Kinkus, and C. F. Ai. Field induced and surface catalyzed formation of novel ions: A pulsed-laser time-of-flight atom-probe study. *The Journal of Chemical Physics*, 78(7):4763–4775, apr 1983.

[122] Gerd Hendrik Greiwe, Zoltan Balogh, and Guido Schmitz. Atom probe tomography of lithium-doped network glasses. *Ultramicroscopy*, 141:51–55, 2014.

[123] Dhamodaran Santhanagopalan, Daniel K. Schreiber, Daniel E. Perea, Richard L. Martens, Yuri Janssen, Peter Khalifah, and Ying Shirley Meng. Effects of laser energy and wavelength on the analysis of $LiFePO_4$ using laser assisted atom probe tomography. *Ultramicroscopy*, 148:57–66, 2015.

[124] K. Hono, T. Ohkubo, Y.M. Chen, M. Kodzuka, K. Oh-ishi, H. Sepehri-Amin, F. Li, T. Kinno, S. Tomiya, and Y. Kanitani. Broadening the applications of the atom probe technique by ultraviolet femtosecond laser. *Ultramicroscopy*, 111(6):576–583, may 2011.

[125] T. Kinno, M. Tomita, T. Ohkubo, S. Takeno, and K. Hono. Laser-assisted atom probe tomography of 18 O-enriched oxide thin film for quantitative analysis of oxygen. *Applied Surface Science*, 290:194–198, jan 2014.

[126] M. Bachhav, R. Danoix, F. Danoix, B. Hannoyer, S. Ogale, and F. Vurpillot. Investigation of wustite ($Fe_{1-x}O$) by femtosecond laser assisted atom probe tomography. *Ultramicroscopy*, 111(6):584–588, 2011.

[127] A. Devaraj, R. Colby, W. P. Hess, D. E. Perea, and S. Thevuthasan. Role of photoexcitation and field ionization in the measurement of accurate oxide stoichiometry by laser-assisted atom probe tomography. *Journal of Physical Chemistry Letters*, 4(6):993–998, 2013.

[128] Yi Zhang and Andrew C. Hillier. Three-dimensional atom probe tomography of oxide, anion, and alkanethiolate coatings on gold. *Analytical Chemistry*, 82(14):6139–6147, jul 2010.

[129] A Cerezo, PH Clifton, A Gomberg, and GDW Smith. Aspects of the performance of a femtosecond laser-pulsed 3-dimensional atom probe. *Ultramicroscopy*, 107(9):720–725, 2007.

[130] Joseph H Bunton, Jesse D Olson, Daniel R Lenz, and Thomas F Kelly. Advances in pulsed-laser atom probe: Instrument and specimen design for optimum performance. *Microscopy and Microanalysis*, 13(6):418, 2007.

[131] Roger Haydock and David R. Kingham. Some predictions of a theory of post-ionization of field-evaporated ions. *Surface Science Letters*, 104(1):L194–L198, mar 1981.

[132] Inspico, high resolution analysis - tools, url= http://inspico.de/software/tools/.

[133] Rita Kirchhofer, Melissa C Teague, and Brian P Gorman. Thermal effects on mass and spatial resolution during laser pulse atom probe tomography of cerium oxide. *Journal of nuclear materials*, 436(1-3):23–28, 2013.

[134] R. Kirchheim. Solubility, diffusivity and trapping of hydrogen in dilute alloys. Deformed and amorphous metals II. *Acta Metallurgica*, 30(6):1069–1078, jun 1982.

[135] Arun Devaraj, Robert Colby, François Vurpillot, and Suntharampillai Thevuthasan. Understanding atom probe tomography of oxide-supported metal nanoparticles by correlation with atomic-resolution electron microscopy and field evaporation simulation. *Journal of Physical Chemistry Letters*, 5(8):1361–1367, 2014.

A Appendix

Table A.1: How to define Lithium Iron Phosphate peaks.

Suggested Ion/Molecule	m/z (a.m.u)	Probability (%)	Suggested Ion/Molecule	m/z (a.m.u)	Probability (%)
H^+	1.00	99.99	${HPO_2}^{+3}$	21.33	99.00
${H_2}^+$	2.00	99.99	LiO^+	23.00	92.28
C^{+2}	6.00	98.89	FeO^{+3}	23.33	5.84
Li^+	6.00	7.50	PO^{+2}	23.50	99.76
CH^{+2}	6.50	98.88	Ga^{+3}	23.67	39.89
Li^+	7.00	92.50	FeO^{+3}	24.00	91.53
O^{+2}	8.00	99.76	P_2O^{+3}	26.00	99.76
OH^{+2}	8.50	99.75	Cr^{+2}	26.00	83,79
H_2O^{+2}	9.00	99.75	${PO_3}^{+3}$	26.33	99.76
Li_2O^{+3}	9.33	7.48	Cr^{+2}	26.50	9,50
H_3O^{+2}	9.50	99.75	Fe^{+2}	27.00	5.85
Li_2O^{+3}	10.00	92.28	Mn^{+2}	27.50	100.00
P^{+3}	10.33	100.00	Fe^{+2}	28.00	91.75
${O_2}^{+3}$	10.67	99.76	Li_2O^+	28.00	7.48
${PH_2}^{+3}$	11.00	99.99	${FeO_2}^{+3}$	29.33	91.53
LiO^{+2}	11.50	92.28	Li_2O^+	30.00	92.28
C^+	12.00	98.89	P^+	31.00	100.00
CH^+	13.00	98.88	${PO_2}^{+2}$	31.50	99.76
Li_2O^{+2}	15.00	92.28	${PO_4}^{+3}$	31.67	99.76
O^+	16.00	99.76	${O_2}^+$	32.00	99.76
OH^+	17.00	99.75	${PH_2}^+$	33.00	99.99
H_2O^+	18.00	99.75	${PH_3}^+$	34.00	99.99
H_3O^+	19.00	99.75	Ga^{+2}	34.50	60.11
${PO_2}^{+3}$	21.00	99.76	Ga^{+2}	35.50	39.89

Continued on next page

Table A.1 – continued from previous page

Suggested Ion/Molecule	m/z (a.m.u)	Probability (%)	Suggested Ion/Molecule	m/z (a.m.u)	Probability (%)
FeO^{+2}	36.00	91.53	W^{+3}	61.00	14.31
$P_2O_3{}^{+3}$	36.67	99.76	W^{+3}	61.33	30.64
$Li_3PO_4{}^{+3}$	38.67	92.28	W^{+3}	62.00	28.43
P_2O^{+2}	39.00	99.76	Cu^{+}	63.00	69.17
$PO_3{}^{+2}$	39.50	99.76	P_2H^{+}	63.00	99.99
$P_2O_4{}^{+3}$	42.00	99.76	$P_2O_4{}^{+2}$	63.00	99.76
$FeO_2{}^{+2}$	43.00	5.84	$PO_2{}^{+}$	63.00	99.76
$FeO_2{}^{+2}$	44.00	91.53	$HPO_2{}^{+}$	64.00	99.00
$FePO_3{}^{+3}$	45.00	91.53	Pt^{+3}	64.67	32.90
W^{+4}	45.50	26.50	Pt^{+3}	65.00	33.80
W^{+4}	45.75	14.31	Pt^{+3}	65.33	25.30
W^{+4}	46.00	30.64	Pt^{+3}	66.00	7.20
W^{+4}	46.50	28.43	$FePO_3{}^{+2}$	66.50	5.84
PO^{+}	47.00	99.76	$FePO_3{}^{+2}$	67.50	91.53
$PO_4{}^{+2}$	47.50	99.76	Ga^{+}	69.00	60.11
HPO^{+}	48.00	99.00	FeO^{+}	70.00	5.84
$FePO_4{}^{+3}$	49.67	5.84	Ga^{+}	71.00	39.89
Cr^{+}	50.00	4,35	$FePO_4{}^{+2}$	74.50	5.84
$FePO_4{}^{+3}$	50.33	91.53	$FePO_4{}^{+2}$	75.50	91.53
Cr^{+}	52.00	83,79	$Fe_3O_4{}^{+3}$	77.33	91.53
$P_2O_6{}^{+3}$	52.67	99.76	P_2O^{+}	78.00	99.76
Cr^{+}	53.00	9,50	$Fe_2O_3{}^{+2}$	78.00	5.84
$Fe_2O_3{}^{+3}$	53.33	91.53	$LiFePO_4{}^{+2}$	78.50	6.86
Fe^{+}	54.00	5.85	$PO_3{}^{+}$	79.00	99.76
$P_2O_3{}^{+2}$	55.00	99.76	$Fe_2O_3{}^{+2}$	80.00	91.53
Fe^{+}	56.00	91.75	$P_4O_8{}^{+3}$	84.00	99.76
Fe^{+}	57.00	2.12	$FeO_2{}^{+}$	88.00	91.53
$Li_3PO_4{}^{+2}$	58.00	92.28	W^{+2}	91.00	26.50
W^{+3}	60.67	26.50	W^{+2}	91.50	14.31

Continued on next page

Table A.1 – continued from previous page

Suggested Ion/Molecule	m/z (a.m.u)	Probability (%)	Suggested Ion/Molecule	m/z (a.m.u)	Probability (%)
W^{+2}	92.00	30.64	$FePO_3{}^+$	135.00	91.53
W^{+2}	93.00	28.43	$LiFePO_3{}^+$	142.00	84.67
$PO_4{}^+$	95.00	99.76	$P_2O_5{}^+$	142.00	99.76
$HPO_4{}^+$	96.00	99.00	$FePO_4{}^+$	151.00	91.53
Pt^{+2}	97.00	32.90	$P_2O_6{}^+$	158.00	99.76
Pt^{+2}	97.50	33.80	$Fe_2O_3{}^+$	160.00	91.53
Pt^{+2}	98.00	25.30	Pt^+	194.00	32.90
$P_4O_6{}^{+2}$	110.00	99.76	Pt^+	195.00	33.80
$Fe_3O_4{}^{+2}$	116.00	91.53	Pt^+	196.00	25.30
$P_2O_4{}^+$	126.00	99.76	Pt^+	198.00	7.20
$FePO_3{}^+$	133.00	5.84	$P_4O_6{}^+$	220.00	99.76

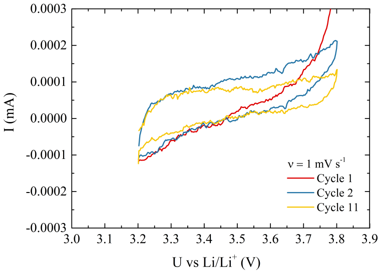

Figure A.1: CV data of a 150 nm thin LFP film before annealing, obtained at a scan rate of 1 mV s^{-1}. The 1st, 2nd, and 11th CV cycle are shown.

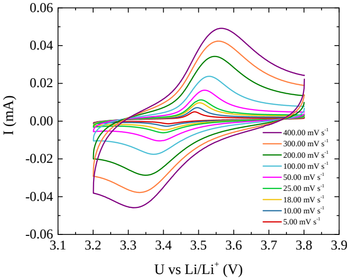

Figure A.2: CV data of a 25 nm thin LFP film at different scanning rates.

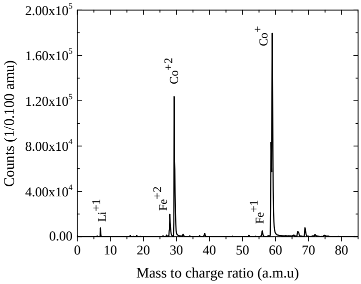

Figure A.3: The identified mass spectrum of the Co/LFP bi-layers.

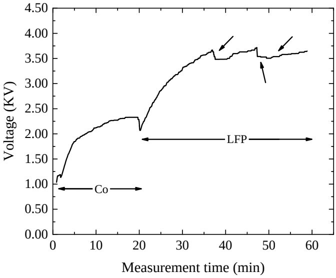

Figure A.4: Voltage evolution of the Co/LFP bi-layers. It is clearly seen the unstable behaviour of the LFP layer.

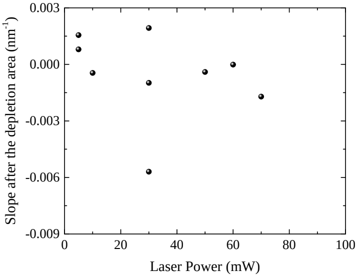

Figure A.5: Slope of the depletion region as compared to the laser power.

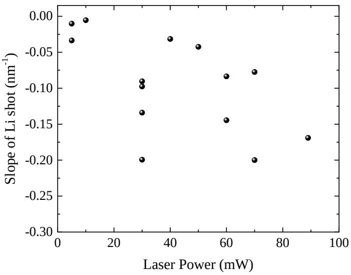

Figure A.6: Slope of the lithium shot as compared to the laser power.

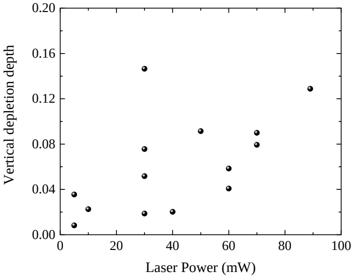

Figure A.7: Depletion depth as compared to the laser power.

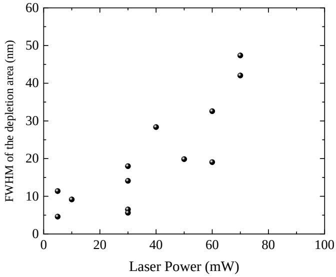

Figure A.8: FWHM of the depletion region as compared to the laser power.

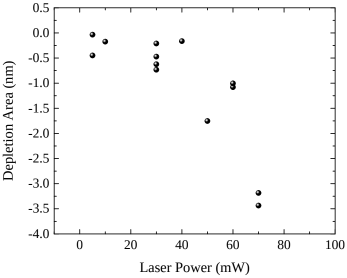

Figure A.9: Depletion region area as compared to the laser power.

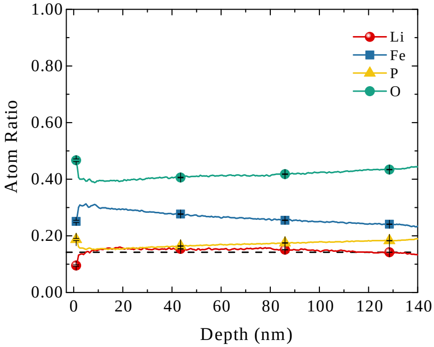

Figure A.10: Concentration profile extracted along the tip axis of the amorphous LFP. The tip was measured at 10 mW. The standard nominal ratio of Li in $LiFePO_4$ is plotted as a black dashed line. The measured concentrations from the APT were 14.83 at % Li, 25.84 at % Fe, 17.35 at % P and 41.96 at % O, whereas the nominal atomic concentrations are 14.28 at % Li, 14.28 at % Fe, 14.28 at % P, 57.14 at % O.

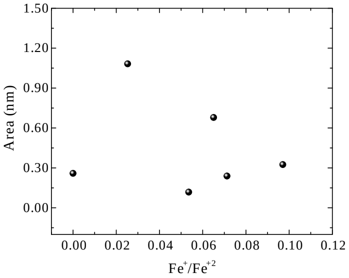

Figure A.11: Areas of the crystalline LFP as a function of the iron isotopes ratio Fe^{+}/Fe^{+2}.

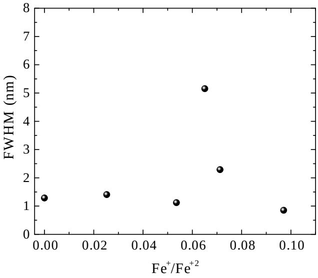

Figure A.12: FWHM of the crystalline LFP as a function of the iron isotopes ratio Fe^+/Fe^{+2}.

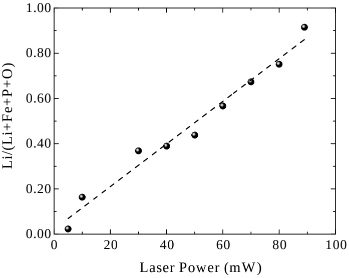

Figure A.13: Li concentration with respect to all elements as a function of the laser power.

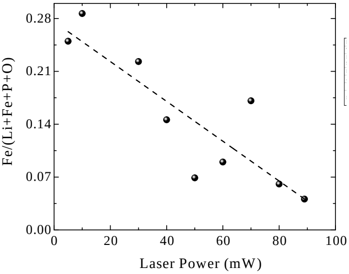

Figure A.14: Fe concentration with respect to all elements as a function of the laser power.

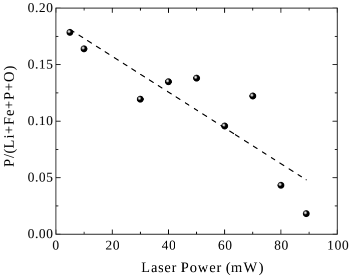

Figure A.15: P concentration with respect to all elements as a function of the laser power.

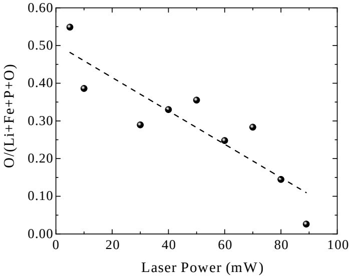

Figure A.16: O concentration with respect to all elements as a function of the laser power.

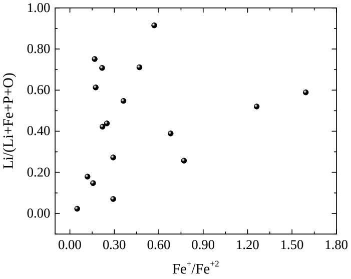

Figure A.17: Li concentration with respect to all elements as a function of the iron isotopes ratio Fe^{+2}/Fe^{+}.

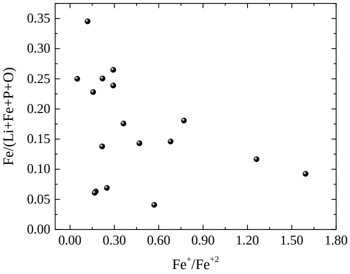

Figure A.18: Fe concentration with respect to all elements as a function of the iron isotopes ratio Fe^{+2}/Fe^{+}.

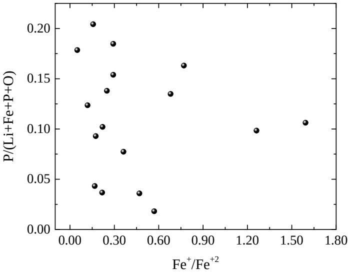

Figure A.19: P concentration with respect to all elements as a function of the iron isotopes ratio Fe^{+2}/Fe^{+}.

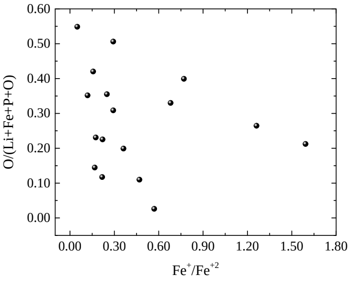

Figure A.20: O concentration with respect to all elements as a function of the iron isotopes ratio Fe^{+2}/Fe^{+}.

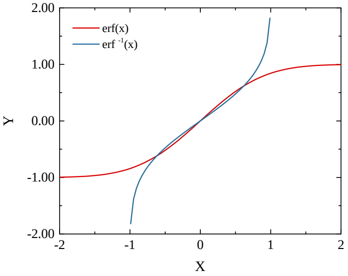

Figure A.21: The error function erf(x) and the inverse error erf^{-1}(x) function.

List of Tables

3.1 TEM lamella thinning voltages/currents as compared to the thickness. 47

4.1 Chemical compositions of LFP powder and thin film by Inductively Coupled Plasma - Optical Emission Spectrometry (ICP-OES) after assuming the ideal content of O. 50
4.2 Diffusion Coefficients (D) as a function of the layer thickness (d). 60

5.1 Stepwise variation of laser power in the experiment shown in Figure 5.20, laser powers and their orders at the same tip. 88

A.1 How to define Lithium Iron Phosphate peaks. 141

List of Figures

2.1 Elementary cell of the olivine-type structure of $LiFePO_4$, illustrating locations of Li atoms (green), Fe (yellow), P (violet), and O atoms (red) in the unit cell, tetrahedral of PO_4 and octahedra of FeO_6. After [28]. 7

2.2 Schematic shows the Li composition distribution inside a particle during the delithiation process. 10

2.3 Schematic shows the Li distribution by blue contours, whereas the brown octahedra represents FeO_6 and the purple tetrahedral represents PO_4 units. After [44]. 11

2.4 Schematic of the 'domino-cascade' model shows the de/intercalation processes in the LFP. After [45]. 11

2.5 Schematic represents the shrinking-core model in the LFP electrode. After [50]. 13

2.6 Schematic illustrates the 'radial mode' and its inactive/remnant cores. After [35]. 13

2.7 (a) Gibbs free energy and (b) the voltage profile as a function of Li concentration for a two phase transition battery material upon de-/ithiation. 15

2.8 Schematic representing a finite region between the lithiated and the delithiated phases. After [45]. 16

2.9 Schematic representation of the phase boundary. $LiFePO_4$ phase moves along the a-direction, while Li ions pull in and out the b-direction during dis/charging processes. After [52]. 17

2.10 Schematic diagram of a TEM setup. Left: diffraction mode, Right: imaging mode. After [69]. 20

2.11 Electron's potential energy diagrams, (left) in absence of the applied electric field, and (right) in presence of the applied electric field. x is the distance to the surface of an electron from a gas atom in the vicinity of a tip, I_0 is the energy of the first ionisation, x_c is the critical distance of ionisation, E_F is the Fermi energy and Q_c is the work function of the surface. After [71]. . . . 21

2.12 Schematic depicts the removal of a surface atom and the transition from the neutral atomic state (red) to the ionic state (blue). Atomic and ionic potential energy V(x) with and without electric field as function of the distance from the surface. Λ is the sublimation energy, n is the degree of ionisation, I_i is the ith ionisation energy, ϕ_e is the work function of the surface ion, Q_0 is the energy barrier without the electric field and Q(F) is the energy barrier with electric field. After [72]. 23

2.13 Schematic diagram shows a positively charged surface. After [71]. 25

2.14 Schematic diagram illustrates the field ion imaging. 26

2.15 Schematic represents the point-projection of surface atoms in a specimen [71]. 27

2.16 Schematic views of (a) lattice planes. (b) the radius curvature evolution. After [71]. 28

2.17 Scheme of the atom probe tomography (APT). After [82]. 30

2.18 Process diagram of the time of flight (ToF), electronics response as compared to the applied laser signal. After [82]. 31

2.19 Schematic illustration of the reconstruction algorithm. L is the distance between the surface of the sample and the detector, R is the radius of the apex, (x_D, y_D) are the cartesian coordinates of the evaporated ion on the detector. θ and θ' are the angles of the detected ion in the radial and compressed modes respectively. After [84]. 32

2.20 Left: Voxelisation with a constant volume. Right: Voxelisation with a constant number of atom per voxel. After [87]. 35

3.1 Schematic of the electropolishing setup. 37

3.2 Scheme of the sputtering chamber and the flat thin film electrodes stack. After [105]. 39

3.3 Potential waveform applied to the working electrode in the cyclic voltammetry experiment. 40

3.4 Potential (top) and corresponding current (bottom) waveforms in the chronoamperometry technique. 42

3.5 Schematic diagram of the FIB-SEM device; PtIN, platinum injection needle; CDM, continuous dynode electron multiplier detector; ETD, Everhart-Thornley detector; SS, sample stage. After [106]. 43

3.6 (1) E-beam deposited Pt layers using 5 kV. (2) Ion beam deposited Pt layer. (3, 4) Trenches milled into the specimen. 5) Micromanipulator attached to the lamella. (6, 7, 8) Lifting out the lamella. 44

3.7 (1) Placing and gluing the lamella on the 2 μm W post. (2) Cutting the lamella. (3, 4, 5, and 6) Sharpening of the tip in a descending manner. 46

3.8 (1, 2, and 3) lamella thinning procedures. 47

4.1 XRD spectra of the annealed LFP thin film as compared to the non-annealed LFP thin film and the LFP powder. All peaks are well clarified besides two main pronounced reflections of Pt and Si. 49

4.2 Bright field TEM images of the produced layers stack with the respective diffraction pattern from the LFP. LFP/Pt layers are stacked between two Pt protective coatings from the FIB and the SiO_2 substrate. Left: LFP_{100nm}/Pt_{150nm} in as-deposited state and its respective diffraction pattern confirm the amorphous structure. Right: LFP_{150nm}/Pt_{100nm} layers after an additional annealing in an ultrahigh vacuum ($<10^{-6}$ mbar) for 5 h at 500 °C. Crystalline LFP layer with some highlighted grains in red colour is shown. 51

4.3 CV data of a 200 nm thin LFP film at different scanning rates. For the sake of clarity, presentation was split into three regimes of decreasing scanning rate (a, b, c). Additional CVs for another thickness can be found in Appendix (Figure A.2). (d) LFP film measured in the voltage window 2.00-4.00 V, film thickness is 150 nm. 53

4.4 CV data for 100 nm thick at a constant scan rate 2.00 mV s^{-1} (6 C). The layer shows a stable dis-/charging cycling for 7000 cycles. 55

4.5 The calculated capacities for a 100 nm LFP thick film and their retention after 7000 dis-/charge cycles. 56

4.6 Randles-Sevcik (R.-S.) plots: (a, b) Double logarithmic plots of current density (j_p) versus the scan rate (ν) for the deintercalation and intercalation peaks, respectively. Linear regressions were plotted in dashed lines. As a reference for comparison with the experimental data, two black lines with exponents 0.50 (solid line) and 1.00 (dashed line) were drawn. 58

4.7 Randles-Sevcik (R.-S.) plots: (a, b) Current density (j_p) versus square root of the scan rate ($\nu^{1/2}$) for the deintercalation and intercalation peaks, respectively. Linear regressions were plotted in dashed lines, whereas two solid linear regressions were drawn in red and blue for the thickest films 250 and 200 nm, respectively. 58

4.8 (a, b) Peak currents normalized to films thicknesses as a function of the scan rate for the deintercalation and intercalation peaks, respectively. As a reference for comparison with the experimental data, two black lines with exponents 0.50 (solid line) and 1.00 (dashed line) were drawn. 59

4.9 (a) Evolution of the kinetic exponent versus the layer thickness. Such exponents were calculated from the regression lines of Figures 4.6 (a, b) for low scan rates. (b) Calculated slopes ($j_p/\nu^{1/2}$) versus the layer thickness. They were calculated from the regression lines of Figures 4.7 (a, b) for fast scan rates. 61

4.10 Linear relationship between the capacity per unit area and the layer thickness at $v = 1.00$ mV s^{-1}. The intersection of the regression dashed line and the x-axis is determined to be around 18 nm. 62

4.11 (a) Changes of the anodic and cathodic peak potentials for different thicknesses as a function of the scan rate (v). (b) Overpotentials for different layer widths at different scan rates. 62

4.12 (a) Peak current density (j_p) versus the overpotentials (ΔU) for different thicknesses. (b) Peak current density (j_p) versus the layer thickness (d) at different overpotentials. 64

4.13 Schematic diagram represents the Li transport. Thin arrows: ionic transport through the LFP grains, thick arrows: intercalation in LFP. 64

4.14 (a, b) Bright and (c, d) dark field TEM images of LFP thin films for thickness 250 nm and 100 nm, respectively. LFP layers locate directly next to the highlighted Pt electrode collector. 66

5.1 (a) SEM image of a tungsten needle. (b) Typical field ion micrograph of a pure W observed along the (110) direction. 68

5.2 Defined mass spectrum of the LFP/W bi-layers system. 69

5.3 (a) Atomic reconstruction of the LFP/W bi-layers. (b) An enlarge image of the lattice planes of tungsten. Li (pink), Fe (blue), P (green), O (cyan), and W (red). 70

5.4 Evaporation field difference between the LFP and W. The red circle interprets a sharp unstable transition between the two layers. 71

5.5 Composition depth profile extracted axially along the APT reconstruction of LFP/W. The standard nominal ratio of Li in $LiFePO_4$ is plotted as a black dashed line. 72

5.6 Iso-surfaces and the 2D Li composition maps highlighting the Li-rich regions. (a, b) 20.00 at % Li isocomposition top and side views. (c, d) Top and side 2D Li composition maps. 73

5.7 Mass spectrum of the LFP_{5nm}/Fe_{5nm} stack covered by a protective layer from iron. 74

5.8 Evaporation Fields of the LFP_{5nm}/Fe_{5nm} stack covered by a protective layer from iron. 75

5.9 Composition profile of the LFP_{5nm}/Fe_{5nm} stack covered by a protective layer from iron. 76

5.10 (a) 3D atomic reconstruction of the LFP_{5nm}/Fe_{5nm} stack covered by a protective layer from iron. (b) Distribution of Li through the stack. Li (pink), Fe (blue), P (green), and O (cyan). . 76

5.11 (a) SEM image of the 2 μm W post after flatting by the FIB. The top surface is marked by a white circle. (b) The same 2 μm W post after sputtering a thick 1-2 μm layer of LFP then reshaped by the FIB. The LFP is capped as a dark black colour on the tungsten. 77

5.12 An example of a mass spectrum of the amorphous LFP measured at laser power 30 mW. Each peak is well separated and has a good signal to noise ratio. To clarify the background, the figure was drawn with broken y-axis. 78

5.13 Concentration profile extracted along the tip axis of the amorphous LFP. The tip was measured at laser power 60 mW. The standard nominal ratio of Li in $LiFePO_4$ is plotted as a black dashed line. The gray area marks the depletion region. 79

5.14 Proximity histogram obtained across ±15 nm of the interface showing the concentration partitioning between the Li rich and poor regions. 80

5.15 (a) Top and (b) side views of the 3D reconstruction for the amorphous LFP; Li (pink), Fe (blue), P (green), and O (cyan). (c) A 10.00 at % Li iso-composition surface highlights the Li-enriched/poor regions throughout the reconstructed volume. (d) Top and (e) side inner views of 2D Li composition maps, red regions represent high charge Li density, while lower densities are illustrated in green and blue. The colour scale bar of sub-figures (c-e) is shown in the middle of the Figure. The geometrical scale bar is drawn as a black box beside each sub-figure. 81

5.16 (a) Li, (b) Fe, (c) P, and (d) O concentrations with respect to (Li+Fe+P+O) as a function of the laser power. The standard nominal ratio of each element in $LiFePO_4$ is plotted in black dashed line. 82

5.17 An example of a mass spectrum of the crystalline LFP measured at a laser power of 30 mW. To clarify the background to noise ratio, the figure was drawn with broken y-axis. 84

5.18 Axial extracted composition profiles of the annealed LFP along the tip axis. The tip was measured at a laser power of 40 mW. The standard nominal ratio of Li in $LiFePO_4$ is plotted as a black dashed line. 85

5.19 (a) Top and (b) side views of the 3D reconstruction of the crystalline LFP; Li (pink), Fe (blue), P (green), and O (cyan). (c) A 14.00 at % Li iso-composition surface. (d, e) Top and side inner views of 2D Li composition maps. The colour scale bar of sub-figures (c-e) is shown in the middle of the figure. The geometrical scale bar is drawn as a black box beside each sub-figure. 86

5.20 (Left) DC voltage evolution curve of the amorphous LFP at different laser powers. Laser powers are represented in different colours. (Right) Schematic diagram shows the laser power values and their orders during the measurement. At each laser power 2 millions of events were counted, except the last laser power, which delivered 18 millions of events. The laser power of 30 mW was selected as a measurement reference. 87

5.21 A defined mass spectrum of the amorphous LFP measured at different laser powers. Table 5.1 illustrates the laser powers and their ranks. 89

5.22 (a) Iron charge state ratios $Fe^{+2}/(Fe^{+} + Fe^{+2})$ of the amorphous LFP at different laser powers of the experiment shown in Figure 5.20. (b) The corresponding field strength as compared to the laser power. Field strength was estimated from the Kingham's Fe curves. For a state of clarity, the beginning of the measurement is represented in red colour. This region is interrupted by the Li drift. On the other side, the end of the measurement is represented in yellow colour. 90

5.23 Kingham curves of Fe derived from the post field ionization theory [131], (Fe^{+} blue, Fe^{+2} orange, and Fe^{+3} red). After [132]. . . . 90

5.24 Elemental concentration ratios with respect to Fe as a function of the laser power (left) and the field strength (right). (a, b) O/Fe, (c, d) P/Fe, and (e, f) Li/Fe, respectively. For a state of clarity, the beginning of the measurement (30 mW) is represented in red colour. This stage is distinguished by the strong Li drift. On the other side, the end of the measurement (30 mW) is represented in yellow colour. 91

5.25 Concentration profile extracted along the tip axis of the amorphous LFP. The tip was measured at different laser powers, see table 5.1. The scale bar of the laser powers is put above the figure. Colours of the scale bar are synchronized with Figure 5.20. The standard nominal ratio of Li in $LiFePO_4$ is plotted as a black dashed line. 92

5.26 Amorphous LFP at different laser powers; (a) the 3D reconstruction Li (pink), Fe (blue), P (green), and O (cyan). (b) Inner view of the 2D Li composition map. (c, d) 47 and 69 at % Li isocomposition surface. The scale colour bar of the sub-figures (b-d) is shown in the middle of the figure. The geometrical scale bar is drawn as a black box beside each sub-figure. 94

5.27 Lateral 2D Li composition map of the amorphous LFP at different laser powers; (a) at the top 30 mW, (b) at 60 mW, (c) at 80 mW. The scale colour bar is shown on the top of the figure. The geometrical scale bar is drawn as a black box. 95

5.28 Li distribution of both LFP states through the axes of the tips as compared to the laser powers. (a) for amorphous LFP and (b) for crystalline LFP. The standard nominal ratio of Li in $LiFePO_4$ is plotted in two black dashed lines. 96

5.29 (a) Areas and (b) FWHMs of the Li enrichment peaks at different laser powers. 97

5.30 (a, b) An example shows the Li axial composition profile and the DC voltage evolution of an amorphous LFP sample measured at laser power 30 mW. The shadowed regions represent the areas of the Li shot and the Li depletion, while the FWHM is represented in the figure. (c, d) Li concentration profile and the DC voltage evolution for an amorphous LFP measured at laser power 70 mW. A possible fracture period of the measurement is shown. 98

5.31 Schematic simulates the Li diffusion along the tip. The tip is divided into N slices, a_0 is the lattice plane distance, while n_0 represents the initial Li content in each slice. 99

5.32 Simulated Li concentration profile as compared to the measured one at laser power 90 mW at a constant diffusivity. The black colour shows the experimental result, while cyan colour represents the computed outcome. Note the bad matching after 50 nm depth. 101

5.33 Potential trace for solute in a disordered material. The black dots represent the solute atoms. G is the Gibbs free energy. Q is the activation energy. 102

5.34 Simulated composition profile with different σ values at the same initial diffusivity. An enlarged is set to clarify differences. . 102

5.35 Simulated Li concentrations profiles as compared to the measured ones at different laser powers (a) 90 mW, (b) 60 mW, (c) 50 mW, (d) 30 mW. The black colour shows the experimental results, while cyan colour represents the computed outputs of the theoretical model. 103

5.36 The simulated diffusivities at different Li concentrations for different laser power. 104

5.37 The simulated diffusivities at different laser power for different Li concentrations. 104

5.38 Relative initial diffusivity for amorphous LFP calculated from the theoretical model. 105

6.1 (a) CV data of a 300 nm thin LFP film obtained at a scan rate of 0.33 mV s^{-1}, the 2nd (red) and the last 20th (blue) cycles are shown. (b) After the 20^{th} cycle, a constant potential, in this example 3.48 V, was applied for 5 hours to establish an equilibrium distribution of the Li ions. 107

6.2 (a) Mass spectrum of a discharged LFP, lithiation state 70.00 %. The tip was measured at a laser power of 40 mW. (b) Concentration profiles extracted along the tip axis of a discharged LFP, lithiation state 70.00 %. The tip was measured at a laser power of 40 mW. The standard nominal ratio of Li in $LiFePO_4$ at this lithiation state (70.00 %) is plotted as a black dashed line. 108

6.3 3D reconstruction of the discharged LFP (70.00 %) -(a) All elements ; Li (pink), Fe (blue), P (green), and O (cyan) (b) A slice of 1 nm thick of only Li element, slice size 160x120x1 nm^3. (c) A 28.00 at % Li iso concentration surface highlights the Li-enriched/poor regions throughout the reconstructed volume. Geometrical scale bars are drawn as black boxes beside each sub-figure. 108

6.4 (a-c) Top and (d-f) side inner views of 2D density maps of all atoms, red regions represent high density, while lower densities are illustrated in green and blue. (g-i) 47.1, 54.8, and 73.1 atom nm^{-3} iso-density surfaces show the dense regions throughout the reconstructed volume in 3D views. The scale colour bar is shown in the left of the figure. Geometrical scale bars are drawn as black boxes beside each sub-figure. 110

6.5 (a, b) Side and (c) top inner views of 2D composition maps of Li, red regions represent high concentrated Li regions density, while lower regions are illustrated in green and blue. The scale colour bar is shown in the left of the figure. Geometrical scale bars are drawn as black boxes beside each sub-figure. 110

6.6 (a, b) Side and (c, d) top inner views of 2D Li density maps. (e-g) 7.7, 8.8, and 12.1 atom nm^{-3} Li iso-density surfaces highlight the Li rich/poor regions throughout the reconstructed volume. Lithiation state is 70 %. The scale colour bar is shown in the left of the figure. Geometrical scale bars are drawn as black boxes beside each sub-figure. 111

6.7 (a) CV spectrum of a 300 nm thin LFP film at scan rate 0.33 mV s^{-1}. The figure represents the termination potentials. (b) CV curve in the current versus time domain. (c) Axial extracted Li composition profiles for LFP at different dis/charge states. The tips were measured at laser power 40 mW. (d) Observed Li contents as compared to the theoretical values at different lithiation states. Li amounts were calculated from the whole tips. The standard nominal ratio of Li in $LiFePO_4$ at lithiation state 100.00 % is plotted as black dashed lines in sub-figures (c) and (d). 112

6.8 (a) 91.4 atom nm^{-3} LFP iso-density surface highlight the rich/poor regions of all elements throughout the reconstructed volume. (b, c) Side and top inner views of 2D density maps of all elements, red regions represent high charge LFP density, while lower densities are illustrated in green and blue. Lithiation state is 1.12 %. The scale colour bar is shown in the left of the figure. Geometrical scale bars are drawn as black boxes beside each sub-figure. 113

6.9 (a) 5.7 atom nm^{-3} Li iso-density surface highlight the rich/poor regions of Li element throughout the reconstructed volume. (b, c) Side and top inner views of 2D density maps of Li elements, red regions represent high charge LFP density, while lower densities are illustrated in green and blue. Lithiation state is 1.12 %. The scale colour bar is shown in the left of the figure. Geometrical scale bars are drawn as black boxes beside each sub-figure. 114

6.10 Statistical analyses of the Li distribution at different lithiation states. Observed frequency distributions (solid line) in comparison to their binomial distributions (dashed line) with corresponding Pearson coefficients. (a-f) represent lithiation states 1.12 %, 17.48 %, 34.48 %, 70.00%, 93.96 %, and 100.00 %, respectively. (g, h) Normalized frequency distributions for observed and binomial distributions for Li at different lithiation states, respectively. 115

6.11 (a, b) Pearson coefficients of Li distribution in dis/charged LFP versus the lithiation states and Li concentrations measured by APT, respectively. 116

6.12 CV curves of a 150 nm LFP thin film. The 1st and 11th cycles are shown. The black arrow in the figure refers to the existence of uninterested phases before cycling. 117

6.13 Statistical analyses of the Fe distribution at different lithiation states. Observed frequency distributions (solid line) in comparison to their binomial distributions (dashed line) with corresponding Pearson coefficients. (a-f) represent lithiation states 1.12 %, 17.48 %, 34.48 %, 70.00%, 93.96 %, and 100.00 %, respectively. (g, h) Normalized frequencies for observed and binomial distributions of Fe at different lithiation states, respectively. . . . 118

6.14 (a) and (b) Pearson coefficients of the Fe distribution in dis-/charged LFP versus the lithiation states and Fe concentration measured by APT, respectively. 120

6.15 Statistical analyses of the P distribution at different lithiation states. Observed frequency distributions (solid line) in comparison to their binomial distributions (dashed line) with corresponding Pearson coefficients. (a-f) represent lithiation states 1.12 %, 17.48 %, 34.48 %, 70.00%, 93.96 %, and 100.00 %, respectively. (g, h) Normalized frequencies for observed and binomial distributions of P at different lithiation states, respectively. 121

6.16 (a) and (b) Pearson coefficients of the P distribution in dis-/charged LFP versus the lithiation states and P concentration measured by APT, respectively. 122

6.17 Statistical analyses of the O distribution at different lithiation states. Observed frequency distributions (solid line) in comparison to their binomial distributions (dashed line) with corresponding Pearson coefficients. (a-f) represent lithiation states 1.12 %, 17.48 %, 34.48 %, 70.00%, 93.96 %, and 100.00 %, respectively. (g) and (h) Normalized frequencies for observed and binomial distributions of O at different lithiation states, respectively. 123

6.18 (a) and (b) Pearson coefficients of the O distribution in dis-/charged LFP versus the lithiation states and O concentration measured by APT, respectively. 124

A.1 CV data of a 150 nm thin LFP film before annealing, obtained at a scan rate of 1 mV s^{-1}. The 1^{st}, 2^{nd}, and 11^{th} CV cycle are shown. 143

A.2 CV data of a 25 nm thin LFP film at different scanning rates. . . . 144

A.3 The identified mass spectrum of the Co/LFP bi-layers. 144

A.4 Voltage evolution of the Co/LFP bi-layers. It is clearly seen the unstable behaviour of the LFP layer. 144

A.5 Slope of the depletion region as compared to the laser power. . . 145

A.6 Slope of the lithium shot as compared to the laser power. 145

A.7 Depletion depth as compared to the laser power. 145

A.8 FWHM of the depletion region as compared to the laser power. . 146

A.9 Depletion region area as compared to the laser power. 146

A.10 Concentration profile extracted along the tip axis of the amorphous LFP. The tip was measured at 10 mW. The standard nominal ratio of Li in $LiFePO_4$ is plotted as a black dashed line. The measured concentrations from the APT were 14.83 at % Li, 25.84 at % Fe, 17.35 at % P and 41.96 at % O, whereas the nominal atomic concentrations are 14.28 at % Li, 14.28 at % Fe, 14.28 at % P, 57.14 at % O. 147

A.11 Areas of the crystalline LFP as a function of the iron isotopes ratio Fe^{+}/Fe^{+2}. 147

A.12 FWHM of the crystalline LFP as a function of the iron isotopes ratio Fe^{+}/Fe^{+2}. 148

A.13 Li concentration with respect to all elements as a function of the laser power. 148

A.14 Fe concentration with respect to all elements as a function of the laser power. 148

A.15 P concentration with respect to all elements as a function of the laser power. 149

A.16 O concentration with respect to all elements as a function of the laser power. 149

A.17 Li concentration with respect to all elements as a function of the iron isotopes ratio Fe^{+2}/Fe^{+}. 149

A.18 Fe concentration with respect to all elements as a function of the iron isotopes ratio Fe^{+2}/Fe^{+}. 150

A.19 P concentration with respect to all elements as a function of the iron isotopes ratio Fe^{+2}/Fe^{+}. 150

A.20 O concentration with respect to all elements as a function of the iron isotopes ratio Fe^{+2}/Fe^{+}. 150

A.21 The error function erf(x) and the inverse error erf^{-1}(x) function. . 151

ABDELKARIM, AHMED

Battery Materials Scientist

@ PhD.Abdelkarim@gmail.com
☎ +491748534776
Heisenbergstraße.3, Stuttgart, Germany
Date of Birth and Place: 29 May 1987 in Cairo
Marital Status: Single
Nationality: Egyptian
Stuttgart, Deutschland
Work permit: Unrestricted in Europe
in linkedin.com/in/ahmed-mohamed-302995170

WORK EXPERIENCE

PhD Candidate/Researcher

University of Stuttgart

Apr. 2017 – May. 2021 Stuttgart-Germany

- Research and Development
  1. Electrochemistry of Li battery cells/-electrodes
  2. Morphological characterizations and Nano-structural manipulations of Li materials.
  3. 3D preparations and analyses of Li materials at the atomic level scale.

https://www.uni-stuttgart.de/

Researcher

National Research Center

Nov. 2008 – Nov. 2016 Giza-Egypt

- Research and Development
  1. Electrical and optical studies of prepared materials by pulsed laser deposition. For instance, producing a highly conductive transparent electrodes by laser for solar cells.
  2. Laser ablation, preparing nano-sized materials by laser.
  3. Atomic Absorption Spectroscopy, quantitative analyses (elements contents) of materials.

http://www.nrc.sci.eg

Teaching Assistant

Misr University for Science and Technology

Oct. 2011 – Jun. 2013 Cairo-Egypt

- Physics Instructor
  1. Responsible for teaching and supervising engineering students for experimental physics.

http://www.must.edu.eg/

Physicist

Alfa Lab

Sep. 2014 – Oct. 2016 Cairo-Egypt

- Analyse
  1. Statistical blood analyses for some specific diseases.

https://www.alfalaboratory.com/

PHILOSOPHY OF LIFE

"You are the author of your own life."

PROUD OF

Fantastic performance
My Doctorate is the first study of its kind over the world

Another success
I'm a DAAD scholarship holder

STRENGTHEN

Hard Working Flexible Teamwork Self Motivated

Microsoft Office Origin Latex

LANGUAGES

Arabic (*C2*)	●●●●●
English (*C1*)	●●●●○
German (*B2*)	●●●○○
French (*A1*)	●○○○○

INTERESTS

Swimming Football Read books

EDUCATION AND SKILLS

PhD in materials science (Battery Materials)

University of Stuttgart

📅 Apr. 2017 – March. 2021 📍 Stuttgart-Germany

- Materials science, Battery materials
- Thesis topic ’Three Dimensional Analytical Study of Thin Film Battery Electrodes.’
  1. Electrochemistry of Li materials (Open Circuit Voltage (OCV), Cyclic Voltammetry (CV), Chronopotentiometry (CP), Chronoamperometry (CA)).
  2. Checking the functionality, capacity, performance, cyclability, stability and capacity retention of Li electrodes.
  3. Structural and morphological characterization of Li materials by X-ray diffraction (XRD), Transmission Electron Microscope (TEM), and Scanning Electron Microscope (SEM).
  4. Nano-structural manipulations of Li materials using Dual Beam Microscopy (SEM/FIB).
  5. 3D analyses of Li materials at the atomic level scale by Atom Probe Tomography (APT).

https://www.uni-stuttgart.de/

Master in Physics (Lasers and Nanomaterials)

Ain Shams-University

📅 May 2011 – Nov. 2013 📍 Cairo-Egypt

- Thesis topic ’Electrical, Optical and Structural Studies of some Transparent Conducting Films Prepared by Pulsed Laser Deposition.
  1. Preparing and studying transparent conducting oxide thin films for solar cells windows.

http://www.asu.edu.eg/

Bachelor of Science (Electronic Physics)

Ain Shams-University

📅 Sep. 2004 – Jun. 2008 📍 Cairo-Egypt

1. Microcontrollers and digital signal processing.

http://www.asu.edu.eg/

REFERENCES

Prof. Dr. Dr. h. c. Guido Schmitz

@ Institute of Materials science (IMW), University Stuttgart

✉ Guido.Schmitz@mp.imw.uni-stuttgart.de

Heisenbergstraße 3, 70569 Stuttgart, Germany.

Prof. Dr. Hassan Talaat

@ Physics Department, Ain Shams University

✉ hassantalaat@hotmail.com

Faculty of Science, Ain Shams University, Abbassia, Cairo 11566, Egypt.

Prof. Dr. Emad Elmenyawy

@ Physics Department, National Research Center

✉ `emad_elmenyawy`@yahoo.com

33 El Buhouth Street, Ad Doqi, Dokki Cairo 12622, Egypt

Abdelkarim, Ahmed
Stuttgart, January 14, 2022

ABDELKARIM, AHMED

Batteriematerialien Wissenschaftler

@ phd.abdelkarim@gmail.com ☎ +491748534776
Heisenbergstraße.3, Stuttgart, Deutschland Geburtsdatum/-ort: 29 Mai 1987 in Kairo
Familienstand: Ledig Staatsangehörigkeit: Ägypter
Stuttgart, Deutschland Arbeitserlaubnis: Uneingeschränkt in Deutschland
in linkedin.com/in/ahmed-mohamed-302995170

BERUFSERFAHRUNG

PhD Forscher

Universität Stuttgart

Apr. 2017 – Okt. 2021 Stuttgart-Deutschland

- Forschung und Entwicklung
  1. Elektrochemie von Li-Batteriezellen / -elektroden
  2. Morphologische Charakterisierungen und nanostrukturelle Manipulationen von Li-Materialien.
  3. 3D-Präparationen und Analysen von Li-Materialien auf atomarer Ebene.

https://www.uni-stuttgart.de/

Forscher

Nationales Forschungszentrum, die ägyptische Regierung

Nov. 2008 – Nov. 2016 Giza-Ägypten

- Forschung und Entwicklung
  1. Elektrische und optische Untersuchungen von vorbereiteten Materialien durch gepulste Laserabscheidung. Zum Beispiel die Herstellung hochleitfähiger transparenter Elektroden bei Laser für Solarzellen.
  2. Laserablation, Herstellung nanoskaliger Materialien bei Laser.
  3. Atomabsorptionsspektroskopie, quantitative Analysen (Elementgehalt) von Materialien.

http://www.nrc.sci.eg

Lehrassistent

Misr Universität für Wissenschaft und Technologie

Oct. 2011 – Jun. 2013 Kairo-Ägypten

- Physiklehrer
  1. Verantwortlich für das Unterrichten und Betreuen von Ingenieurstudenten für experimentelle Physik.

  http://www.must.edu.eg/

Physiker

Alfa Labor

Sep. 2014 – Oct. 2016 Kairo-Ägypten

- Analyse
  1. Statistische Blutanalysen für bestimmte Krankheiten.

LEBENSPHILOSOPHIE

“Du bist der Autor deines eigenen Lebens.”

AUSZEICHNUNGEN

Fantastische Leistung
Meine Doktorarbeit ist die erste Studie dieser Art auf der ganzen welt

Ein weiterer Erfolg
Ich bin ein DAAD Stipendiat

STÄRKEN

Fleißig | Flexibel | Teamfähigkeit | Selbst Motiviert

Microsoft Office | Origin | Latex

SPRACHKENNTNISSE

Arabisch (*C2*)	●●●●●
Englisch (*C1*)	●●●●○
Deutsch (*B2*)	●●●○○
Französisch (*A1*)	●○○○○

INTERESSEN

Schwimmen | Fußball | Bücher lesen

https://www.alfalaboratory.com/

AKADEMISCHE STUDIEN

Promotion in den Materialwissenschaften (Batteriematerialien)

Universität Stuttgart

📅 Apr. 2017 – Okt. 2021 📍 Stuttgart-Deutschland

- Thema der Doktorarbeit 'Dreidimensionale analytische Untersuchung von Dünnschichtbatterieelektroden'
  1. Elektrochemie von Li-Materialien (Leerlaufspannung (OCV), Cyclovoltammetrie (CV), Chronopotentiometrie (CP), Chronoamperometrie (CA)).
  2. Überprüfung der Funktionalität, Kapazität, Leistung, Zyklisierbarkeit, Stabilität und Kapazitätserhaltung von Li-Elektroden.
  3. Strukturelle und morphologische Charakterisierung von Li-Materialien von Li-Materialien durch Röntgenbeugung (XRD), Transmissionselektronenmikroskop (TEM) und Rasterelektronenmikroskop (SEM).
  4. Nanostrukturelle Manipulationen von Li-Materialien mittels Dual Beam Microscopy (SEM/FIB).
  5. Dreidimensionale Analyse von Li-Materialien auf atomarer Ebene mittels Atom Probe Tomography (APT).

https://www.uni-stuttgart.de/

Master in Physik (Laser und Nanomaterialien)

Ain Shams-Universität

📅 Mai 2011 – Nov. 2013 📍 Kairo-Ägypten

- Thema der Masterarbeit 'Elektrische, optische und strukturelle Untersuchungen einiger transparenter leitender Filme, die durch gepulste Laserabscheidung hergestellt wurden'
  1. Vorbereitung und Untersuchung transparenter leitender Oxiddünnfilme für Solarzellenfenster.

http://www.asu.edu.eg/

Bachelor in Elektronik Physik

Ain Shams-Universität

📅 Sep. 2004 – Jun. 2008 📍 Kairo-Ägypten

1. Mikrocontroller und digitale Signalverarbeitung.

http://www.asu.edu.eg/

REFERENZEN

Prof. Dr. Dr. h. c. Guido Schmitz

@ Institute of Materials science (IMW), University Stuttgart

✉ Guido.Schmitz@mp.imw.uni-stuttgart.de

Heisenbergstraße 3, 70569 Stuttgart, Germany.

Prof. Dr. Hassan Talaat

@ Physics Department, Ain Shams University

✉ hassantalaat@hotmail.com

Faculty of Science, Ain Shams University, Abbassia, Cairo 11566, Egypt.

Prof. Dr. Emad Elmenyawy

@ Physics Department, National Research Center

✉ emad_elmenyawy@yahoo.com

33 El Buhouth Street, Ad Doqi, Dokki Cairo 12622, Egypt

VERÖFFENTLICHUNGEN

Peer Review Artikel

- Abdelkarim, A. (2015). “Femtosecond pulsed laser induced growth of highly transparent indium-tin-oxide thin films: Effect of deposition temperature and oxygen partial pressure”. In: *Optik* 126.23, pp. 3789–3794. ISSN: 0030-4026. DOI: `https://doi.org/10.1016/j.ijleo.2015.07.158`.
- – (2011). “Temperature Dependence of Transparent Conducting Oxide”. In: *Egyptian Journal of Solid State* 34, pp. 261–271.

Konferenzberichte

- Abdelkarim, A. (2021a). “Li mobility in Lithium Iron Phosphate measured by APT”. in: Pacific Northwest, USA.
- – (2021b). “Three dimensional visualization of lithium iron phophate (LFP) at different dis-/charge states”. In: Pacific Northwest, USA.
- – (2020a). “APT analysis of lithium in Lithium Iron Phophate (LFP) at different field strength”. In: Dreseden, Germany.
- – (2020b). “Li kinetics in Lithium Iron Phosphate by APT”. in: Oxford, England.
- – (2019). “Measurement of Li mobility in Lithium Iron Phosphate by APT at different field strength”. In: Düsseldorf, Germany.
- “The 5th National Conference on Optical Spectroscopy, laser and their Applications” (2014). In: Cairo, Egypt.
- “Application of Molecular Modeling” (2013). In: Cairo, Egypt.
- “The 3rd International Workshop on Ultra Fast Technology and Applications” (2012). In: Cairo, Egypt.
- “Nanomaterials and Nanocatalysis for Energy Petrochemicals and Environmental Applications” (2010). In: Cairo, Egypt.

Abdelkarim, Ahmed
Stuttgart, January 14, 2022